

Sensitivity of precipitation to Mediterranean SSTs in the case of the Vb-type cyclone in August 2005 using the regional model WRF

Master's Thesis

Faculty of Science
University of Bern

presented by

Claudio Kummler

2014

Supervisor:
PD Dr. Christoph C. Raible

Co-Supervisor:
Dr. Juan José Gómez-Navarro

Climate and Environmental Physics
Physics Institute of the University of Bern

Contents

1	Introduction	3
1.1	Prominent Vb-type cyclones and their implications	5
1.2	Theoretical background	6
1.3	State of knowledge	9
1.4	Objectives	11
2	Regional model, input data, and experimental design	13
2.1	System components of the WRF model	13
2.2	Reanalysis and observational data	19
2.3	WRF preprocessing system	21
2.4	Experimental design	22
3	Methods	27
3.1	Precipitation analysis	27
3.1.1	Precipitation impact of Vb-type cyclones	27
3.1.2	Precipitation analysis of WRF output	30
3.2	Cyclone detection and tracking	31
3.2.1	Cyclone tracking for the Vb climatology	32
3.2.2	Cyclone tracking for WRF output	33
4	Climatology of Vb-type cyclones and their impacts on precipitation	35
4.1	Vb climatology	35
4.2	Impact on precipitation	40
4.3	Discussion	44
5	Sensitivity of Vb-type cyclones to SSTs in the Mediterranean	47
5.1	Ctrl simulation	47
5.2	Sensitivity experiments	58
5.3	Discussion	68
6	Conclusion	71
7	Outlook	73
A	Programs and Scripts	75
A.1	Detection of z700 minima in WRF output	75

B Namelists	79
B.1 namelist.wps	79
B.2 namelist.input	80

Abstract

Mid-latitude cyclones are meso to large scale weather phenomena that are able to cause extreme events such as storms and floodings. In this regard, there is a characteristic trajectory of low pressure systems that renders specific geographic locations more prone to be affected by these extreme weather events. This characteristic cyclone trajectory is called Vb, which starts in the Mediterranean Basin and moves around the eastern Alps towards the Ukraine. Vb-type cyclones were continually responsible for strong flooding in Switzerland, Germany, and Austria. Despite a broad range of analysis that are concerned with the intensification and activity of mid-latitude cyclones, there is a particular lack in highly resolved analysis of the track Vb.

To make a first step to a better understanding of these phenomena, a climatology of Vb-type cyclones is presented, which is based on data from the ERA-interim reanalysis from 1979-2009. In this climatology, 89 Vb-type cyclones are detected, which is equal to a mean of 2.97 events per year. A third of the identified Vb-type cyclones occurred in spring, with a secondary maximum in fall, where about a fourth of the identified Vb-type cyclones occurred. The mean value of Vb related precipitation anomalies is significantly higher than the mean value of all the rain anomalies in ERA-interim from 1979-2009. In this respect, roughly one fifth of the 89 identified Vb-type cyclones contributes to extreme precipitation events (99th percentile).

Besides the climatology, another scope of this study is to assess the role of the sea surface temperatures (SSTs) in the Mediterranean for precipitation in Switzerland in the case of the Vb-type cyclone that occurred in August, 2005. Therefore, a number of sensitivity experiments with the regional model WRF is performed. The results show that uniformly increased SSTs in the Mediterranean are associated with an intensification of the investigated Vb-type cyclone, due to diabatic processes. In this regard, SST changes in the Mediterranean are non-linearly related to precipitation in Switzerland: If the Mediterranean SSTs of the WRF ctrl simulation are increased by 2 K and beyond, the accumulated precipitation in Switzerland from August 20 (00 UTC) to August 24, 2005 (00 UTC) increases substantially from 86 mm in WRF ctrl to more than 115 mm in the +5 K experiment. Projections of Mediterranean SSTs estimate a uniform mean increase of about 3 K until 2100 (Lionello et al., 2002). This suggests that a Vb-type cyclone such as the one that occurred in August 2005 might be even more severe, and could potentially cause even more damage in the context of higher Mediterranean SSTs.

Chapter 1

Introduction

Koeppen (1881) was one of the first who produced a map of mean trajectories of barometric minima over central Europe, where he found a preferred trajectory of low pressure systems that move from France to the Mediterranean Sea, and then around the eastern Alps towards Poland and the Ukraine. In the year 1891, the German Meteorologist W.J. van Bebber made a further effort in analyzing surface pressure maps over Europe and found as well preferred trajectories of mid-latitude low pressure systems (van Bebber, 1891). Thereby, he classified the respective trajectories of isolated pressure minima into five categories (Fig. 1.1). Later on, Mudelsee et al. (2004) found a causal relationship between a specific propagation path of low pressure systems and heavy precipitation and flooding. A cyclone on a Vb trajectory, which is the only of W. J. van Bebber's trajectories that is still in use, moves either from the Gulf of Genoa or the Adriatic Sea around the eastern Alps towards Russia. These phenomena often transport large amounts of moisture around the Alps due to their counterclockwise rotation. Accordingly, there were several Vb-type cyclones in the past that were responsible for substantial flooding in countries that are located north of the Alps such as Switzerland, Germany, and Austria.

The IPCC (2007) argued that the Mediterranean Basin (MB), where the Vb trajectory starts, is a hot spot for future climate change. In this respect, average temperatures in the MB are projected to increase from 2.2 K to 5.1 K by the end of the century compared to the 1980-1999 average level. Thereby, it is conceivable that an increase of the sea surface temperatures (SSTs) in the MB induce changes in Mediterranean latent heat and moisture fluxes. Furthermore, this could have an impact on the genesis and intensification of Vb-type cyclones through diabatic processes. In this regard, the sensitivity of Mediterranean SSTs to Vb related precipitation on the northern side of the Alps becomes interesting.

Thus, the aim of this study is to investigate the sensitivity of Vb-type cyclones and the related precipitation in Switzerland to the SSTs in the MB. Furthermore, a tracking of Vb-type cyclones, as already done in Hofstaetter and Chimani (2012), is performed to present a climatology of Vb-type cyclones.

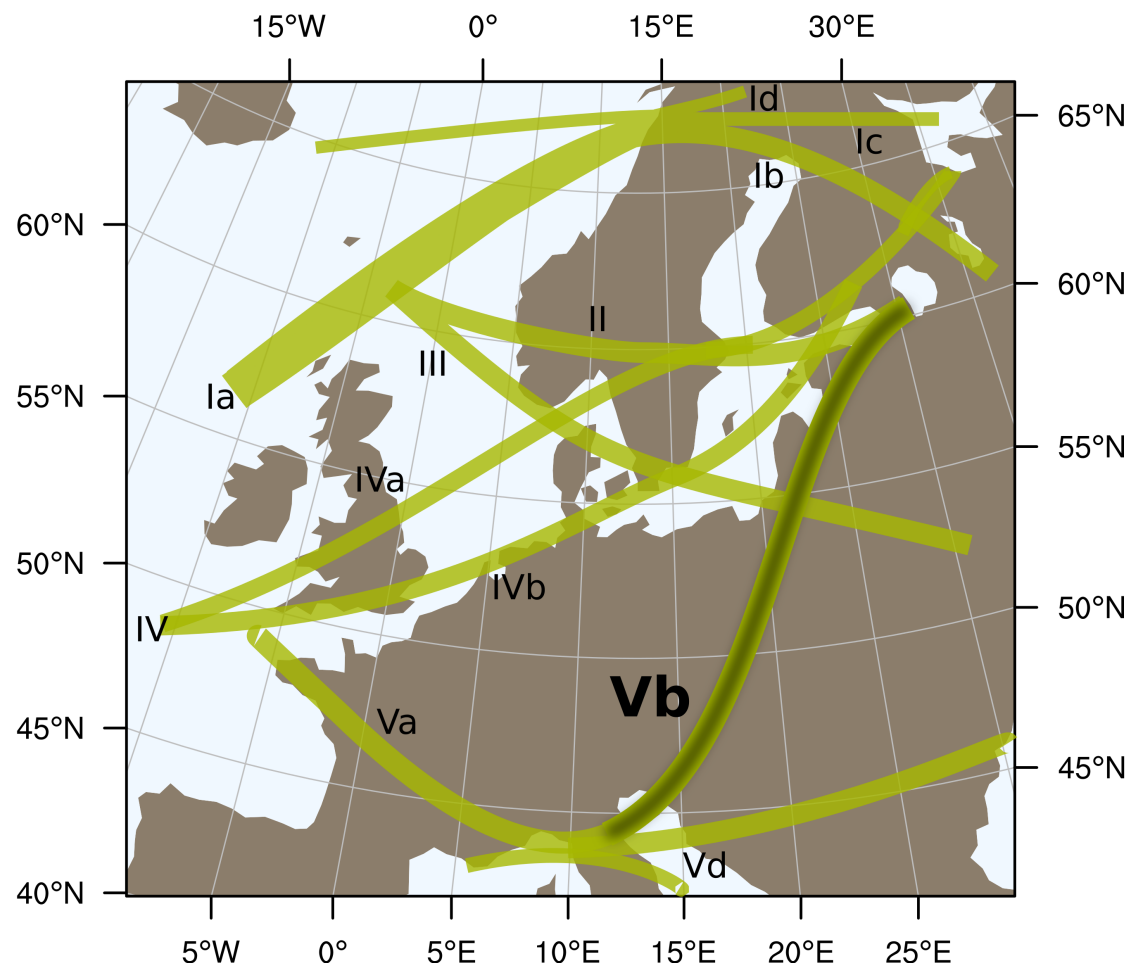


Figure 1.1: The green lines show all cyclone tracks named by W. J. van Bebber. The darker green line represents the Vb trajectory. Source: M. Messmer, personal communication, based on van Bebber (1891).

1.1 Prominent Vb-type cyclones and their implications

Vb-type cyclones were associated with substantial floodings in central Europe (Mudelsee et al., 2004). In September 1993, the town of Brig (CH) was hit by heavy precipitation caused by a Vb-type cyclone. Brig is a Swiss alpine municipality in the Canton of Valais, that has a population of 12,000 people. After several weeks of continuous and moderate precipitation and three days of heavy rain, the river Saltina overflowed on September 24. As a result, the downtown of Brig was covered with wreckage and debries, two women died and the financial damage amounted to CHF 650 million. (<http://www.planat.ch/en/images-details/datum/2011/06/21/hochwasser-brig-1993/>).

From July 4 to July 7, 1997 several weather stations in Czech Republic, eastern Germany, and southern Poland measured maximal values of accumulated precipitation between 215 mm and 400 mm. This caused the water level of the River Oder to rise. Two weeks later another low pressure system arrived on a Vb trajectory, with another 100-250 mm/day of precipitation over Germany and parts of the Czech Republic. This triggered in combination with the already saturated soils strong floodings and damages of about DM 648 million (Graefe and Hegg, 2004).

In the beginning of August 2002, two consecutive rain events led to floods in Germany, Austria and the Czech Republic. From August 6 to August 7 heavy precipitation saturated the soils in Bavaria (DE), Boehmen (CZ), and Austria. This led to first floodings in the drainage basin of the river Danube. However, the main catastrophe was yet to come. A second precipitation event occurred, which was associated with a Vb-type cyclone. The major activity in terms of precipitation started on August 10 in the eastern part of Switzerland and southwestern Germany. The weather station Zinnwald-Georgenfeld, which is located south of Dresden, measured 312 mm within 24 hours. Furthermore, this flood caused an economical damage of about EUR 17.5 billion in central Europe (Grünewald et al., 2004).

From August 19 to August 23, 2005 an extended low pressure system formed over the Gulf of Genoa and moved over the northern part of Italy towards the Ukraine. From August 20 to August 22, 2005 some alpine parts of Switzerland received more than 200 mm of accumulated rain (Fig. 1.2). This amount of rain was unprecedented for many weather stations on the northern side of the Swiss Alps (Bezzola et al., 2008). The consequences were substantial flooding, landslides, financial damages of about CHF 2.5 billion, and even casualties (MeteoSchweiz, 2006).

More recently, May 2013 was anomalously cold and wet. Until the end of May continuous precipitation saturated the soils in large parts of eastern Germany, especially in Sachsen. Simultaneously, an extended high pressure system over the eastern Atlantic established a cold-air trough over the western part of Europe. In the beginning of June a Vb-type cyclone moved from the Adriatic Sea around the

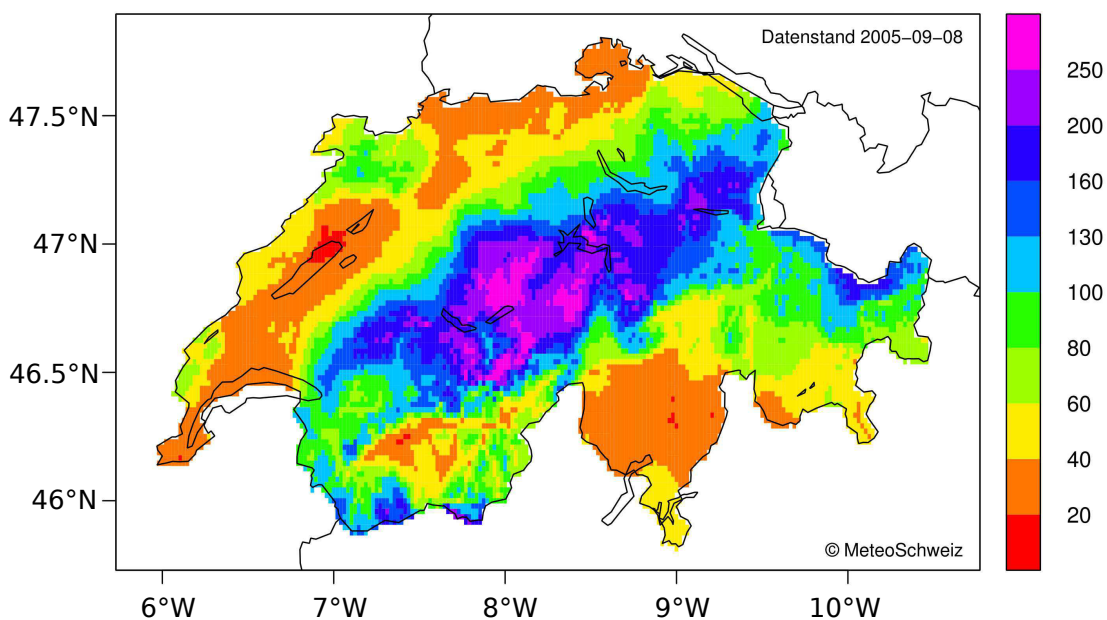


Figure 1.2: Observational distribution of precipitation in mm accumulated between August 20 and August 22, 2005 in Switzerland. Source: Frei (2005).

Alps to Austria and south-eastern Germany. The relatively warm and wet air from the Mediterranean Sea was forced to rise on the cold-air trough and produced large amounts of precipitation. Thereby, the weather station of Garsebach (Landkreis Meissen, Sachsen) in Germany received between May 30 and June 2 more than 200 mm of rain. The subsequent flooding produced accumulated costs of about EUR 2 billion (Mitzschke, 2013).

1.2 Theoretical background

In meteorology, the traditional concept to describe the formation of a mid-latitude cyclone is the concept of baroclinic instability. In a baroclinic atmosphere the density of an air parcel depends on pressure and temperature, while in a barotropic atmosphere the density of an air parcel only depends on the pressure (Holton, 1992). In the northern mid-latitudes the globally strongest meridional temperature gradients are present. Since these temperature gradients are associated with density and hence, pressure gradients, a so-called thermal wind from west to east is established, which increases with increasing height. As a result, there is a band of very strong winds established below the mid-latitude tropopause. This band of very strong winds is called the jet stream. The strength of the zonal winds including the jet stream is also longitude dependent. In this regard, there are mean increases in zonal wind speed at the eastern coasts of America and Asia due to thermally induced pressure differences between land and water. Hence, in mean there are troughs of the 500 hPa geopotential height (gph) at the eastern coasts of America and Asia. The pressure

differences between land and water as well as the influence of the orography act as perturbations to the flow, which induce large horizontal planetary waves (Rossby waves). The term instability refers to the fact that these perturbations induce waves that are growing in time. Since these large scale waves propagate horizontally from West to East, they are fluctuating from North to South.

This fluctuation from North to South changes the relative vorticity of the associated air parcels. To understand this the properties of absolute vorticity have to be considered. Absolute vorticity is the sum of planetary and relative vorticity. The planetary vorticity arises from longitudinal changes in angular speed of the rotating earth. Since absolute vorticity is a constant in time it follows that a northward shift of an air parcel lowers its relative vorticity. This results in upper level divergence and upward movement of air downstream of a trough, which induces cyclogenesis from the tropopause down to the surface (Martin, 2006).

As described, the concept of baroclinic instability uses pressure and temperature to characterize the genesis of a low pressure system. However, since herein sensitivity experiments with Mediterranean SSTs are performed it is more convenient to have a concept at hand that considers cyclogenesis in terms of diabatic processes, where the concept of potential vorticity (*PV*) becomes very useful. Therefore, this section outlines how the *PV* perspective on atmospheric dynamics is defined.

***PV* perspective**

PV is defined as follows:

$$PV = \frac{1}{\rho} \zeta^a \cdot \nabla \Theta, \quad (1.1)$$

where ρ is the density, ζ^a is the absolute vorticity, and $\nabla \Theta$ is the vertical gradient of potential temperature. The handling of *PV* usually involves the usage of the so called potential vorticity unit ($1 \text{ PVU} = 10^{-6} \text{ Ks}^{-1} \text{ kg}^{-1} \text{ m}^2$). The 2 PVU isosurface is typically defined as the dynamical tropopause. Hence, values above this threshold are related to stratospheric air, whereas values below are related to tropospheric air (Hoskins et al., 1985).

Equation 1.1 shows that *PV* is a function of the gradient of potential temperature and absolute vorticity. The absolute vorticity is higher towards the poles and the gradient of potential temperature is stronger in the stratosphere, where stratification is much stronger. Hence, very high values of *PV* can be found in the polar stratosphere.

The genesis of an extratropical cyclone can be considered as an interaction of three positive *PV* anomalies: An upper level stratospheric intrusion, mid- to low-tropospheric diabatically produced *PV*, and a warm anomaly at the surface acting as a surrogate *PV* anomaly (Campa and Wernli, 2012).

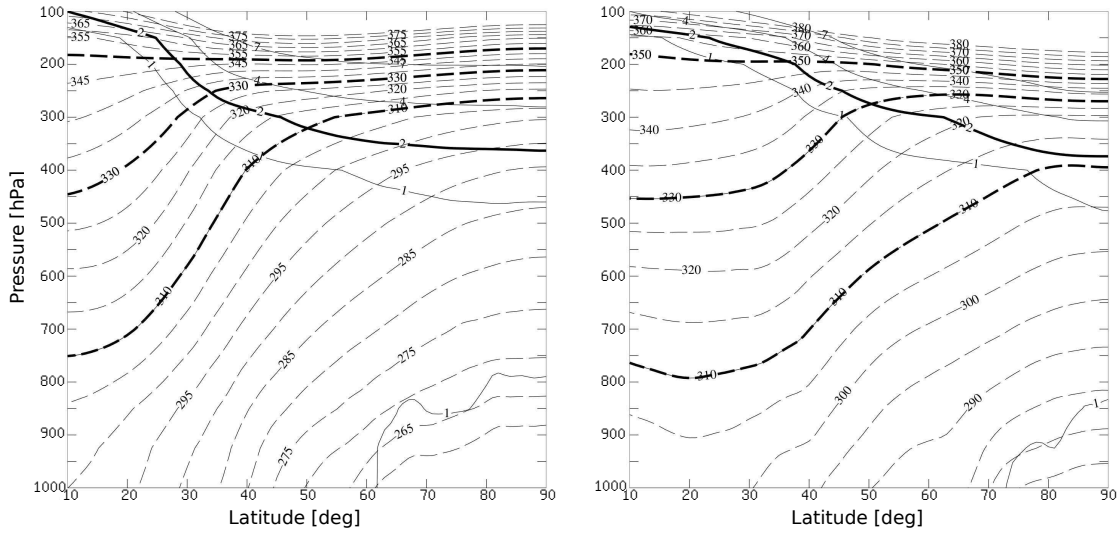


Figure 1.3: Zonal-mean climatological distribution of potential temperature (dashed contours) and PV (solid contours for 1,2,4, and 7 PVU) in the northern hemisphere winter (left) and summer (right). The 2 PVU contour, indicating the dynamical tropopause, and the 310, 330, and 350 K isentrope are indicated by bold lines. Figure from Wernli and Croci-Maspoli (2013).

In upper level stratospheric intrusions, stratospheric air with high values of PV can be imported into the troposphere along the isosurfaces of potential temperature, where adiabatic and frictionless flow is present (Fig. 1.3). Thereby, PV is materially conserved for adiabatic and frictionless flow. In summer, this isosurface is preferably between 320 K and 340 K warm, because the isosurfaces of potential temperature that are located within this range extend from the stratosphere in polar regions to the middle of the troposphere at the equator. Such intrusions of stratospheric air are called PV streamer, and induce a positive PV anomaly below the mid-latitude tropopause, and hence trigger cyclonic rotation from the tropopause to the surface, which is weakened with decreasing height. The cyclonic rotation at the surface leads to surface advection of southern warm air to an eastward position relative to the initial cyclonic wind field. The positive temperature anomaly at the surface induces a further positive PV anomaly, and hence another cyclonic wind field at the surface. As a result, this establishes a low-level cyclone, whose center is slightly ahead of the advancing upper level PV anomaly.

PV can also be destroyed or produced throughout the troposphere due to diabatic processes such as latent heating or phase changes of water (Hoskins et al., 1985). The equation that describes the vertical change of PV due to diabatic heating reads as follows:

$$\frac{D}{Dt} PV \simeq \frac{1}{\rho} \zeta^a \frac{\partial \dot{\theta}}{\partial z} \quad (1.2)$$

Thereby, ρ is the density, ζ^a is the absolute vorticity, and $\dot{\theta}$ is the diabatic heating rate in Ks^{-1} , and $\frac{\partial\dot{\theta}}{\partial z}$ is its vertical gradient. In the northern hemisphere ζ^a is greater than zero. Thus, it follows from Eq. (1.2) that PV is produced where $\frac{\partial\dot{\theta}}{\partial z} > 0$ and destroyed where $\frac{\partial\dot{\theta}}{\partial z} < 0$. It has to be noted that Eq. (1.2) quantifies the material change of PV . Hence, it quantifies the change of PV following the vertical motion of an air parcel (Wernli and Davies, 1997).

Considering all the aforementioned processes PV anomalies are able to become vertically aligned, which forms a so-called PV tower, that is westward tilted from the surface going upwards. Furthermore, a PV tower can be considered a fully developed mid-latitude cyclone with an eastward movement.

1.3 State of knowledge

As stated above, the Vb-type trajectory starts in the Mediterranean area. Since one of the aims of this study is to investigate the sensitivity of Vb related precipitation to SSTs in the MB it is interesting to know a bit more about projections on possible future climates in the MB. In this regard, one important statement is made by Somot et al. (2006), who says that the SST over the entire MB is expected to warm until 2100 homogeneously by an average of about 3 °C.

Also Lionello et al. (2002) stated that the ongoing warming of the global climate system leads to a warming of the MB, and that increased SSTs in the MB are likely to cause increased intensity in cyclogenesis. To test this hypothesis, they analyzed possible changes in the frequency and intensity of cyclones in the MB due to a doubling of the atmospheric CO₂ concentration. Thereby, the ECHAM atmospheric circulation model was used. The reliability of the control (ctrl) simulation, for current climate conditions, was assessed with the ERA-15 data set. The conclusion of this study is a reduced cyclonic activity over the entire MB in the 2×CO₂ simulation due to a northward shift of the storm track. However, they also pointed out a more likely extreme intensity of cyclones in the MB due to a reinforcement of diabatic processes such as latent heat release (Lionello et al., 2002).

It is conceivable that cyclones that are more intense produce more precipitation. In this regard, from a climatological point of view, precipitation in the MB peaks in winter (Lionello et al., 2006). Therefore, Lionello and Giorgi (2007) carried out 30-year climate simulations with a RCM, where they considered the period 2071-2100 under the SRES scenarios A2 and B2, and compared them with the control period 1961-1990. This was done to examine possible changes in winter precipitation and the links to cyclonic activity in the MB. The RCM uses a spatial resolution of 50 km with a model domain, which covers the European continent and adjacent oceans. They found an increase in winter precipitation over Europe and the northern MB for both the A2 and the B2 scenarios. In contrast to the results of Lionello et al. (2002),

these changes in precipitation in both scenarios could now be linked to stronger cyclonic activity in the north-western parts of the MB (Lionello and Giorgi, 2007).

Furthermore, Raible et al. (2010) investigated the winter climate in the MB from 2071-2100 with respect to the SRES A2 scenario and compared the results with the ctrl simulation from 1961-1990, which was evaluated with reanalysis data. The simulations are performed with the ECHAM5 model, which is a spectral model with a horizontal resolution of T106 (approximately $1.125^\circ \times 1.125^\circ$). As a result, they found that the hydrological cycle will be substantially affected, especially in winter. There is a significant decrease in the number of cyclones simulated in the western and central part of the MB for the future. This produces a decrease of precipitation rates over the western Mediterranean under climate change conditions (Raible et al., 2010).

Other studies tried to gain insight into cyclonic activity through the use of tracking tools. For example Hofstaetter and Chimani (2012) tracked low pressure systems in reanalysis data from ERA-40 and ERA-interim, to determine different track types over central Europe from 1961 to 2002. Their tracking approach detects isolated minima in the bandpass filtered 700 hPa geopotential height field. The results of the study show that the common Vb cyclone track has a mean occurrence of 3.5 times per year. The probability of occurrence is largest in spring, with a second maximum in autumn. Moreover, they found no temporal trend of Vb-type cyclones throughout the investigated period.

Also the problems and agreements of different tracking schemes have been analyzed. In this respect, Neu et al. (2013) compared 15 cyclone detection and tracking methods in order to assess their similarities and differences. To do so, they used the same input data set, namely ERA-interim with 6-hourly time steps and a spatial resolution of 1.5° . The analyzed time covers the period from 1 January, 1989 to 31 March, 2009. As a result, they found good qualitative agreement in the spatial structure of the identified cyclones. However, for the western and central Mediterranean they found considerable differences in the exact locations of the cyclone positions, resulting in different minimum central pressures. Thereby, all schemes except for one agree on the time of the minimum central pressure, which varies by 9 hPa. With regard to the number of cyclones there are also remarkable quantitative differences between the considered tracking schemes. More precisely, cyclones found in northern hemisphere winter vary from about 6000 to 21000, while the number of found cyclones in summer varies from 5000 to 28000.

In the same regard, Raible et al. (2008) investigated the differences and agreements between the tracking schemes of Blender et al. (1997), Murray and Simmonds (1991), and Wernli and Schwierz (2006), always using the ERA-40 reanalysis. Furthermore, they analyzed the differences between the NCEP/NCAR reanalysis, and the ERA-40 reanalysis, to provide an estimate of uncertainty due to different input data sets for the period 1961-1990. Both data sets were interpolated to a regular grid of

2.5°, with a time resolution of 6 h. As a result, they found differences in both the number of cyclones and the cyclone intensity. More and deeper cyclones are found in ERA-40. This was attributed to the spatial resolution of the model that is used to obtain ERA-40, which is higher than the resolution of the model used for the NCEP/NCAR reanalysis. Furthermore, the interannual variability of the number of cyclones as well as the extreme cyclone intensity is significantly correlated between the data sets. However, the extreme cyclone intensity shows higher correlations, which suggests that the number of cyclones might not be as robust as the extreme cyclone intensity to describe the interannual variability. Also the three considered tracking schemes show high correlations in the interannual variability of the number of cyclones. Some cyclone tracks are not detected by one or more schemes. Thereby, especially the tracking scheme by Blender et al. (1997) tends to find more cyclones. In this respect, one main conclusion of the study is that a potential user of a cyclone detection and tracking method always should proceed with caution, because the interpretation of cyclone tracks may depend on the scheme or the specific parameter setting that is chosen by the user.

All of the aforementioned studies on Mediterranean cyclones are either done with Global Climate Models (GCM) or RCMs, which are run with rather coarse spatial and temporal resolutions. These coarse resolutions are not appropriate to investigate local impacts of Vb-type cyclones in the Alps, where a complex orography is present. In this respect, a dynamical downscaling of Vb-type cyclones with a RCM that runs with higher resolutions is yet to be done.

1.4 Objectives

To assess potential future changes in Vb-type cyclones, it is important to understand the underlying mechanisms of their genesis and intensification as well as the connection to the underlying SSTs in the MB. To make a first step in this direction, a statistical analysis of Vb-type cyclones will be performed to assess the frequency and the impact of these phenomena in terms of moisture transport and extreme weather events. Thereafter, a RCM will be used to design specific sensitivity experiments with respect to the underlying SSTs in the Mediterranean.

The Vb-type cyclone that will be used for the sensitivity experiments occurred in August, 2005. The procedure of this low pressure system is comprehensively described by a report published by the Federal Office of Meteorology of Switzerland (MeteoSchweiz, 2006). According to this report, a high altitude low pressure system with core over the Netherlands could be identified on August 19, 2005. This situation triggered a south-westerly flow at upper levels over the western Mediterranean. During this time, convective precipitation occurred, which only led to locally restricted problems. On August 20, the low pressure system aloft was still discernable over the Benelux Union. However, the main cyclonic activity was now shifted to North Italy over the Gulf of Genoa, where a secondary surface low developed. Simultaneously, the cyclonic activity aloft shifted over the Mediterranean as well. On

August 21, the surface low pressure system over the Gulf of Genoa intensified, and the two systems merged. This led to strong cyclonic activity and north-easterly winds in Switzerland, which produced heavy precipitation and flooding. The cyclonic activity aloft was strongest in the night to August 22. In this time, the whole system moved a bit towards east and was located on August 22 (12 UTC) over the Adriatic Sea. This also caused the winds at upper levels to turn to northerly direction, which increasingly pressed humid air towards the Alps. On August 23, the low pressure system was located over Hungary. The most humid air masses were now located outside of Switzerland, whereas southern Germany and Austria were still affected by heavy precipitation (MeteoSchweiz, 2006).

The objectives of this study are:

- To characterize a climatology of Vb-type cyclones in terms of frequency, intensity and impacts on precipitation in Switzerland, Austria and southern Germany.
- To perform a RCM simulation of the Vb-type cyclone that occurred in August, 2005, and use it to gain insight into the underlying processes.
- To use the obtained RCM simulation for a number of sensitivity experiments to investigate the impacts of changing SSTs in the Mediterranean on precipitation in Switzerland.
- To gain insight into the underlying physical processes that are responsible for possible changes in precipitation.

Chapter 2

Regional model, input data, and experimental design

Precipitation is generated through a number of processes that are highly variable in space and time. Therefore, it is important that a model that is used for precipitation analysis is able to resolve these processes. GCMs only use initial conditions to compute the physically coherent development of weather and climate on a global scale. To do so, they require large computational resources and are restricted in terms of the spatial resolution. RCMs simulate a limited area domain, which allows to increase the spatial resolution. However, they not only demand initial but also boundary conditions that either come from a GCM or from reanalysis data. This approach allows a RCM to generate output of higher spatial resolution, which is needed to accurately simulate the processes that are related to the formation of precipitation.

In this study, the model simulations are performed with the Weather Research and Forecasting Model (WRF, Skamarock et al., 2008). WRF is a mesoscale meteorological model, which can be used for both research and operational purposes. Furthermore, WRF is the successor modeling system of the Mesoscale Meteorology Model 5 (MM5, Grell et al., 1994). In a first step the system components of the WRF model are introduced. Then, the herein used data sets are presented, followed by a description of the WRF preprocessing system. Finally, the experiments used in this study are presented.

2.1 System components of the WRF model

The regional model WRF consists of different system components: vertical and horizontal coordinates, a dynamical core, a number of parametrizations of several sub-grid processes, and a soil model. In this section, the particular setting of system components used in this study is presented.

Vertical and horizontal coordinates

In the vertical, the dynamical core of WRF uses a terrain-following hydrostatic-pressure mass coordinate (Fig. 2.1, Skamarock et al., 2008).

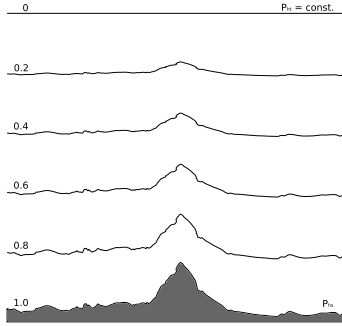


Figure 2.1: Schematic representation of vertical η -levels between 0 and 1. Figure from Kilic (2012).

This vertical coordinate is denoted by η and is defined as:

$$\eta = (p_h - p_{ht}) / \mu, \text{ where } \mu = p_{hs} - p_{ht}, \quad (2.1)$$

where p_h is the hydrostatic component of the pressure, whereas p_{hs} and p_{ht} are the surface and top pressure, respectively.

In Eq. 2.1, $\mu(x,y)$ is the mass per unit area within a column in the model domain at coordinates (x,y) . The opportune flux form variables are:

$$\mathbf{V} = \mu \mathbf{v} = (U, V, W), \quad \Omega = \mu \omega, \quad \Theta = \mu \Theta \quad (2.2)$$

where $\mathbf{v} = (u, v, w)$ are the covariant velocities in the two horizontal and vertical directions, respectively, and ω is the contravariant vertical velocity (Skamarock et al., 2008).

Horizontally, the WRF model uses the Arakawa-C grid staggering (Fig. 2.2). The horizontal components of velocity (u - and v -wind components) are defined along the normal cell face and represent an average over each cell face, whereas the thermodynamic variables (e.g. perturbation potential temperature) are defined at the center of the grid cell and represent an average throughout the cell.

A simulation uses a main grid and can be extended with several inner nested grids. Every nested domain can either be a static domain or a moving nest. The 1-way

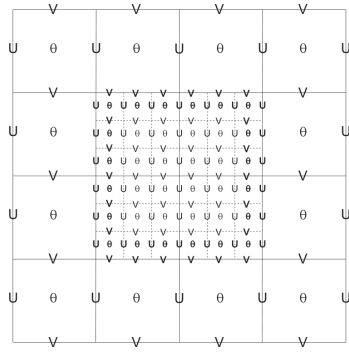


Figure 2.2: Arakawa-C grid: Horizontal grid comprised of a parent domain and an embedded nest domain with a 3:1 grid size ratio. Figure from Skamarock et al. (2008).

and 2-way grid nesting options are the two possibilities in which nested domains can interact. In either case, the boundary conditions for the finer child grids are interpolated from the coarse grid forecast. Hence, only the grid points that belong to the coarse parent grid are considered. In the 1-way grid nesting option this is the only direction of information exchange between the grids. Thus, the information only goes from the coarse grid forecast to the fine grid. For the 2-way nesting the solutions of the coarse grid points, which are congruent with grid points of a fine grid, are replaced with the spatially averaged solution of the fine grid, which may be different due to the higher resolution of the fine grid. These newly assigned parent grid points are then together with the parent grid points that are located outside of the considered fine grid, the basis for the interpolation, which lead to the boundary conditions of the fine grid. In this study, the 2-way grid nesting option is used.

Dynamical core

The dynamical core of WRF solves the compressible and nonhydrostatic Euler equations:

$$\partial_t U + (\nabla \cdot \mathbf{V} u) - \partial_x(p\partial_\eta\phi) + \partial_\eta(p\partial_x\phi) = F_U \quad (2.3)$$

$$\partial_t V + (\nabla \cdot \mathbf{V} v) - \partial_y(p\partial_\eta\phi) + \partial_\eta(p\partial_y\phi) = F_V \quad (2.4)$$

$$\partial_t W + (\nabla \cdot \mathbf{V} w) - g(\partial_\eta p - \mu) = F_W \quad (2.5)$$

$$\partial_t \Theta + (\nabla \cdot \mathbf{V} \Theta) = F_\Theta \quad (2.6)$$

$$\partial_t \mu + (\nabla \cdot \mathbf{V}) = 0 \quad (2.7)$$

$$\partial_t \phi + \mu^{-1}[(\mathbf{V} \cdot \nabla \phi) - gW] = 0 \quad (2.8)$$

The diagnostic relation for the inverse density is given as:

$$\partial_\eta \phi = -\alpha \mu, \quad (2.9)$$

and the equation of state:

$$p = p_0 (R_d \Theta / p_0 \alpha)^\gamma. \quad (2.10)$$

In Eq. (2.3) - (2.5), (2.9), (2.11) and (2.12), the subscripts x, y and η denote the directions of the derivatives,

$$\nabla \cdot \mathbf{V}a = \partial_x(Ua) + \partial_y(Va) + \partial_\eta(\Omega a) \quad (2.11)$$

and

$$\mathbf{V} \cdot \nabla a = U \partial_x a + V \partial_y a + \Omega \partial_\eta a, \quad (2.12)$$

where a represents a generic variable. $\gamma = \frac{c_p}{c_v} = 1.4$ stands for the ratio of the heat capacity for dry air, R_d is the gas constant for dry air, and p_0 represents a reference pressure (typically 10^5 Pa). The right-hand-side terms F_U , F_V , F_W and F_Θ are forcing terms arising from model physics, turbulent mixing, and the rotation of the Earth. Furthermore, Θ is the potential temperature, $\phi = gz$ (the geopotential), p (the pressure), and $\alpha = 1/p$ (the inverse density). Thereby, wind, potential temperature, perturbation geopotential, and perturbation surface pressure are the prognostic variables (Skamarock et al., 2008).

The dynamical core of WRF provides two dynamics solvers: the advanced research WRF (ARW) solver, which mainly was developed at the National Center for Atmospheric Research (NCAR) and the Nonhydrostatic Mesoscale Model (NMM) solver, mainly developed at the National Center for Environmental Prediction (NCEP). Herein, the ARW solver is used (Skamarock et al., 2008).

Parametrizations

The dynamical core treats grid scale processes of temperature, wind, pressure, and geopotential in time. However, there are important sub-grid processes that can not

be resolved with the resolution of the RCM grid by the dynamical core. As a consequence, several assumptions have to be made that allow to take these processes into account. This is done through a number of parametrizations. The parametrizations are available for different categories such as convective/cumulus, microphysics, planetary boundary layer (PBL), land surface model, and radiation (Skamarock et al., 2008).

Convective/cumulus scheme

Convection and cumulus processes are parametrized by the convective/cumulus schemes. These schemes are responsible for the sub-grid scale effects of convective and shallow clouds. In this respect, they represent vertical fluxes due to unresolved up- and downdrafts (Skamarock et al., 2008). Cumulus schemes aim to identify the presence of atmospheric large-scale conditions that support the development of convective activity. Thereby, they are designed to drive the model atmosphere towards a convectively adjusted state. This convectively adjusted state is either predefined, or is computed using a bulk or spectral cloud model (Bechtold et al., 2001).

Herein, the Kain-Fritsch (KF) scheme is used (Kain, 2004). The KF scheme is a mass flux parametrization. It uses the Lagrangian parcel method (e.g., Simpson, 1983; Wiggert, 1969), including vertical momentum dynamics (Donner, 1993), to estimate whether any existing instability will become available for cloud growth, and to estimate the properties of any convective clouds (Kain, 2004). The basic procedure of the KF scheme can be divided in a trigger function, a mass flux formulation, and closure assumptions.

The task of the trigger function is to identify potential updraft source layers (USL) for convective clouds (Kain, 2004). Given the atmospheric large-scale conditions it defines where and when the scheme is activated. Thereby, vertically adjacent layers, starting on the surface, are mixed until a depth of 60 hPa. This forms the first potential USL. Now, within this mixed layer, the temperature and height of an air parcel that stems from this USL at its lifting condensation level (LDL) is computed. This allows to compare the temperature at the LDL (T_{LDL}) with its surrounding temperature at the height level of T_{LDL} . This comparison indicates the potential cloud depth that this air parcel is able to produce. If the probable cloud thickness is smaller than 3 km the procedure is repeated at the next higher 60 hPa mixed layer, and so on (Bechtold et al., 2001). Besides, the background vertical motion in the atmosphere can transport an air parcel, which would not have positive buoyancy at LDL, to higher levels (Kain, 2004). Therefore, a temperature perturbation with respect to the grid-resolved vertical motion is added to T_{LDL} . The procedure is repeated until a height of 300 hPa is reached. This set of measures, as a function of the minimum cloud depth, composes the trigger function and is responsible for the start of the mass flux formulation.

The mass flux formulation is an updraft function that considers detrainment and entrainment rates of (moist) air in a column of the atmosphere. It accounts for

environmental mass fluxes and computes the thermodynamic characteristics of the updraught at LDL. This is done for all the convective air parcels identified by the trigger function. The detrainment and entrainment rates are considered to be inversely proportional. Hence, high entrainment rates are favored by high parcel buoyancy and moist environments, whereas high detrainment rates are favored by low parcel buoyancy and dry environments. Convective updrafts are driven by condensation of water vapor and convective downdrafts are driven by the cooling effect of evaporation of condensate that is generated within the updraft. The surrounding mass fluxes are required to conserve the mass of an air column, so that the net convective mass flux at any level in the column is zero.

Finally, the closure assumption is used to control the intensity of convection (Bechtold et al., 2001). Thereby, all the convective available potential energy (CAPE) in a grid element is removed within an adjustment time τ . This adjustment time is between 0.5 hour and 1 hour for deep convection and 3 hours for shallow convection. Subsequently, enthalpy and mixing ratios of the surrounding air are adjusted, whereas the updraft and downdraft values of the thermodynamic variables remain unchanged. Then, a new value of CAPE is computed by using undilute parcel ascent. Finally, the amount of convection, cumulus formation, and precipitation for a particular situation is estimated (Bechtold et al., 2001).

Microphysics scheme

The microphysics schemes include explicitly resolved water vapor, cloud and precipitation processes on the sub-grid level. The schemes are carried out at the end of a time step as an adjustment process. Hence, microphysics schemes do not provide tendencies. This is due to the notion that condensation adjustment should take place at the end of the time step to make sure that the final saturation balance is accurate for the updated temperature and moisture (Skamarock et al., 2008).

Herein, the New Thomson et al. scheme is used (Hall et al., 2005). The scheme was developed to represent the major physical processes of precipitation development. It involves ice, snow, and graupel processes and is suitable for high resolution simulations in the mid-latitudes (Skamarock et al., 2008).

Planetary boundary layer

The planetary boundary layer (PBL) schemes are concerned with vertical sub-grid-scale fluxes that are produced by eddy transport in the whole atmospheric column, not just the PBL (Skamarock et al., 2008). When a PBL scheme is activated, vertical diffusion is deactivated with the assumption that the PBL scheme will handle this process. The PBL schemes compute the flux profiles within the mixed boundary layer and the stable layer. Thereby, these schemes provide atmospheric tendencies of temperature, moisture (including clouds), and horizontal momentum in the whole atmospheric column.

Herein, the Yonsei University (YSU) PBL scheme is used. It represents sub-grid scale fluxes that are due to non-local gradients. Hence, it is a vertical diffusion package with a nonlocal turbulent mixing coefficient in the PBL (Hong and S-W, 2007). The mixing in the PBL is produced as a function of the virtual potential temperature at height h and horizontal wind speed at height h .

Soil model

Moreover, a soil model is employed to incorporate heat and moisture fluxes over land and sea ice points (Skamarock et al., 2008). WRF computes these fluxes using the information from other schemes such as the microphysics and convective scheme.

Herein, the MM5 5-layer thermal diffusion model is used. The energy budget of this soil model includes radiation, and sensible and latent heat flux. Also, snow cover, soil moisture, and land use are taken into account (Skamarock et al., 2008).

Radiation

Radiation schemes provide atmospheric heating due to both radiative fluxes and surface downward long and shortwave radiation for the ground heat budget (Skamarock et al., 2008). Longwave radiation consists of infrared or thermal radiation absorbed and emitted by gases and surfaces. Shortwave radiation is comprised of visible and surrounding wavelengths that make up the solar spectrum.

In this study, a new version of the longwave rapid radiative transfer model (RRTM) that includes the Monte Carlo independent column approximation (MCICA) method of random cloud overlap is used (Mlawer et al., 1997; Wang et al., 2010). The RRTM scheme is a spectral band scheme using the correlated- k method. It accounts for longwave processes due to water vapor, ozone, CO₂, and trace gases as well as cloud optical depth using pre-set tables (Skamarock et al., 2008).

For the shortwave radiation, the MM5 (Dudhia) scheme is used, which is based on Dudhia (1989). It has a downward integration of solar flux, accounting for clear-air scattering, water vapor absorption, cloud albedo, and absorption. It uses look-up tables for clouds and has an option to account for terrain slope and shadowing effects on the surface solar flux (Skamarock et al., 2008).

2.2 Reanalysis and observational data

A reanalysis data set combines observational data and model output using statistical assimilation techniques to yield a coherent atmospheric data set. Since reanalysis data include observations it can be considered to be more reliable than the output of a state-of-the-art GCM. Hence, the input data for the Vb statistics as well as the boundary- and initial conditions for the regional model are provided by reanalysis data.

Observational data for reanalysis products include different sources: surface observations, ships, rawinsondes, aircrafts, and satellites. The atmospheric model is used for both interpolation of values from observation points to the grid points of the reanalysis and projections to the next time step where observations are available. Deviations between the modeled projections and the interpolated observations are corrected using a statistical data assimilation method, which is kept unchanged over the reanalysis period. This is important to maximize the consistency of the data for the whole reanalysis period. In doing so, physical coherent and reliable atmospheric data sets are obtained (Kistler et al., 2001).

ERA-interim reanalysis

For the statistical analysis performed in the first part of this study, and for the evaluation of the WRF ctrl simulation, the ERA-interim data set is used. ERA-interim is a reanalysis of the period from 1979 to the present (Dee et al., 2011). The ERA-interim atmospheric model uses a T255 spectral resolution for the basic dynamical fields and a reduced Gaussian grid with uniform 79 km spacing for surface and other grid point fields such as SST and mean sea level pressure. Furthermore, ERA-interim offers several cloud parameters and a representation of the hydrological cycle (Berrisford et al., 2009). According to Dee et al. (2011), ERA-interim is produced with a sequential data assimilation scheme, advancing forward in time using 12-hourly analysis cycles. In each cycle, available observations are combined with prior information from a forecast model to estimate the evolving state of the global atmosphere and its underlying surface. This yields data of different temporal and spatial resolutions (Dee et al., 2011). For parts of the herein presented Vb climatology, and for the evaluation of the Vb-type cyclone as simulated by WRF, gph fields that start in March 1979 and end in February 2009 are used. These data have a 6-hourly temporal resolution on a regular $1.5^\circ \times 1.5^\circ$ grid. Also for the Vb climatology, total precipitation data with a 6-hourly temporal resolution on a regular $1^\circ \times 1^\circ$ grid are used.

NCEP-NCAR reanalysis

The reanalysis data set used to drive the WRF simulations is the NCEP-NCAR reanalysis (Kistler et al., 2001). This data set covers the years 1958 - 2008. For the reanalysis the NCEP global spectral model is used. This model operates with 28 vertical sigma levels and has a resolution of T62, which is equivalent to a horizontal resolution of about 210 km (Kistler et al., 2001). The assimilation system used in the NCEP-NCAR reanalysis is a three-dimensional variational (3DVAR) scheme, which is cast in spectral space (Kalnay et al., 1996). Herein, data at 6 hourly temporal resolution on a $2.5^\circ \times 2.5^\circ$ grid is used.

Observations

To quantitatively assess the precipitation output in Switzerland of the WRF ctrl simulation, observational data of precipitation by MeteoSwiss is used. These data

are always taken at 05:40 am from rain gauges that are distributed over Switzerland as visible on Fig. 3.2. Hence, each measurement represents the precipitation of the last 24 hours. Herein, the used rain observations cover the period from August 20 to August 23, 2005.

2.3 WRF preprocessing system

The WRF Preprocessing System (WPS) is a set of three tools to prepare the driving data so that it can be used by the regional model. WPS consists of geogrid, ungrid, and metgrid (Fig. 2.3). Each of the three elements performs one stage of the preparation (Wang et al., 2010).

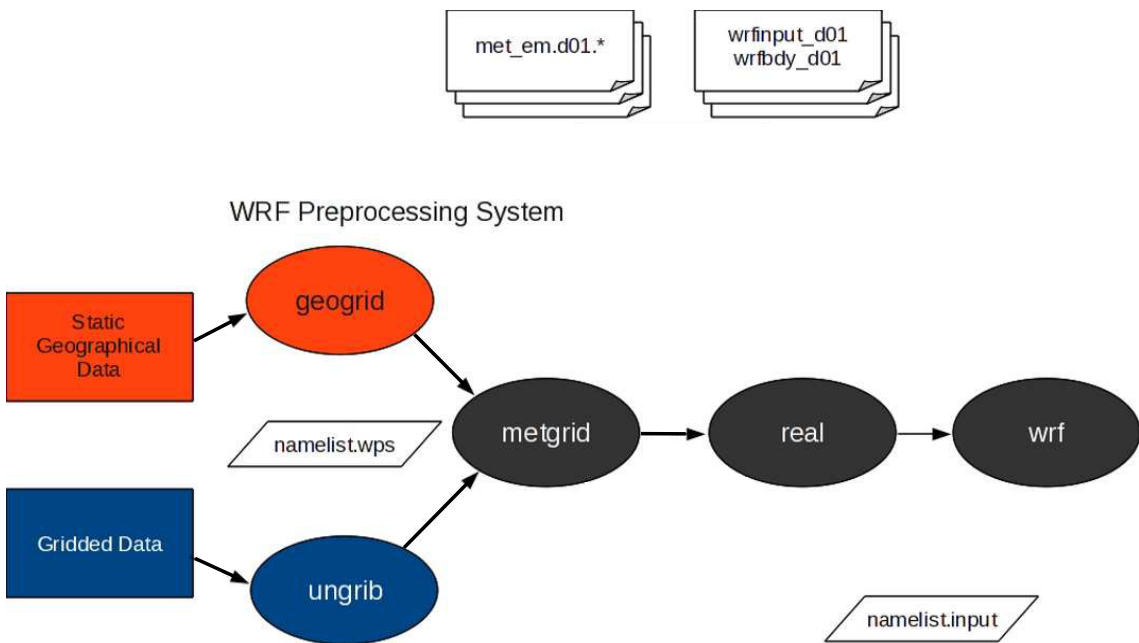


Figure 2.3: Flowchart of WPS components, their input sources, and interactions.

geogrid establishes the simulation domains interpolating the surface data, which is static in time, to the grids of the domains. The domains and grids for the simulations are established using the information given in the corresponding namelists (Appendix B), whereas the surface data is generated by an interpolation process using a database that is downloaded on the WRF website. The surface data consists of soil categories, land use category, terrain height, annual mean deep soil temperature, monthly vegetation fraction, monthly albedo, maximum snow albedo, and slope category (Wang et al., 2010).

As discussed above, the regional model needs 2 and 3-dimensional atmospheric input data such as temperature, pressure, or humidity. These data are demanded by

the model as GRIB files and can stem from different sources such as the NCEP-NCAR reanalysis or ERA-interim. Thereby, GRIB stands for GRIded Binary. It is a standardized, compressed binary data format that is usually used for meteorological purposes. GRIB files usually contain more fields than are needed to initialize WRF. Therefore, the utility `ungrib` extracts the needed data and converts it to common intermediate format files. In these intermediate files common field names are assigned to same fields from different sources, which can be recognized by WRF. For the definition of the fields that have to be extracted and their conversion to intermediate files so-called variable tables (Vtables) are used (Wang et al., 2010).

`metgrid` interpolates the meteorological output of `ungrib` to the grids that are established by `geogrid`. This tool sets the boundary conditions as well as the initial conditions for all domains. These data are made available in so-called `metem` files, which are produced for each domain. However, the initial and the boundary conditions are cast in vertical pressure coordinates, which can not be processed by WRF since it uses η -levels as discussed above (Fig. 2.2). Hence, a tool called `real.exe` is employed to interpolate the data from pressure levels to η -levels. This yields the `wrfinput` and `wrfbody` files that can be used by `wrf.exe` to perform the RCM run.

Nudging

Nudging is an option which is often used in regional models. It provides the possibility to continually force the model to follow the large scale circulation given by either reanalysis data, output from a comprehensive GCM, or observations. In WRF, three options of nudging are implemented: no nudging at all, analysis nudging, and observational nudging (Wang et al., 2010). Thereby, analysis nudging forces the model simulation grid point by grid point towards a series of analysis, whereas observational nudging locally forces the simulation towards observational data. The herein chosen settings for nudging will be presented in the section on the experimental design.

2.4 Experimental design

One goal of this study is to reproduce the meteorological situation that was responsible for the flooding in Switzerland in August, 2005. The above discussed input data for the time span of this event provide the boundary and initial conditions to design the WRF ctrl simulation.

ctrl simulation

The ctrl simulation starts on August 20 (00 UTC) and ends on August 24, 2005 (00 UTC). Thus, the simulated time span covers four days. The simulation consists of 4 nested domains (D1, D2, D3, D4) (Fig. 2.4). Each domain has 36 η -levels in the vertical. The height above sea level of every vertical η -level for 15°E and 43.5°N

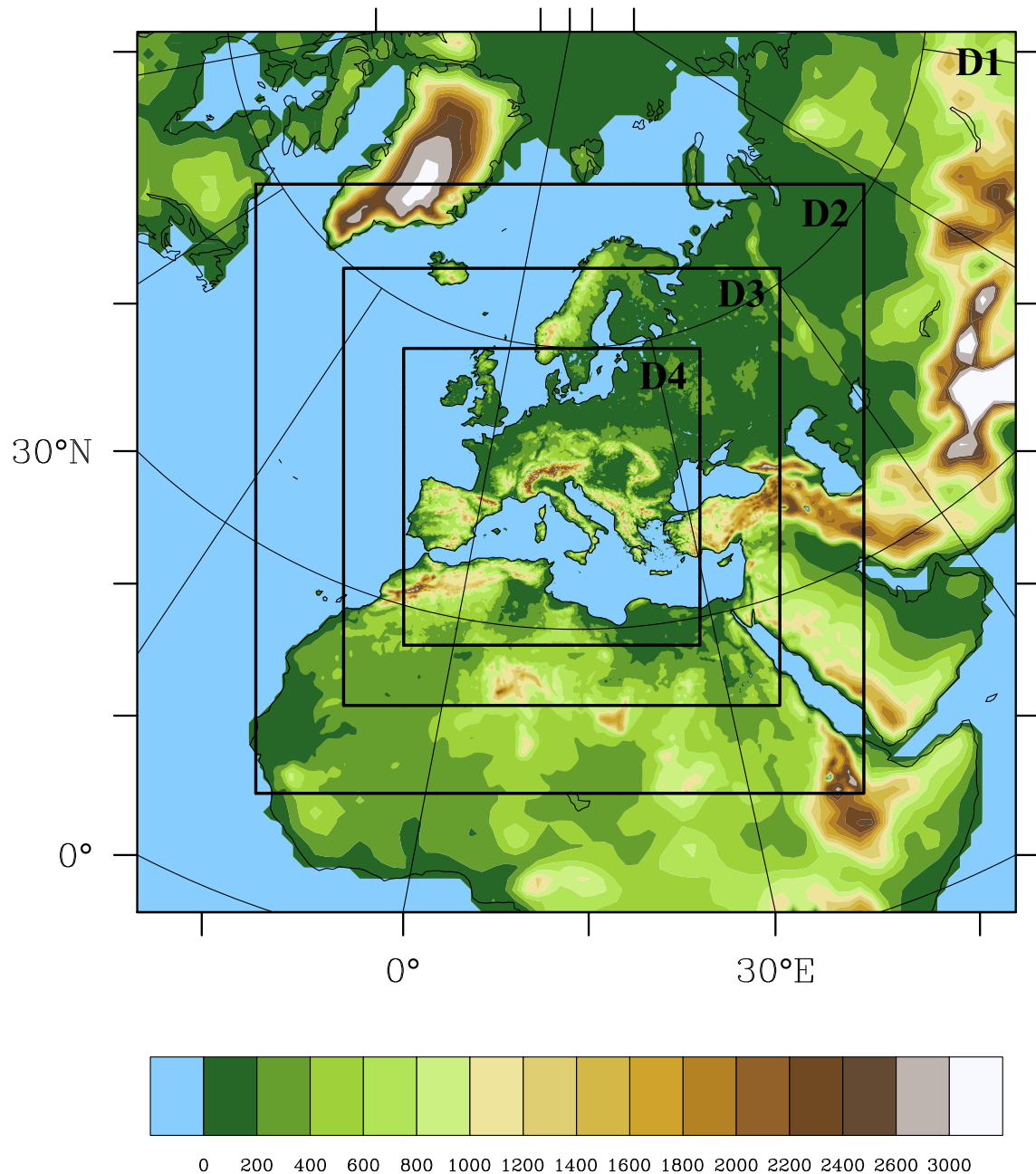


Figure 2.4: Four nested domains (D1, D2, D3, D4) for the model simulations with WRF. To illustrate the horizontal resolution the orography is shown.

(over the Adriatic Sea) is shown in Fig. 2.5, whereas the corresponding pressure values at the same coordinate are indicated by Fig. 2.6. Since stratospheric processes can also be important for the genesis and propagation of mid-latitude cyclones, the top layer of the simulations is at 20 hPa. The spatial resolution and the time steps of the different domains are listed in Table 2.1.

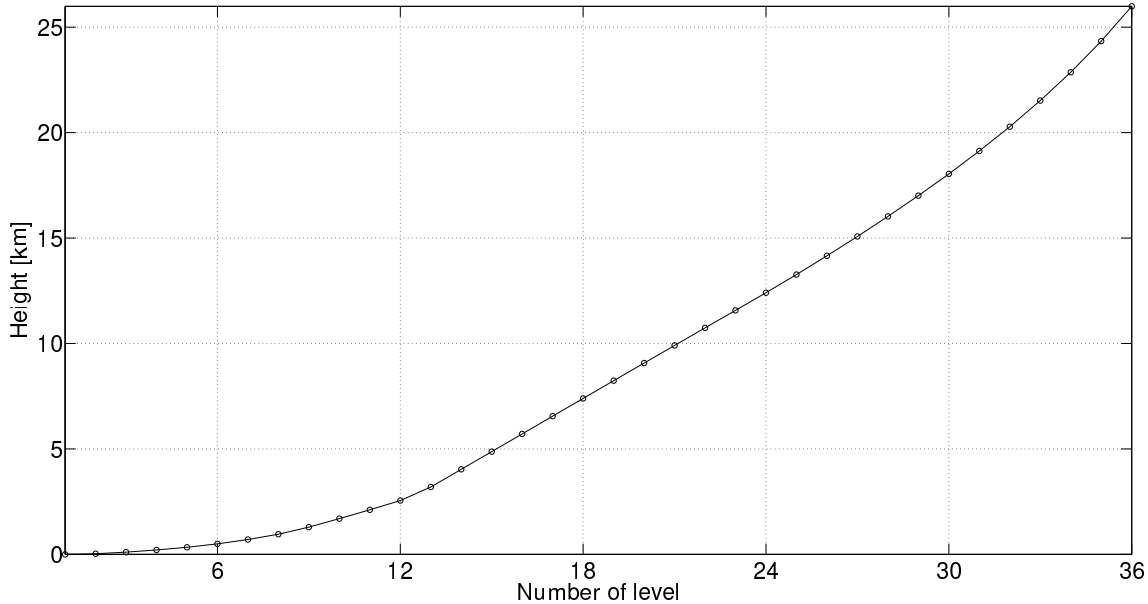


Figure 2.5: Height of vertical η -levels over the Adriatic Sea at 15°E and 43.5°N.

The center point of the parent domain is set at 46.6° N and 14° E. This allows to properly cover the geographical area of interest. The model uses a Lambert projection, which minimizes distortions at mid-latitudes.

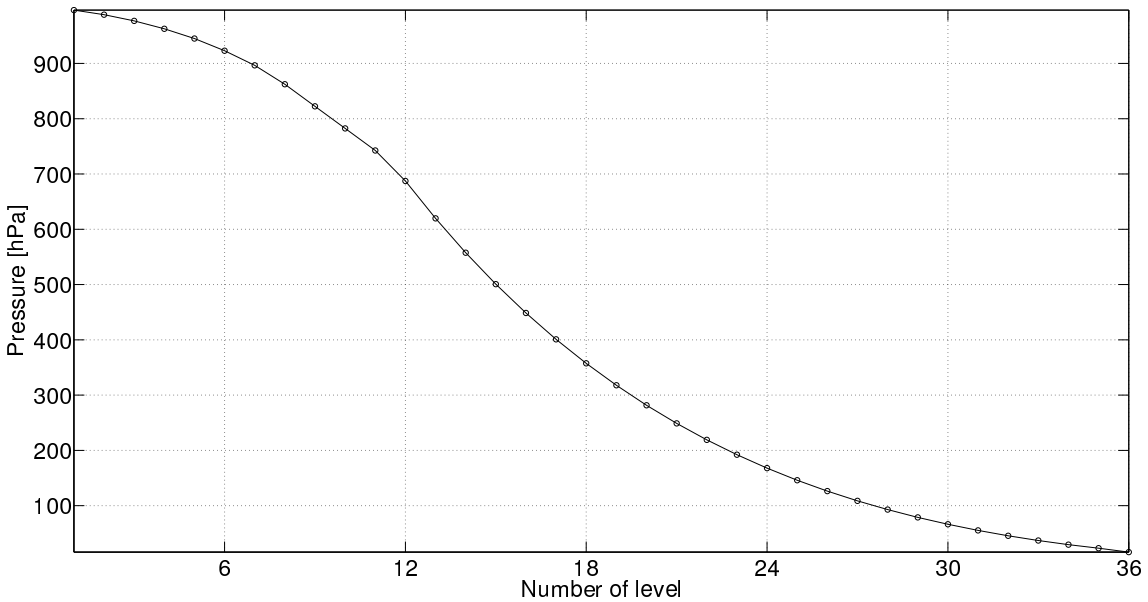


Figure 2.6: Pressure of vertical η -levels over the Adriatic Sea at 15°E and 43.5°N.

Table 2.1: Spatial resolutions and time steps of the four domains that are used for the simulations with WRF.

Domain	Spatial Res. [km]	Time step [sec]
1	108	180
2	36	60
3	12	20
4	4	6.66

Sensitivity experiments

For the sensitivity experiments the setting of the ctrl simulation is used, except for the SST in the Mediterranean (without the Black Sea). The colored region in Fig. 2.7 corresponds to the area where the SST is changed. The changes are uniform and always relative to the SST distribution as it is present in the ctrl simulation. Changing the SST by -5 K to +5 K in 1 K intervals, a total of 10 sensitivity experiments are performed and later on analyzed. Figure 2.7 shows the SST distribution in the 3rd domain of the ctrl simulation, which covers the whole Mediterranean Sea.

The use of nudging to design the WRF ctrl simulation would probably produce an even more accurate outcome for the ctrl simulation with respect to reanalysis data. However, since one of our aims is to analyze the implications of increased SSTs in the Mediterranean to the trajectory of the cyclone, it is important that the simulations

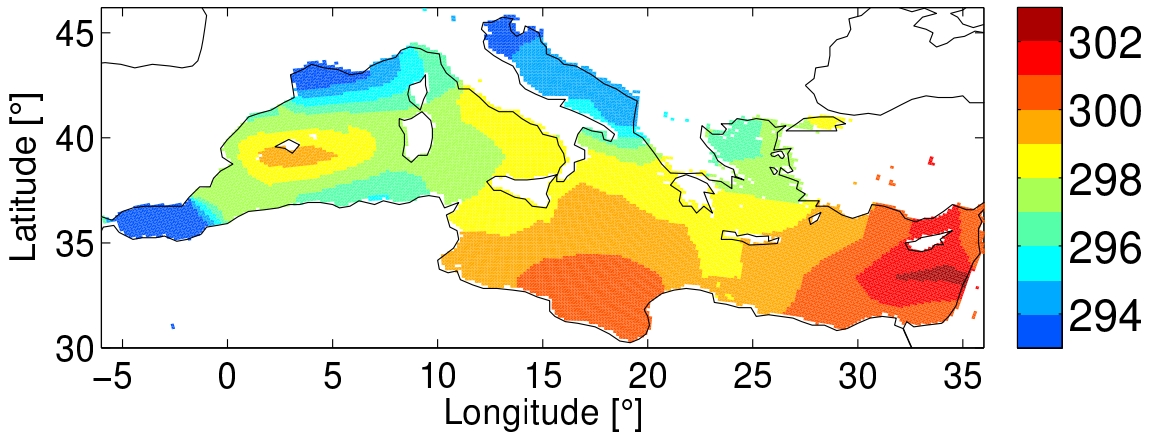


Figure 2.7: SST distribution in Kelvin for the domain D3 of the ctrl simulation on August 20, 2005 (00 UTC).

run freely. With the use of nudging in the ctrl simulation it would not be discernable anymore whether the deviations of the trajectory or the intensity in the sensitivity experiments is triggered by the removal of the nudging process or the increase of the SSTs in the Mediterranean. Hence, in this study the usage of nudging is not appropriate.

Chapter 3

Methods

In this chapter, the methods employed in this study are presented in detail. Firstly, the methods which are used to analyze precipitation in the alpine area are introduced. Then, the cyclone detection and tracking techniques are presented.

3.1 Precipitation analysis

According to chapter 1.1, substantial floodings on the northern side of the Alps occurred in the last twenty years: Some were associated with Vb-type cyclones. Hence, one scope of this study is to investigate the role of Vb-type cyclones in terms of their precipitation contribution in a climatological perspective. Thus, the connection between the occurrence of Vb-type cyclones in the past and anomalously high precipitation rates on the northern side of the Alps is analyzed in ERA-interim.

Furthermore, precipitation is analyzed in the WRF output. This is done to investigate the sensitivity of the precipitation in a target area in northern Switzerland to changes of SSTs in the Mediterranean. Furthermore, changes in atmospheric states and physical processes that can be relevant for precipitation are analyzed.

3.1.1 Precipitation impact of Vb-type cyclones

Herein, a point of interest is the climatological impact of Vb-type cyclones on precipitation located at the northern side of the Alps, namely in southern Germany, Austria and Switzerland. To statistically analyze this precipitation impact, a target area that covers this region is defined. This target area covers the longitudes 6°E to 16.5°E and the latitudes 46°N to 49°N (Fig. 3.1). The size of this target area has to be large enough so that it is representative for Vb related precipitation, but it should not be too large so that it is affected by other low pressure systems that might pass simultaneously more in the North. Hence, the chosen region represents precipitation in Switzerland, southern Germany, and Austria. Hereinafter, this first target area for precipitation is called: European rain area.

The climatological yearly cycle of precipitation in the European rain area is esti-

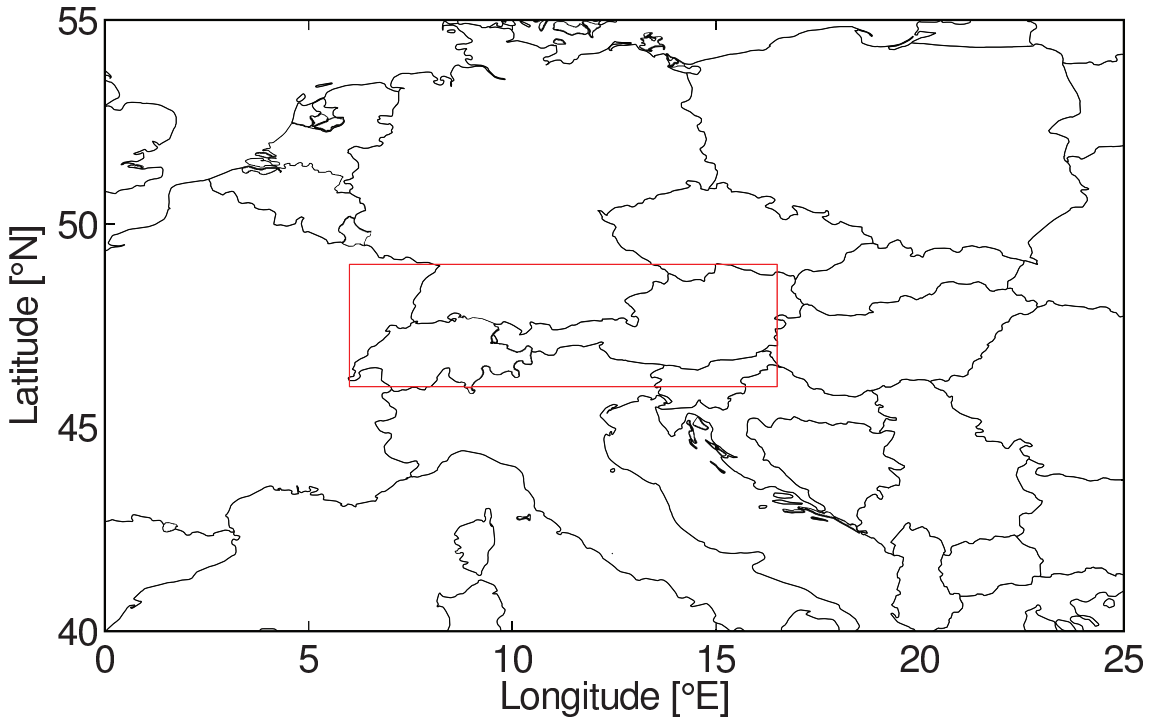


Figure 3.1: Target area used for the analysis of precipitation caused by Vb-type cyclones in Switzerland, southern Germany, and Austria.

mated by calculating the spatial mean values of daily precipitation in Eq. 3.1. This is calculated for every day d in the annual cycle as:

$$\bar{P}_d = \frac{1}{n_{lat}} \sum_{i_{lat}}^{n_{lat}} \frac{1}{n_{lon}} \sum_{i_{lon}}^{n_{lon}} P_d(i_{lat}, i_{lon}, d), \quad (3.1)$$

where \bar{P}_d is the spatial mean of daily precipitation in the European rain area and day d . i_{lat} and i_{lon} are the longitudinal and latitudinal grid points i , respectively, and n_{lat} and n_{lon} are the amount of longitudinal and latitudinal grid points in the European rain area. It has to be noted that a model grid box that is located more northwards represents a smaller area than a grid box that is relatively located more southwards. An area weighting is however not applied, since these area differences are negligible.

Next, the daily mean values are used to compute the monthly mean values in mm/-day. This yields one spatial mean value for every month during the whole analyzed time span:

$$\bar{P}_m = \frac{1}{n_{d_m}} \sum_{k_{d_m}=1}^{n_{d_m}} \bar{P}_d(k_{d_m}), \quad (3.2)$$

where \bar{P}_m is the precipitation mean value of a particular month m in mm/day. d_m is a particular day within the month m , and n_{d_m} is the amount of days within this month m .

Finally, all the monthly mean values of corresponding months (e.g., all the Januaries in the analyzed time span) are used to compute the climatological monthly mean (Eq. 3.3). This yields a yearly cycle that consists of 12 climatological mean values, one for each month of the year. Thereby, each value is defined to represent the middle day of a particular month:

$$\bar{P}_{cm} = \frac{1}{n_{mp}} \sum_{k_{mp}=1}^{n_{mp}} \bar{P}_m(k_{mp}), \quad (3.3)$$

where \bar{P}_{cm} is the climatological mean value of month m in mm/day. n_{mp} is the amount of years.

Subsequently, the difference between every daily precipitation value in the European rain area and the climatological yearly cycle is calculated. Hence, a linear interpolation between two values of the yearly cycle is applied to obtain the climatological precipitation value for a day that lies in between of two middle days of a month (Eq. 3.4):

$$P_{ad}(t) = P_d(t) - (\bar{P}_{cm}(t) + \left(\frac{\bar{P}_{cm}(t+1) - \bar{P}_{cm}(t)}{n_d} \right) (d(t) - d_{middle}(t))), \quad (3.4)$$

where $P_{ad}(t)$ is the daily rain anomaly corresponding to date t , $P_d(t)$ is the daily precipitation value corresponding to date t , $P_{cm}(t)$ is the monthly climatological mean (taken from the yearly cycle) corresponding to the month of date t , $d(t)$ is the day that corresponds to the day of date t , and d_{middle} is the middle day corresponding to the month of date t , while n_d is the amount of days in a particular month.

Further on, the amount of Vb-type cyclones that contribute to extreme precipitation in the European rain area is analyzed. This is done by checking whether the day of maximum rain of each Vb-type cyclone exceeds the 95th percentile of all the precipitation anomalies.

Besides, a bootstrapping test between all the anomalies of the entire time span and the anomalies that belong to a Vb-type cyclone is performed to check whether there is a significant difference between the mean values of the two samples. For the bootstrapping, the series of all the rain anomalies are randomized. This yields a new distribution $X_{1(shuffled)}$. Then, the mean value, which consists of the first n

rain anomalies from $X_{1(\text{shuffled})}$ is computed, where n is the size of the sample that consists of the rain anomalies that are related to Vb-type cyclones. This procedure is repeated 5000 times, which leads to a new distribution X_2 that is comprised of 5000 new mean values. Then, it is tested for a significance level of 5% whether the sample mean value of the anomalies that belong to Vb-type cyclones exceeds the 97.5th percentile of X_2 .

3.1.2 Precipitation analysis of WRF output

An important part of our analysis in this study concerns the sensitivity of precipitation to SSTs in the Mediterranean, analyzed by performing sensitivity experiments with WRF. Since the analysis with WRF is performed in the case of the alpine flooding in 2005, a second target area for Switzerland is established (Fig. 3.2). This second target area covers the longitudes 7.15°E to 9.3°E and latitudes 46.5°N to 47.25°N and includes only a part of Switzerland located to the north of the Alps. The mean value of the simulated precipitation by WRF in this second target area is then compared with the observed precipitation mean value in the same area and for the same time span provided by MeteoSwiss. Henceforth, this second target area for precipitation is called: Swiss rain area.

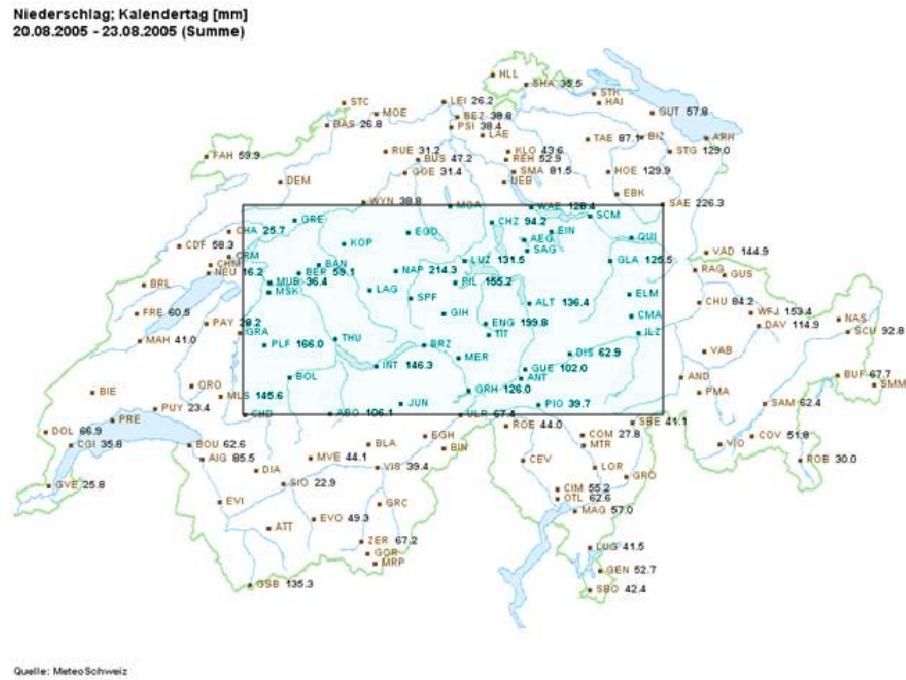


Figure 3.2: Target area for precipitation in Switzerland. Figure from MeteoSwiss.

The total amount of precipitation computed by WRF is considered for the entire simulated time span, hence, from August 20 to August 24, 2005. This is necessary because the model might not be able to resolve the time development of precipitation

in a completely accurate way. However, this is not a problem since herein only an accurate reproduction of the total amount of accumulated rain in the target area is of interest.

To analyze the sensitivity of precipitation in the Swiss rain area to changes of SST in the Mediterranean, the spatial mean values of precipitation in the Swiss rain area, as well as the maximum precipitation values in the Swiss rain area are considered. Besides, the time series of precipitation in the Swiss rain area is shown for each sensitivity experiment.

Furthermore, relative humidity, vertical surface moisture fluxes, and distributions of upper level PV on the 330 K isentropic surface of the ctrl simulation and the sensitivity experiments are analyzed. This is done to gain insight into the changes in the underlying processes and atmospheric states that lead to precipitation.

3.2 Cyclone detection and tracking

To obtain a climatology of Vb-type cyclones based on reanalysis data that can be compared with all the cyclones that pass over a defined area of Europe, the associated cyclones have to be identified and tracked. This is done in two steps: Firstly, a detection and tracking algorithm is used to identify all the cyclones that pass over an area of Europe. In a second step, all the Vb-type cyclones have to be identified within the European cyclones. To do so, a filter algorithm is applied to the cyclone tracks. A detailed description of the applied tracking and filter algorithms for the Vb climatology is presented in this chapter.

Furthermore, the track and intensity of the Vb-type cyclone simulated with WRF is identified. This is important in order to analyze whether the simulated Vb-type cyclone in the ctrl simulation follows the trajectory and intensity as it is prescribed by reanalysis data. Furthermore, it is a point of interest to see whether the path and strength of the cyclone in the sensitivity experiments deviate from the path and strength of the ctrl simulation. Hence, a tracking algorithm for the WRF output was developed, which is presented in the second part of this section.

According to Hofstaetter and Chimani (2012) it is not recommendable to track cyclones at surface levels that pass the complex topography of mountain regions such as the Alps. A major reason for this is that cyclones in summer often have a weak or fairly disturbed pressure signal on the surface. This leads to inhomogeneities that might appear in the track of these cyclones. Therefore, the detection and tracking of Vb-type cyclones for the Vb climatology as well as for the WRF model output is applied to the gph at 700 hPa ($z700$).

3.2.1 Cyclone tracking for the Vb climatology

The cyclone tracking for the Vb climatology is carried out with the detection and tracking technique of Blender et al. (1997). This cyclone identification algorithm consists of four steps: (1) A cyclone is identified as a local minimum of gph. A local minimum is defined as a minimum within eight neighboring grid points. (2) The cyclone intensity measured by the mean gradient of gph in an area with a radius of 1000 km has to exceed a threshold. (3) At least once within the life time of a cyclone, the aforementioned intensity has to exceed a second threshold value (Blender et al., 1997). (4) The last criterion concerns the minimum life time of a cyclone, which needs to be set. The trajectories of the cyclones are then determined using a nearest-neighbor search within a radius of 1000 km and within the minimum life time. The nearest-neighbor search is done without assuming a preferred propagation, direction or speed of the cyclone (Blender et al., 1997).

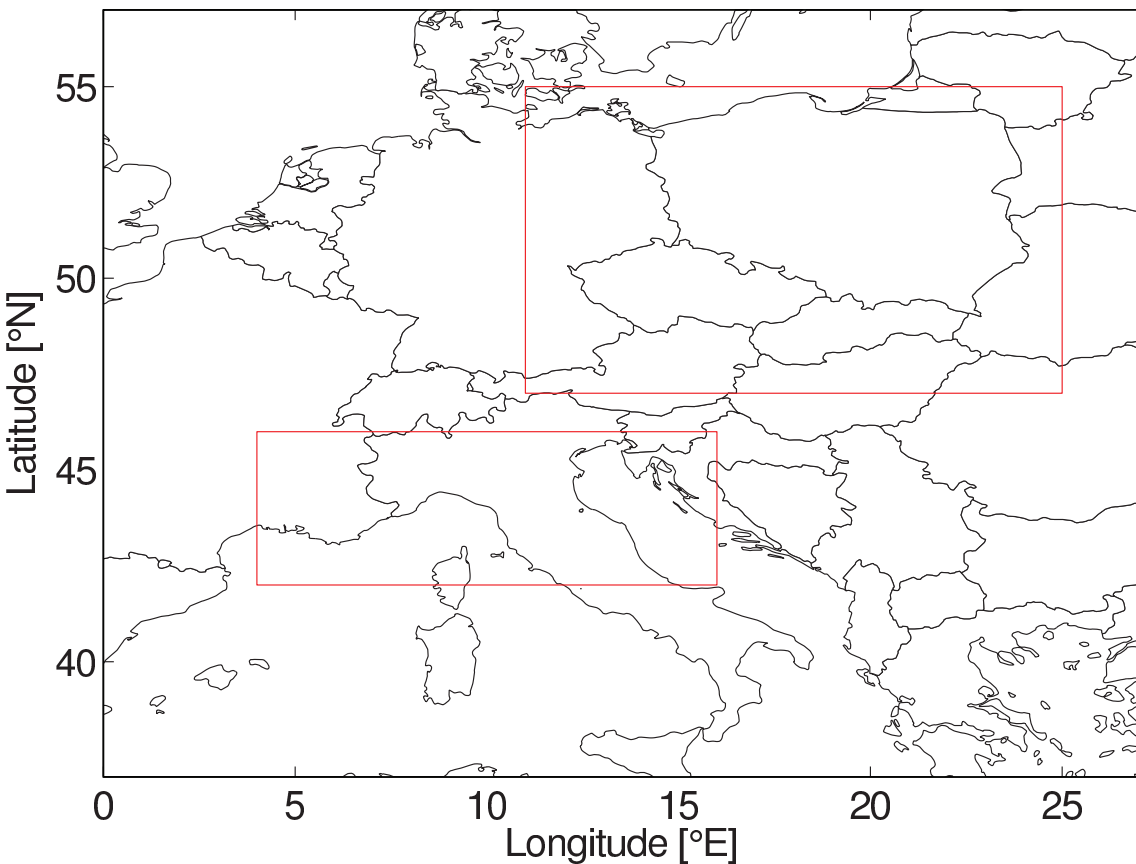


Figure 3.3: Tracking boxes used for the identification of Vb-type cyclones.

It is necessary that the thresholds and criteria are chosen in a way that allows to identify as much Vb-type cyclones as possible. This can be done by tracking single cyclones (e.g., the Vb-type cyclone that caused the alpine flooding in 2005 in Switzerland). The output can then be compared with reanalysis data to make

sure that the tracking algorithm works properly. In addition, other cyclones can be considered to check whether the algorithm detects and tracks them accurately. Herein, a minimum gradient of gph of 35 gpm/1000 km is employed. Moreover, at least once during the life time of the cyclone, the gradient of gph has to exceed a threshold of 100 gpm/1000 km; the minimum life time is 24 h. Furthermore, the area where cyclones are tracked has to be defined. This area should be large enough to ensure that all the cyclones of interest are identified. Therefore, the tracking tool is applied to a box that covers the latitudes 20°N to 85°N and the longitudes 10°W to 40°E. Henceforth, this area is called: cyclone tracking box.

Since in this study the ratio of Vb-type cyclones to all the cyclones in Europe is of interest, a further target area is established to filter out all the cyclones that passed over Europe. This area is called European tracking box, and extends from 0° to 35°E and 35°N to 60°N. To do the filtering an automatized algorithm was implemented. Firstly, this algorithm is applied to the European tracking box, and secondly to filter out all the Vb-type cyclones. To filter out the Vb-type cyclones, two further boxes are defined, where a Vb-type cyclone is expected to pass (Fig. 3.3). The first box extends from 4°E to 16°E and 42°N to 46°N. The second box covers the longitudes from 11°E to 25°E and the latitudes from 47°N to 55°N. A cyclone needs to pass through the first box, which hereinafter is called Vb-box 1. If this is the case, the same cyclone needs to be detected in the second box, which hereinafter is called Vb-box 2.

3.2.2 Cyclone tracking for WRF output

The detection algorithm of Blender et al. (1997), which was used for the Vb climatology, requires global input data. However, WRF is a regional model and, hence, produces regional output. Therefore, another algorithm was written to detect and track cyclones in the WRF output. This algorithm consists of four steps, which are presented now:

- (1) For a meaningful tracking it is important to remove spatial high frequency noise. Although the used gph-field of $z700$ is considerably distant from the surface, it is still possible that artifacts, produced by the complex topography of the alpine area, disturb the tracking procedure. Therefore, a bilinear interpolation from the resolution of domain D4 of the WRF output to the resolution of the ERA-interim reanalysis data (1.5°) is performed. This lowers the resolution of the WRF output leading to a smoothing of the used gph field. Subsequently, the obtained field is interpolated back to the grid of domain D4.
- (2) Only points that are located below 200 meters a.s.l. are considered. This is a further measure to make sure that the Alps are not disturbing the pressure signal.
- (3) An intensity measure for Vb-type cyclones is implemented. For every grid point i , the first derivatives in east, west, north, and south directions are computed (Eq.

3.5 and 3.6). The derivatives are computed between the $z700$ value at grid point i and the $z700$ mean consisting of Δi grid points in a particular direction. Only the grid points that show positive values for all four gradients are taken into account. This leads to the identification of local minima.

$$\frac{(\bar{\Phi}_{i+\Delta i_x} - \Phi_i)}{\Delta i_x} > 0 \text{ and } \frac{(\bar{\Phi}_{i-\Delta i_x} - \Phi_i)}{\Delta i_x} > 0 \quad (3.5)$$

$$\frac{(\bar{\Phi}_{i+\Delta i_y} - \Phi_i)}{\Delta i_y} > 0 \text{ and } \frac{(\bar{\Phi}_{i-\Delta i_y} - \Phi_i)}{\Delta i_y} > 0 \quad (3.6)$$

where Φ_i stands for $z700$ at grid point i . Δi_x corresponds to 10 grid points in the x -direction (west to east) and Δi_y corresponds to 10 grid points in the y -direction (south to north). $\bar{\Phi}$ represents the mean of $z700$, and e.g. $\bar{\Phi}_{i+\Delta i_x}$ represents the mean of $z700$ that consists of the first ten grid points that are located east of grid point i .

(4) in every time step, grid points are canceled out if they do not fulfill the aforementioned measures. Now, from the remaining grid points, and for every time step, the grid point that exhibits the lowest value in $z700$ is designated to be the center point of the cyclone.

Chapter 4

Climatology of Vb-type cyclones and their impacts on precipitation

In this chapter the climatology of Vb-type cyclones is described in terms of their trajectory, intensity, frequency, and length. Then, the impacts on precipitation of Vb-type cyclones are presented.

4.1 Vb climatology

To give a first impression about the ability to detect and track cyclones with the method of Blender et al. (1997) in ERA-interim, all Vb-type cyclone trajectories are shown in Fig. 4.1. The Vb-type cyclone trajectory starts over the Gulf of Genoa, and goes then over Austria towards Poland or the Ukraine (Fig. 1.1). Shown are the trajectories of all cyclones from March 1979 - February 2009, that assume a Vb-movement for at least a part of their life time. As expected, cyclones are concentrated between the two blue boxes, which are used for the identification of Vb-type cyclones (Fig. 3.3). The highest density of the identified cyclone tracks is located over the Gulf of Genoa, and extends north-east towards Austria. The spatial variability increases with increasing distance to this area. It is rare that Vb related cyclones start over Africa and then propagate towards Europe, whereas more Vb related cyclones form over the western Mediterranean or France (Fig. 4.1).

Fig. 4.1 shows also the mean Vb-type trajectory for the period 1979-2009 in green. To obtain this trajectory, the first time step of each cyclone that is located in the Vb-box 1 is taken to calculate the mean longitude and latitude. This is repeated for every further time step, until the end of every cyclone. The mean trajectory in green resembles the Vb path visible in Fig. 1.1.

To characterize the life cycle of Vb-type cyclones, their intensity is also investigated. To do so, grid points that are below the 5th percentile of $z700$ are indicated with black crosses, and grid points that are above the 95th percentile of the gradient of $z700$ are represented by purple crosses (Fig. 4.1). Furthermore, the green dots indicate grid points where both of the aforementioned percentiles are exceeded and

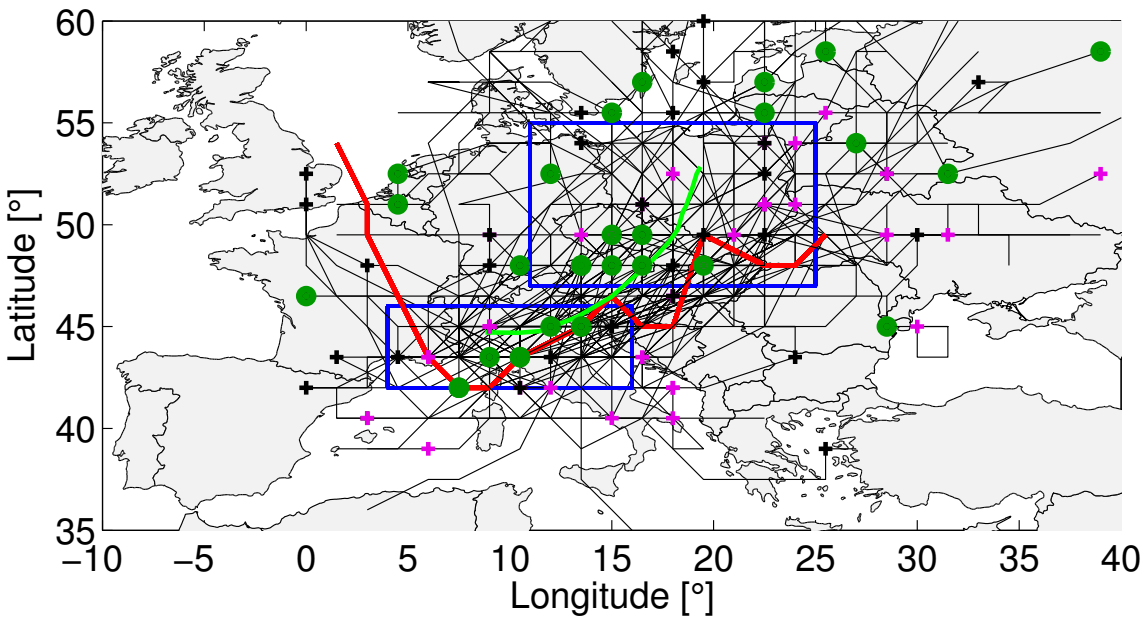


Figure 4.1: Vb tracks detected in ERA-interim from 1979 to 2009. Blue rectangles show the Vb-boxes 1 and 2, which are used to identify Vb-type cyclones. The mean Vb trajectory is shown in green and the Vb-type cyclone that is used for the sensitivity experiments with WRF is emphasized in red. The black crosses indicate grid points where $z700$ deceeds the 5th percentile of a particular cyclone. The purple crosses indicate grid points where the gradient of $z700$ is above the 95th percentile of a particular cyclone and the green dots indicate grid points where both of the aforementioned percentiles are exceeded and deceeded, respectively.

deceeded, respectively. There is a remarkable cluster of green dots along the Vb mean trajectory. This suggests that most of the identified trajectories are most intensive in the middle part of their trajecories.

This is also confirmed by Fig. 4.2a, which shows the life cycles of the differences between minimum $z700$ of a particular cyclone and the mean $z700$ of this particular cyclone. Furthermore, the same is shown for the intensity measured by the mean gradient around a minimum (Fig. 4.2b). Every blue line in Fig. 4.2 corresponds to a Vb-type cyclone identified in Fig. 4.1. The overall range of $z700$ is between 2550 and 3250 gpm, whereas the overall range of the gradient of $z700$ is between 30 and 275 gpm/1000 km. To obtain Fig. 4.2, all the cyclones are interpolated to a constant amount of time steps that exceeds the amount of time steps of the longest identified Vb-type cyclone. This is done to show the intensity in terms of the relative life times. Moreover, the climatological mean evolution of $z700$ is shown in red. This curve is obtained by calculating the mean $z700$ value of corresponding time steps. The temporal evolution of the mean in Fig. 4.2a (red line) shows a clear deepening, ranging from 25 gpm at the beginning to about 0 gpm in the middle, back to 25 gpm at the end of the life cycle. The same is confirmed by Fig. 4.2b, where the temporal evolution ranges from -23 gpm/1000 km at the beginning to 7 gpm/1000 km in the middle part, back to 25 gpm/1000 km at the end of the life cycle. Hence, corresponding with the green dots in Fig. 4.1, the first half of the mean Vb life cycle is dominated by an intensification, whereas the second half is dominated by a loss of intensity.

Now it is interesting to know how many low pressure systems are identified from 1979 to 2009. In this regard, a total of 532 cyclones are found in the european tracking box. Out of these, 89 Vb-type cyclones are filtered out using Vb-box 1 and Vb-box 2 (Fig. 3.3). Furthermore, there are 29 Vb-type cyclones in spring, 20 in summer, 23 in autumn, and 17 in winter. Hence, there is a majority of Vb-type cyclones occurring in spring, with a secondary maximum in autumn. In winter the occurrence of Vb-type cyclones is reduced.

The mean occurrence of Vb-type cyclones is 2.97 cyclones per year, or 7.18 days per year. The occurrence of Vb-type cyclones per year is very variable ranging from 0 to 7 with a standard deviation of 1.83 Vb-type types per year (Fig. 4.3a). The occurrence of Vb-type cyclones per year shows no clear trend between 1979 and 2009. Corresponding to Fig. 4.3a, Fig. 4.3b shows the relative distribution of Vb-type cyclones of the entire period. Fig. 4.4a shows the number of 6-hourly time steps per year that are related to Vb-type cyclones. In this respect, the time steps are counted as soon as a cyclone enters Vb-box 1. The time series of the 6-hourly time steps per year that are related to Vb-type cyclones shows no temporal trend (Fig. 4.4a). Again, the corresponding relative distribution of these 6-hourly intervals of the entire period is presented (Fig. 4.4b).

Besides the mean occurence also the mean length of a Vb-type cyclone is of interest.

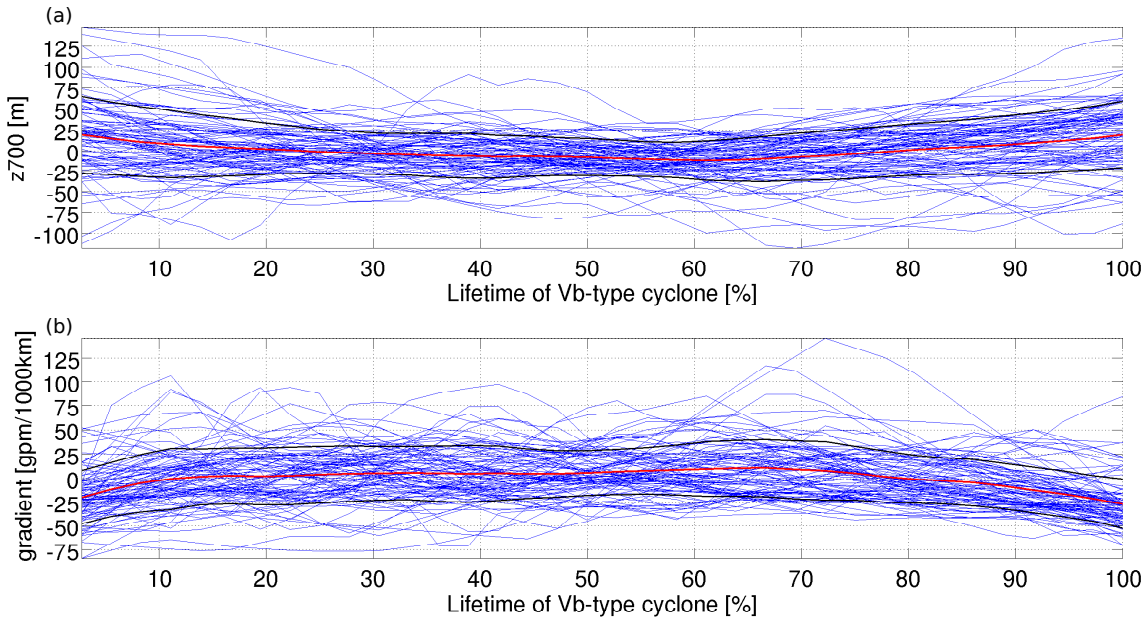


Figure 4.2: a) Life cycles of the differences between minimum $z700$ in a time step of a particular cyclone and the mean $z700$ of this particular cyclone for all the Vb-type cyclones in Fig. 4.1 (blue lines). The red line represents the mean of the blue lines. The black lines show the standard deviation around the mean. The time axis shows the relative life time of the Vb-type cyclones. b) Same as a) but for $z700$ gradient.

In this respect, Vb-type cyclones from 1979-2009 varied in length from 24 hours to 186 hours (Fig. 4.5). The mean length of a Vb-type cyclone is 58 hours, with a standard deviation of 31.2 hours. This contrasts with the mean length of all the cyclones that passed over central Europe, which is 84 hours. More than 80% of the Vb-type cyclones from 1979-2009 lasted between 24 and 72 hours.

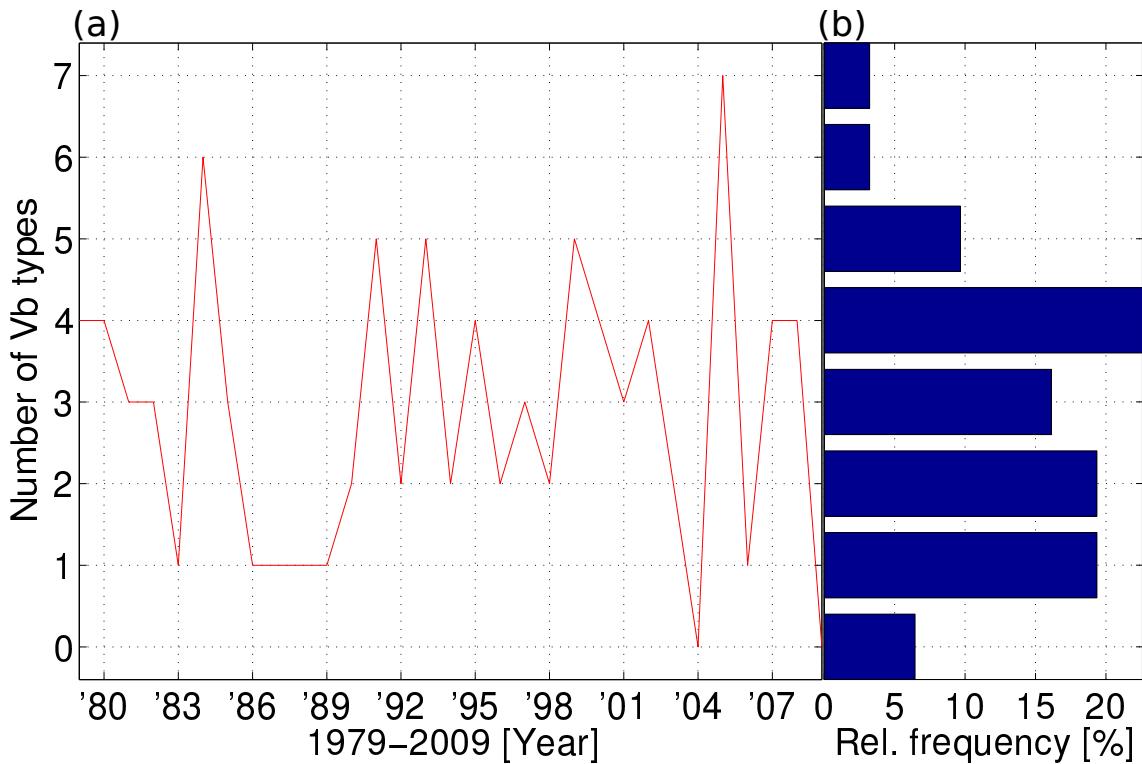


Figure 4.3: a) Number of Vb-type cyclones per year in the period 1979-2009; b) corresponding relative distribution of Vb-type cyclones of the entire period.

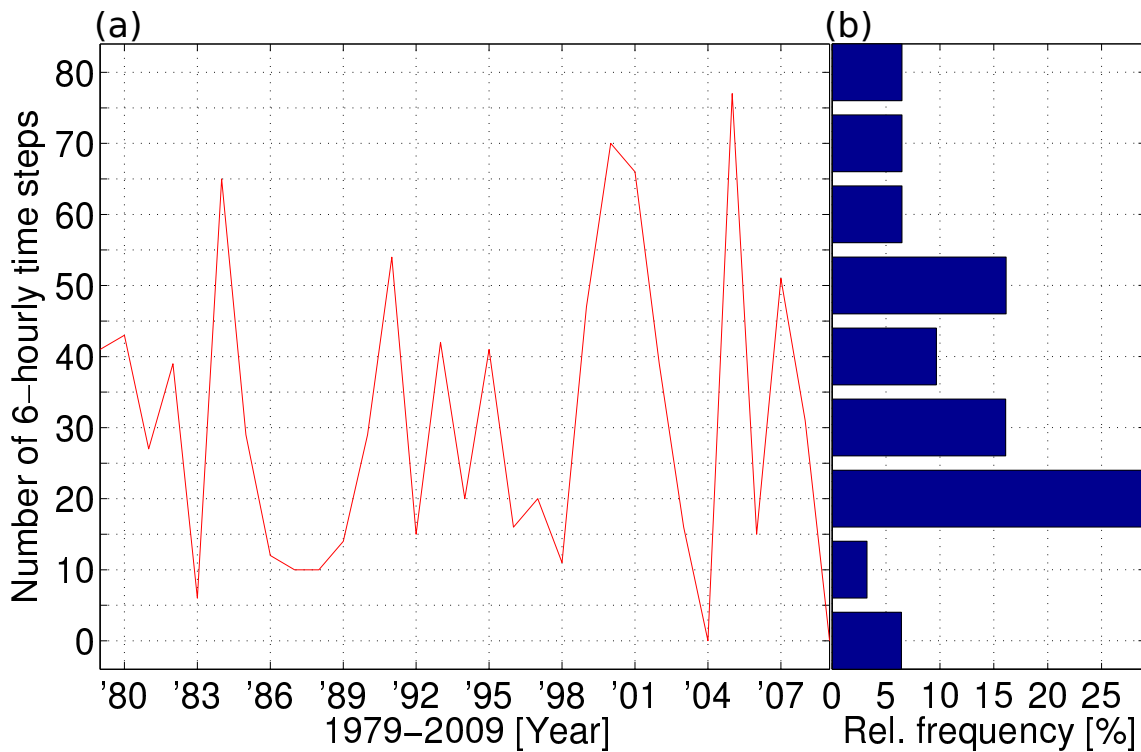


Figure 4.4: a) Number of Vb related 6-hourly intervals per year in the period 1979–2009. b) corresponding relative distribution of these 6-hourly intervals of the entire period.

4.2 Impact on precipitation

As discussed in Section 1.1, Vb-type cyclones are important phenomena in terms of extreme precipitation on the northern side of the Alps. In this respect, extreme precipitation is defined to be located above the 99th percentile of a precipitation distribution. This section investigates the role of Vb-type cyclones with respect to precipitation in Switzerland, southern Germany, and Austria. To do so, a climatology of precipitation for the European rain area is presented. The data for the precipitation climatology is provided by ERA-interim with a spatial resolution of 1° .

The climatological mean winter precipitation in the European rain area is approximately 3 mm/day (Fig. 4.6). These are the minimum values throughout the year. Then, mean precipitation increases to its maximum value of about 6 mm/day in summer. This annual cycle of precipitation is used to calculate the daily rain anomalies (annual cycle removal). For the exact process to produce these rain anomalies, see the subsection 3.1.1.

Fig. 4.7 shows the time series of daily rain anomalies averaged over the European rain area in Fig. 3.1 between 1979 and 2009 found in ERA-interim. The analyzed period consists of 10958 days. For this time period, positive anomalies in precip-

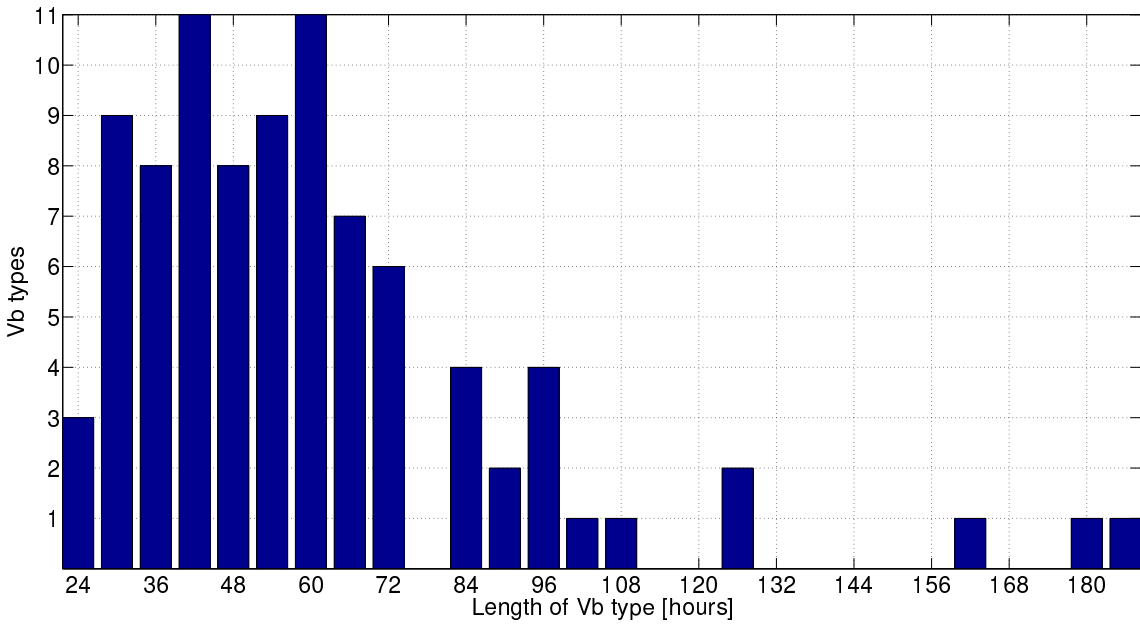


Figure 4.5: Histogram showing the length of all the Vb-type cyclones between 1979 and 2009 in hours starting at the first time step, where a cyclone enters the first Vb-box 1.

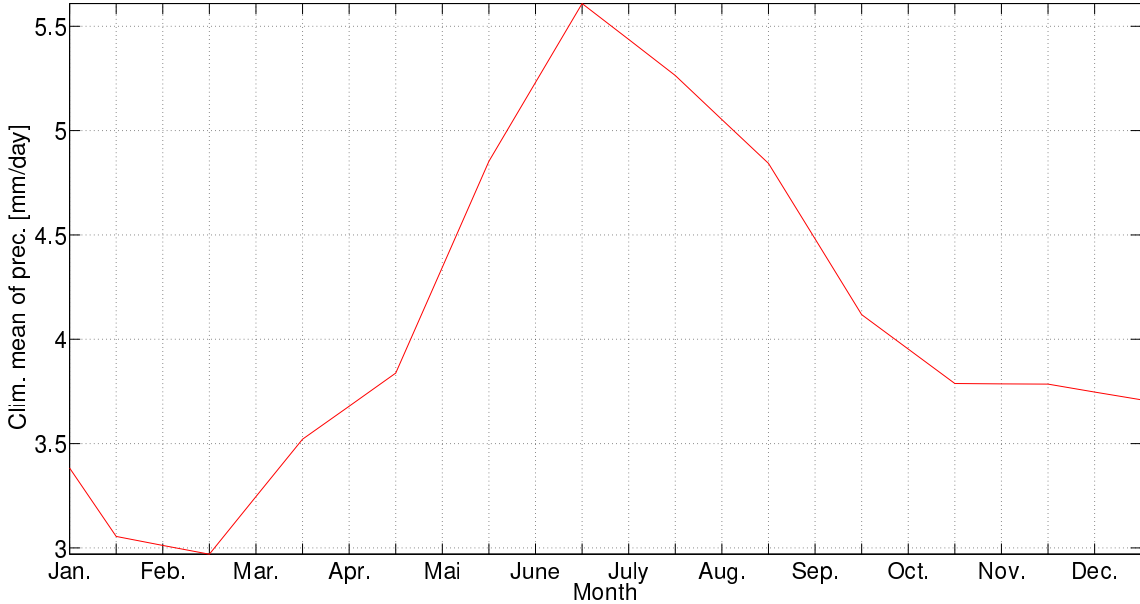


Figure 4.6: Annual cycle of precipitation for the European rain area (Fig. 3.1). The mean values of daily precipitation for each month are shown in mm/day.

itation are found on 4112 days. In this respect, the 218 rain anomalies that are related to Vb-type cyclones are comparatively little in amount, which indicates that Vb-type cyclones are rare as a reason for precipitation in Switzerland, southern

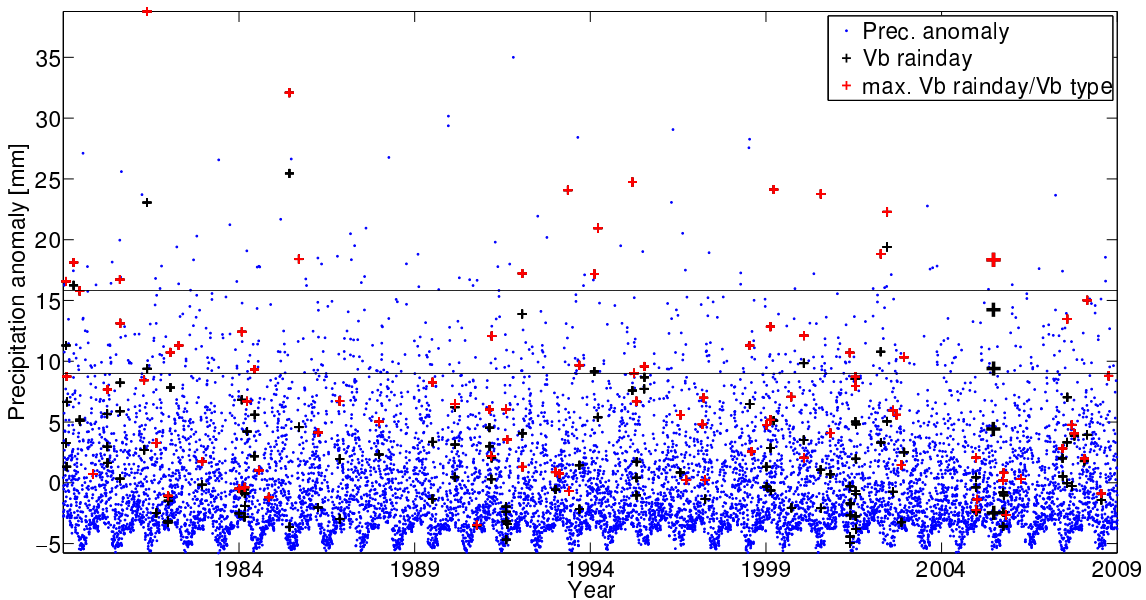


Figure 4.7: Time series of rain anomalies from 1979-2009 in the ERA-interim data set in the European rain area averaged over Switzerland, southern Germany, and Austria (Fig. 3.1). The blue dots indicate precipitation anomalies. Black crosses highlight all the rain anomalies that occur during Vb situations. The maximum rain days per Vb-type cyclone are colored in red. The horizontal black lines indicates the 95th and 99th percentiles. Furthermore, the Vb related rain days that belong to the Vb-type cyclone which occurred in August, 2005 are shown with bold crosses.

Germany, and Austria. However, from 89 Vb-type cyclones found between 1979 and 2009, 31 cyclones contributed to precipitation amounts that are above the 95th percentile in the European rain area. This corresponds to 34,8% of all Vb-type cyclones. Furthermore, 16 out of 89 Vb-type cyclones even contribute to precipitation values that are above the 99th percentile. Regarding individual days, 43 out of 218 Vb rain days exceed the 95th percentile, whereas 20 Vb rain days exceed the 99th percentile. This corresponds to 18% of extreme precipitation in the European rain area. The Vb-type cyclone that occurred in August, 2005 and which is analyzed using the regional model WRF (Chapter 5) is shown with bold crosses. The wiggles at the bottom of the panel indicate the climatological yearly cycle of precipitation. In this sense, the minima of the wiggles correspond to summer, and the maxima correspond to winter.

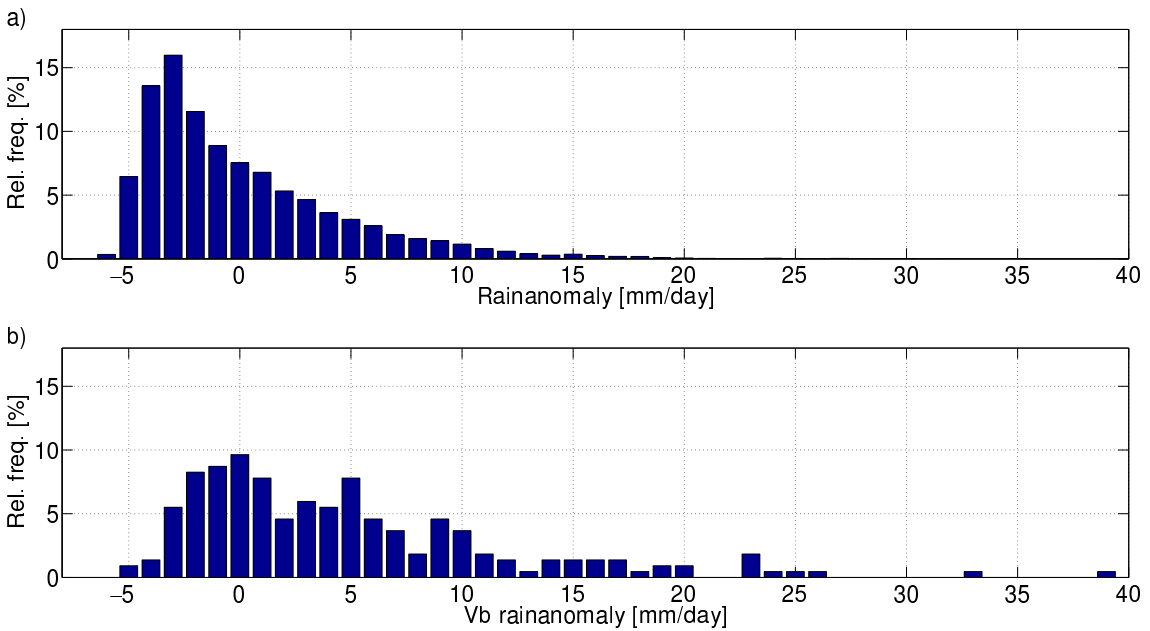


Figure 4.8: a) Histogram of rain anomalies after removing the annual cycle in the European rain area. b) As a) but only for Vb related days (black and red crosses in Fig. 4.7.)

Fig. 4.8a shows the relative frequency of the rain anomalies in Fig. 4.7, whereas Fig. 4.8b consists only of days where a Vb-type cyclone is present (black and red crosses in Fig. 4.7). The mean value of the rain anomalies that are related to Vb-type cyclones (Fig. 4.8b) is 4.73 mm/day. To test whether this Vb related mean value is significantly different from 0, which is the overall mean value, a bootstrapping technique is applied (see Section 3.1.1). Through this bootstrapping technique it is possible to estimate the 97.5th percentile of the whole population of rain anomalies. Since this 97.5th percentile is 0.62 mm/day, which is far below the 4.73 mm/day that is obtained for the Vb related rain anomalies, the mean precipitation of rain days that are related to Vb-type cyclones is significantly higher than the mean precipitation of all the rain anomalies that occur in the European rain area.

4.3 Discussion

Hofstaetter and Chimani (2012) performed a tracking of cyclones over Europe on the pressure level of 700 hPa in ERA-interim. They found that Vb-type cyclones have a mean occurrence of 3.5 cyclones per year, whereas the mean occurrence of Vb-type cyclones in this study is at 2.97 cyclones per year. One reason for this discrepancy is that the tracking techniques used by Hofstaetter and Chimani (2012) and in this study are not the same. Raible et al. (2008) and Neu et al. (2013) pointed out that there are remarkable differences in the absolute number of found cyclones between different tracking schemes. In this regard, especially the western and central Mediterranean was identified as a region where it is difficult to track and identify low pressure systems.

In this respect, the tracking schemes used by Hofstaetter and Chimani (2012), and the herein used tracking scheme by Blender et al. (1997) are compared with each other. The tracking used by Hofstaetter and Chimani (2012) method is less strict, using three criteria for an isolated minimum to be defined: (1) the gradient of $z700$ has to be positive in all four directions, (2) a minimum distance of 500 km between two minima, and (3) a minimum life time that has to be defined. The tracking algorithm by Blender et al. (1997) allows to set values for the gradient of gph that have to be exceeded (Section 3.2.1). Since the detection algorithm of Blender et al. (1997) is more strict in terms of the criteria for defining an isolated minimum it was expected that herein a somewhat smaller number of cyclones is found. In this regard, the importance of the parameter settings in a tracking and detection scheme for mid-latitude cyclones is also pointed out by Raible et al. (2008), who stated that the outcome of cyclone tracking schemes is highly dependent on the chosen parameters, and always has to be treated with caution.

Furthermore, the ERA-interim data used for the cyclone tracking in Hofstaetter and Chimani (2012) has a spatial resolution of 1.125° , whereas the ERA-interim data used in this study has a resolution of 1.5° . This spatial resolution was chosen to be consistent with the intercomparison study of cyclone tracking methods by Neu et al. (2013). The importance of the spatial resolution for the detection of mid-latitude cyclones is pointed out by Blender and Schubert (2000), who found remarkable differences between tracks identified in data sets with different spatial and temporal resolutions. In this regard, the higher the spatial resolution the less cyclone tracks are missed during the tracking procedure. However, compared with a spatial resolution of 1.125° , the probability for finding all the correct trajectories in a spatial resolution of 1.5° is according to Blender and Schubert (2000) still above 90%.

Hence, it was expectable that the herein identified amount of cyclones per year is lower than in Hofstaetter and Chimani (2012). In this sense, the lower amount of cyclones is rather expected to originate from the more strict cyclone tracking approach by Blender et al. (1997) than from the slightly lower spatial resolution of

the used ERA-interim data set.

Regarding other characteristics, Hofstaetter and Chimani (2012) found no temporal trend of Vb-type cyclones, whereas the highest probability for a Vb-type cyclone to occur is in spring, with a secondary maximum in autumn. Furthermore, Hofstaetter and Chimani (2012) found a high interannual variability, which ranges from 0 to 7 Vb-type cyclones per year. All these results are confirmed by this study.

To estimate the impact of Vb related precipitation in Switzerland, southern Germany, and Austria anomalies of daily precipitation were computed. The calculation of anomalies was chosen to subtract the climatological annual variability of precipitation on a given day in the year. This renders the precipitation values of winter and summer comparable, allowing to evaluate whether a rain anomaly that is related to a Vb-type cyclone exceeds a given percentile in a certain time of the year. However, there are other ways to investigate extreme precipitation. Raible (2007) analyzed the relationship between atmospheric circulation and cyclone intensity, and their connection to extreme precipitation. Thereby, absolute precipitation values are used, where extreme precipitation is defined as precipitation that exceeds the 90th percentile in a particular season and region. Hence, it allows to investigate the connection between extreme precipitation that is relative to a particular time and space and prevailing large scale circulation patterns and cyclone intensity. With regard to the scope of this study, the herein made choice of using anomalies to analyse the role of Vb-type cyclones with respect to extreme precipitation in Switzerland, southern Germany, and Austria is considered to be appropriate. Furthermore, Simmons et al. (2010) investigated the quality of continental precipitation from reanalyses such as ERA-interim and ERA-40 through a comparison with a new gauge-based Global Precipitation Climatology Center (GPCC) data set, which is based entirely on gauge data, and hence is derived more directly from observations. The results show that GPCC and ERA identify similar interannual continental-scale variations in precipitation. Agreement is generally better on the northern hemisphere continents and Australia than it is for South America and Africa, and better for ERA-interim than ERA-40. There is a clear shift in the mean difference from the 1990s to the latest decade between ERA-interim and GPCC, where ERA-interim shows a decline in precipitation relative to GPCC. This decline is expected to be caused by a decrease in available station data for the GPCC data. Overall, ERA-interim has higher values than GPCC. As a conclusion, the good agreement in month-to-month variability between reanalyses and observations, and the fact that the newer ERA-interim agrees better with the independent GPCC data than ERA-40 is considered encouraging for further developments of reanalysis data.

Chapter 5

Sensitivity of Vb-type cyclones to SSTs in the Mediterranean

To investigate how Vb-type cyclones react on SST changes in the Mediterranean a ctrl simulation and 10 sensitivity experiments are performed with the regional model WRF. In the first part of this chapter, the fields of $z700$ and PV along the 330 K isentropic surface, which are used to describe the intensity, and trajectory of the Vb-type cyclone in the ctrl simulation are presented and evaluated by comparing WRF results with the ERA-interim reanalysis. Furthermore, the surface upward moisture and latent heat fluxes of the ctrl simulation are presented to assess relevant processes regarding cyclogenesis and intensification. Also, the distribution of precipitation in the ctrl simulation in the Swiss rain area is presented. In the second part, the results of the sensitivity experiments are presented, where the influence of changes in Mediterranean SSTs on cyclone intensity and tracks is discussed. In this respect, the differences of the aforementioned variables between the ctrl simulation and the sensitivity experiment that show the strongest impact in precipitation in the Swiss rain area are presented to understand the underlying physical processes.

5.1 Ctrl simulation

A first impression of the performance of WRF and the data provided by ERA-interim in terms of the trajectory and intensity of the simulated Vb-type cyclone is shown in Fig. 5.1. $z700$ is shown for four subsequent snapshots over the western Mediterranean and central Europe separated by 24 hours. This region is considered to be most important regarding growth and propagation of Vb-type cyclones (Fig. 1.1). Figure 5.1 shows WRF output taken from domain D4, which has a spatial resolution of 4 km. The low pressure system of interest is clearly visible and well reproduced. However, there are high frequency characteristics that can be regarded as artefacts in the field of $z700$ in WRF (Fig. 5.1a). Therefore, the direct WRF output of domain D4 could not be used to obtain meaningful trajectories. Hence, the WRF output from domain D4 is smoothed by the method introduced in Section 3.2.2 in order to remove the high frequency noise (Fig. 5.1b). The simulated $z700$ show clear similarities to ERA-interim. Except for the situation on August 21 (12

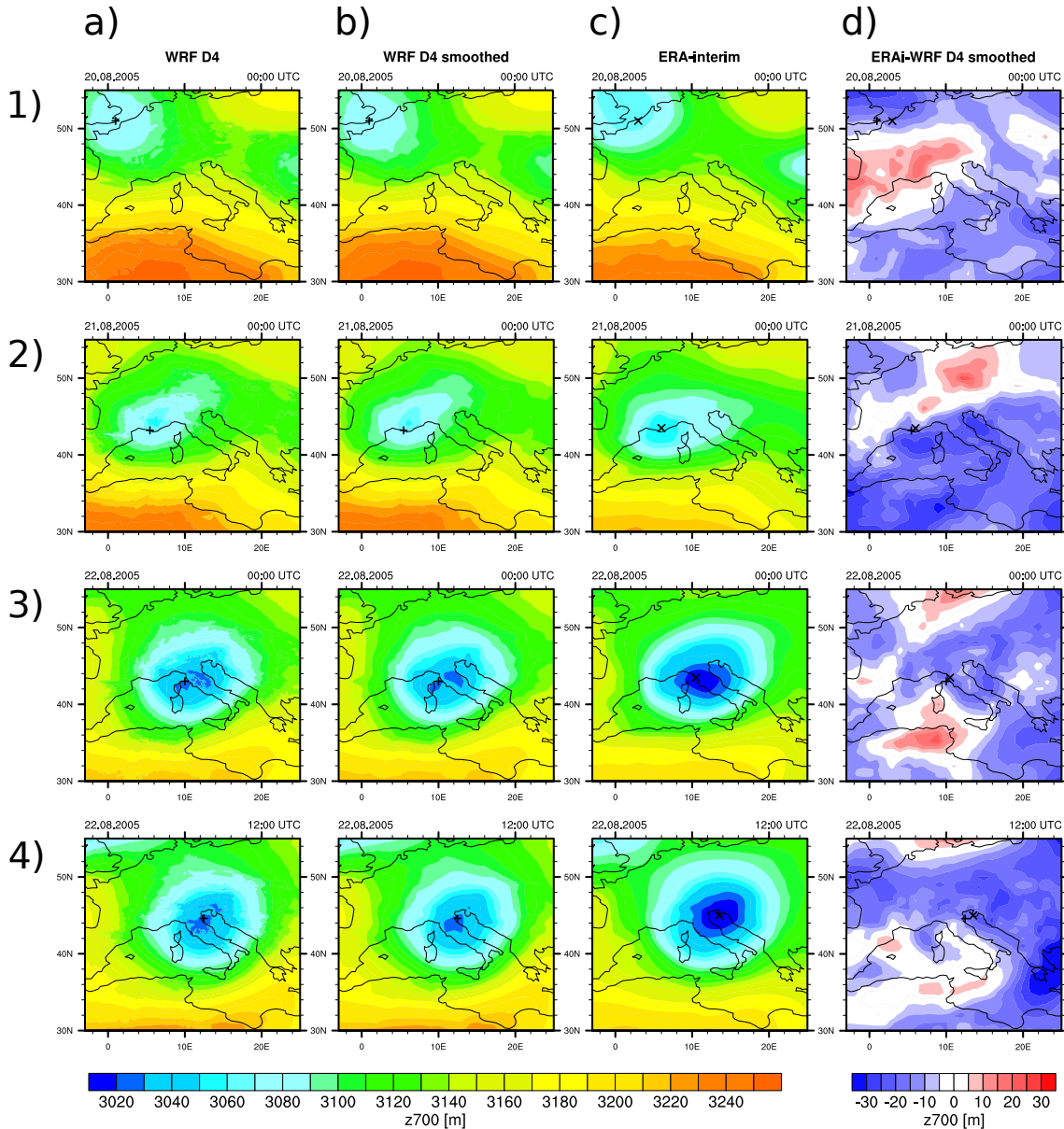


Figure 5.1: z_{700} fields for 4 time steps and different data sets. The columns from left to right show: a) The WRF ctrl simulation in the domain D4, b) the smoothed domain D4 as simulated by the WRF ctrl simulation, c) ERA-interim, d) the differences between ERA-interim and WRF D4 smoothed. The time steps are shown in 1) to 4), starting with the first time step simulated by WRF, and the following two separated by 24 hours, whereas the last shown time step is on August 23, 2005 (12 UTC). Furthermore, the particular locations of the minima of z_{700} in WRF are indicated with “+”-symbols, whereas the particular locations of the minima of z_{700} in ERA-interim are indicated with “x”-symbols.

UTC) the $z700$ low pressure system seems to be slightly deeper and more extended over the domain in ERA-interim than in WRF. However, as visible in Fig. 5.1d, where the differences in $z700$ between ERA-interim and the smoothed output of the WRF domain D4 for corresponding time steps are presented, the simulated cyclone is not clearly visible as a difference in the deepening rate of $z700$ between ERA-interim and WRF, suggesting that there are no remarkable differences in intensity. This is also confirmed by Fig. 5.2, which shows the mean difference in $z700$ over all

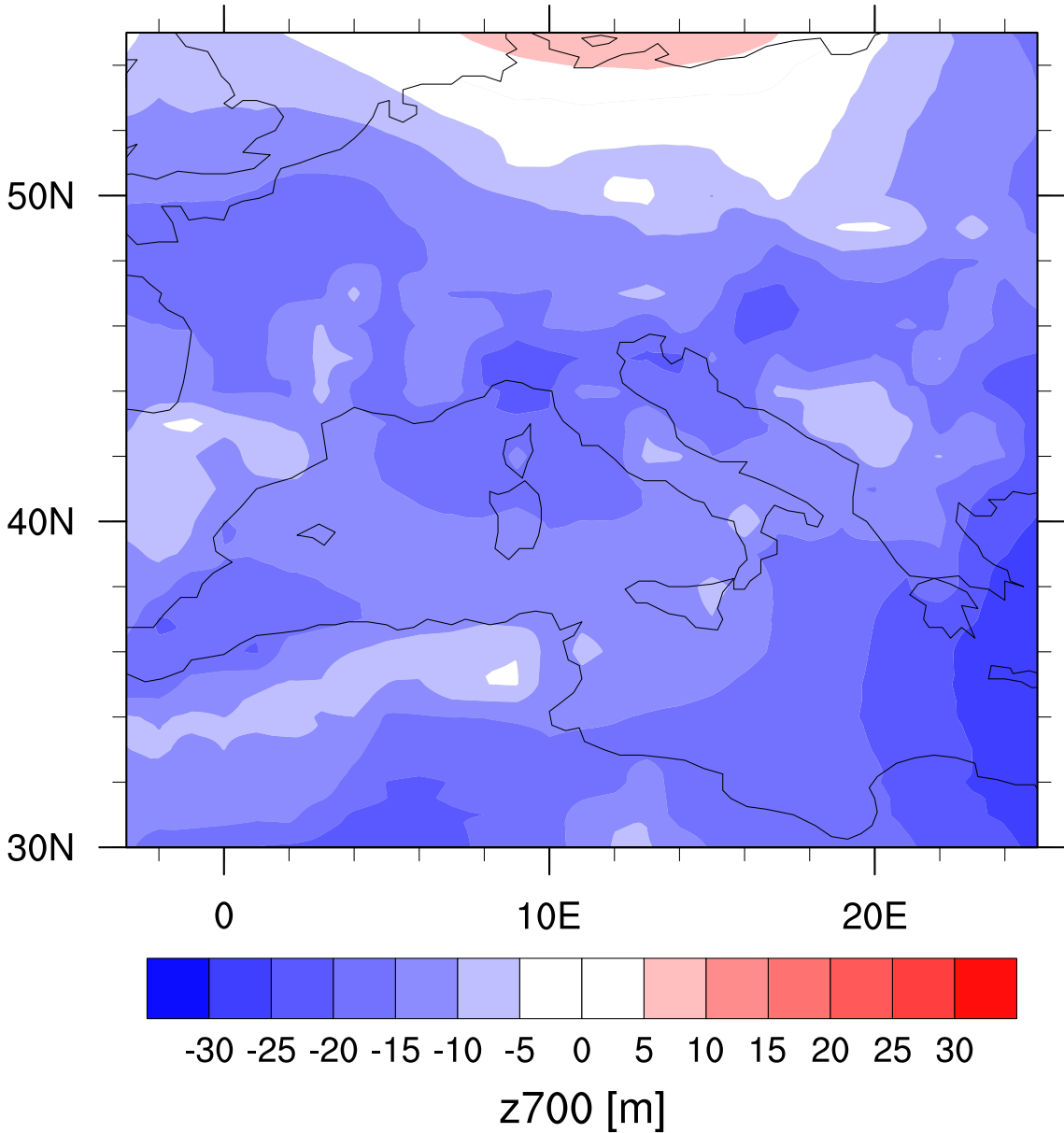


Figure 5.2: Mean differences of $z700$ between ERA-interim and the smoothed domain D4 of WRF. The ERA-interim data was interpolated to the grid of the WRF domain D4 to calculate the mean values for every grid point over all the time steps.

the time steps between the WRF domain D4 and ERA-interim over central Europe and the western Mediterranean. The negative values in Fig. 5.2 indicate lower values in $z700$ in ERA-interim, which are present over the whole considered area, suggesting that there is a systematic bias between the WRF output and ERA-interim, rather than a cyclone that is more intense in ERA-interim.

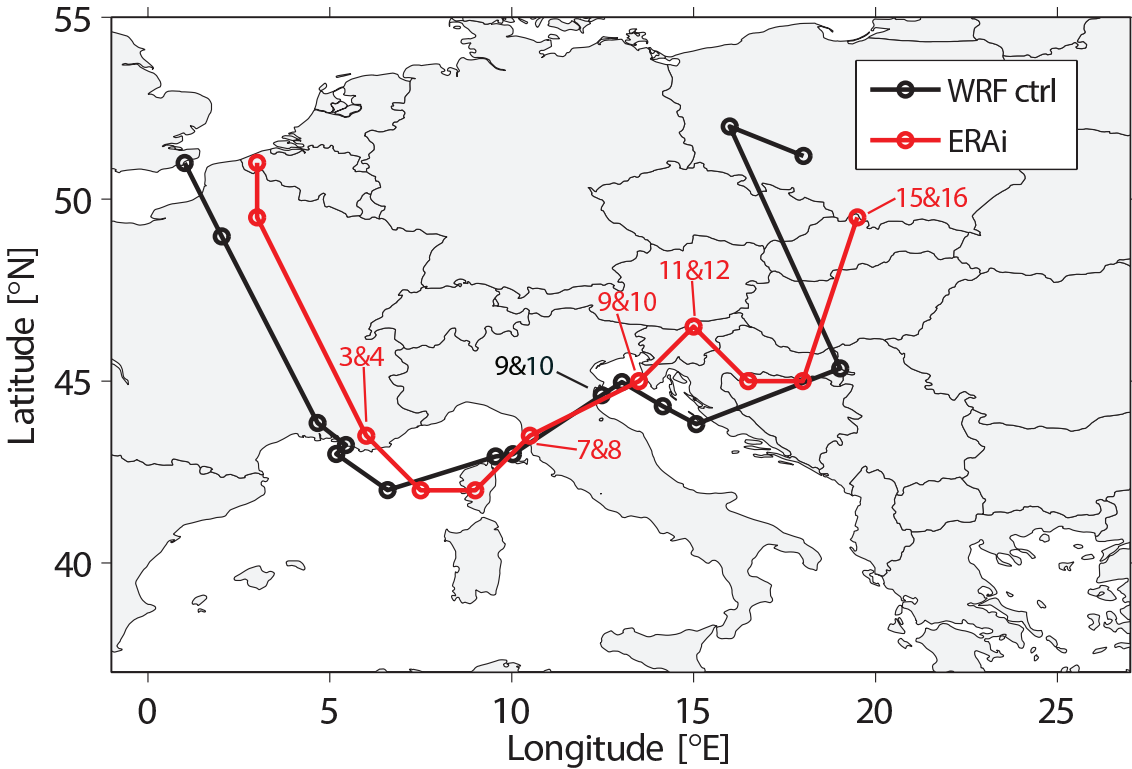


Figure 5.3: Tracks identified in the WRF ctrl simulation in the smoothed domain D4 and in ERA-interim. The WRF track is shown in black and the ERA-interim track is shown in red. The points indicate the cyclone centers, i.e., the minima in $z700$. All the time steps that coincide with each other are marked. Furthermore, the time steps 1, 4, 8, and 10 correspond to the time steps shown in Fig. 5.1.

As already indicated, one way to assess the intensification of a cyclone is to consider the deepening rate of $z700$ over a certain time, whereas the intensity can be assessed considering the absolute gph of $z700$. Therefore, the locations of the minima in $z700$ in the cyclone center have to be identified. This also allows to assess the similarity of the trajectories. In this respect, Figure 5.3 shows the track of the WRF ctrl simulation using the smoothed field of $z700$ of the domain D4 in black and the same in ERA-interim in red. The time steps 3&4, 7&8, 9&10, 11&12, and 15&16 of the ERA-interim trajectory coincide with each other, whereas the time steps 9&10 are congruent on the trajectory as identified in WRF. Overall, the track identified in the smoothed WRF domain D4 is similar to the trajectory found in ERA-interim. From the beginning of the tracks until the Adriatic Sea, there are

no remarkable differences between the two trajectories. However, at the western coast of the Adriatic Sea the two tracks start to slightly deviate. In this regard, 72 and 78 hours after initialization the WRF track is located over the Adriatic Sea, whereas the trajectory in ERA-interim is located more northward over northern Slovenia. This is an effect of the tracking tool used for the WRF output, which only considers grid points that are located over orography that is lower than 200 meters a.s.l. Hence, the WRF output is forced to stay over the Mediterranean, whereas the ERA-interim track goes northward towards Austria. Subsequently, the two tracks proceed generally in the same direction, with continual convergence and divergence. In the end, the WRF track ends in central Poland, and the ERA-interim track ends in western Ukraine.

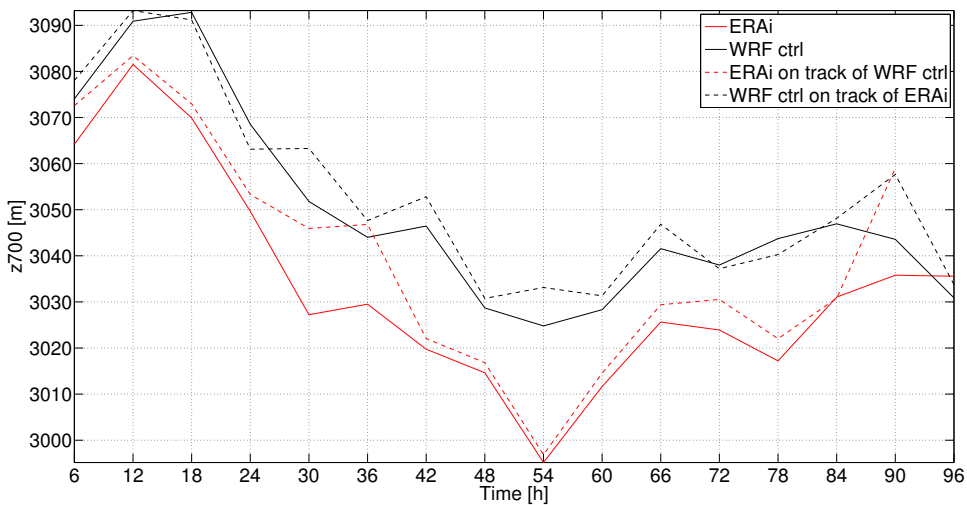


Figure 5.4: Life cycles of $z700$ minima on the different trajectories of Fig. 5.3. The smoothed WRF ctrl output of the domain D4 is represented by the solid black line, whereas the ERA-interim output is represented by the solid red line. The dashed lines show the life cycles of $z700$ minima in WRF on the track where the identified ERA-interim minima are located (black dashed), and of ERA-interim where the identified WRF minima are located (red dashed).

Given that the trajectories between WRF and ERA-interim are similar, absolute values and the temporal deepening rate in $z700$ minima between the two tracks are compared. To do so, the solid lines in Fig. 5.4 show the life cycles of the $z700$ minima of ERA-interim and WRF. The overall life cycles of the considered field minima in $z700$ are similar. In both fields the lowest value is located 54 hours after the initialization. Until this time, both time series show a negative trend, and hence increase in their intensity. WRF is able to reproduce the overall structure of the temporal evolution of $z700$. This is also shown by the similar deepening rates between 18 and 54 hours after the initialization, which in WRF is about 70 gpm and in ERA-interim about 75 gpm. The dashed lines show the values of $z700$ of

ERA-interim on the track in WRF and vice versa. The dashed red line is always above the solid red line, suggesting that the tracking scheme by Blender et al. (1997), which is used for the cyclone tracking in ERA-interim, works properly and always finds the minimum in $z700$. The dashed black line is also mostly above the black solid line except for four time steps at 18, 24, 72, and 78 hours after the initialization. Thereby, the differences are remarkably larger at 24 and 78 hours. In this regard, the height criterion of the WRF tracking tool might be responsible for the roughly 5 gpm discrepancy at 24 hours after the initialization, since at this time step the minimum in ERA-interim is located over southern France, while the minimum identified in WRF is located at the French coast of the Mediterranean Sea, where a reduced elevation is present. Hence, the height criterion of the WRF tracking tool is the reason that the minimum $z700$ value 24 hours after initialization at the location identified by Blender et al. (1997), is not found by the employed WRF tracking technique. Moreover, 72 and 78 hours after the initialization are exactly the time steps where, as explained above, the WRF output is forced to stay over the Mediterranean, whereas the ERA-interim trajectory moves over land, suggesting again the height criterion to be responsible for the lower values in $z700$ found in WRF on the track identified by Blender et al. (1997). In an overall view, during the middle part of the life cycle where the strongest intensification takes place, the tracking technique used for the WRF output seemingly finds the correct minimum values in $z700$. There is a constant offset of about 15-25 gpm between the life cycles of $z700$ minima found in WRF and ERA-interim, which confirms the systematic bias suggested by Fig. 5.2.

Since one scope of this study is to gain insight into the sensitivity of precipitation to Mediterranean SSTs, not only the intensity, but also vertical moisture and latent heat fluxes that are related to the simulated cyclone are of interest. The choice of the first shown time step of upward moisture and latent heat fluxes was made in accordance with two criteria: (1) the spin-up phase of the model, which are the first 12-18 hours after the initialization, is finished, and (2) the center of the simulated low pressure system still has to be over land (Fig. 5.12), to prevent the simulated cyclone from being too strongly influenced by the Mediterranean Sea. Thus, this first time step is at 24 hours after the initialization on August 21, 2005 (00 UTC), and hence corresponds to time step 2) shown in Fig. 5.1. The second time step was chosen at a time where precipitation differences in Switzerland between the WRF sensitivity experiments and the WRF ctrl simulation appear to be largest. Thus, this second time is selected at 60 hours after the initialization on August 22, 2005 (12 UTC), and hence corresponds to time step 4) shown in Fig. 5.1. At this time, the simulated low pressure system is substantially influenced by the Mediterranean Sea, since it already moved over the Gulf of Genoa, and is located over the Adriatic Sea (Fig. 5.14). These two time steps are used to show the influence of the Mediterranean in terms of moisture supply for the simulated Vb-type cyclone. Hereinafter, these two time steps are shown for all the variables that are used to investigate the physical properties of the simulated Vb-type cyclone.

The vertical upward moisture flux on August 21, 2005 (00 UTC) over central Europe is presented in Fig. 5.5. The WRF ctrl simulation and ERA-interim show similar spatial distributions (Fig. 5.5a,b). Most parts in the WRF ctrl simulation experience upward moisture fluxes between 0 and 6×10^{-5} $\text{kgm}^{-2}\text{s}^{-1}$ (Fig. 5.5a). In the region around the Balearic Islands moisture fluxes are more intense, with values in WRF between 2×10^{-4} and 2.6×10^{-4} $\text{kgm}^{-2}\text{s}^{-1}$. ERA-interim only shows maximum values between 1.2×10^{-4} and 2.4×10^{-4} $\text{kgm}^{-2}\text{s}^{-1}$. WRF is expected to simulate a more differentiated distribution of moisture fluxes with higher values since it operates with a substantially higher spatial resolution compared with ERA-interim. Figure 5.5c shows the situation in WRF 60 hours after the initialization on August 22 (12 UTC). Again, moisture fluxes at this time show similar patterns in ERA-interim (Fig. 5.5d). At this time, larger parts of the Mediterranean Sea show increased fluxes. Maximum values in the WRF ctrl simulation are now between 2.2×10^{-4} and 2.6×10^{-4} $\text{kgm}^{-2}\text{s}^{-1}$, whereas the maximum values in ERA-interim are between 1.2×10^{-4} and 2×10^{-4} $\text{kgm}^{-2}\text{s}^{-1}$. The maximum moisture fluxes in WRF are now shifted offshore and are located between the Balearic Islands and Corsica.

Not only moisture fluxes but also latent heat fluxes are interesting, especially to assess processes regarding cyclogenesis in the mid-troposphere. In this regard, the vertical upward latent heat flux at the surface as simulated by the WRF ctrl simulation is compared with ERA-interim (Fig. 5.6). As expected, the distribution of latent heat fluxes resembles to the spatial pattern of vertical moisture fluxes. The maximum latent heat fluxes 24 hours after the initialization in WRF ctrl are between 550 and 650 W/m^2 (Fig. 5.6a), whereas the latent heat fluxes in ERA-interim only amount to maximum values of 400 W/m^2 (Fig. 5.5b). 60 hours after the initialization, the maximum latent heat fluxes in both WRF ctrl and ERA-interim are located between the Balearic Islands and Corsica. At this time, latent heat fluxes in WRF ctrl reaches values between 500 and 600 W/m^2 , whereas in ERA-interim values between 400 and 450 W/m^2 are found (Fig. 5.5c,d). Hence, WRF simulates moisture and latent heat fluxes that are partially more intense and depicts a more differentiated picture of these processes. In this respect, the higher fluxes in WRF are expected since it simulates with a much higher spatial resolution than ERA-interim.

A further look at the data in WRF ctrl reveals that both upward latent heat and moisture fluxes start to substantially increase 20 to 24 hours after the initialization in the night from August 20 to August 21, 2005. This is the time where according to MeteoSchweiz (2006) a surface low pressure system forms over the Gulf of Genoa just before the upper level cyclone moves over the MB (Fig. 5.12,3), where it merges with the surface low. Thus, the vertical movement of air triggered by the surface and upper level low pressure systems over the Gulf of Genoa increases the considered vertical fluxes, which are stronger in locations where the SSTs are higher (Fig. 2.7).

As explained in Chapter 1, latent heat fluxes are able to influence PV , which is used as an indicator for cyclogenesis. Therefore, the distribution of PV at the 330

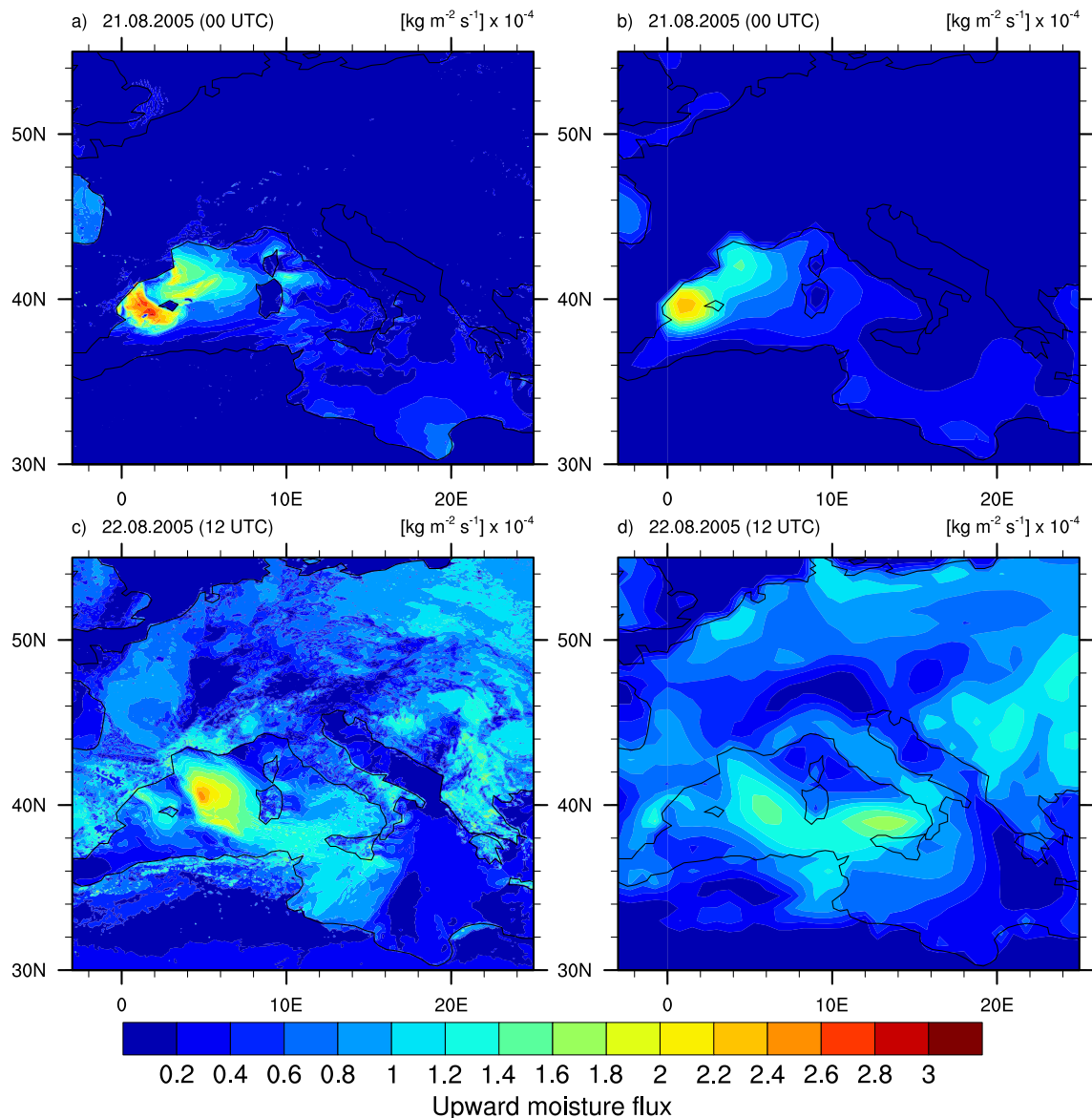


Figure 5.5: a) Upward moisture fluxes over central Europe and the western Mediterranean of WRF ctrl 24 hours after the initialization. b) same as a) in ERA-interim. c) Same as a) 60 hours after the initialization. d) Same as a) in ERA-interim 60 hours after the initialization.

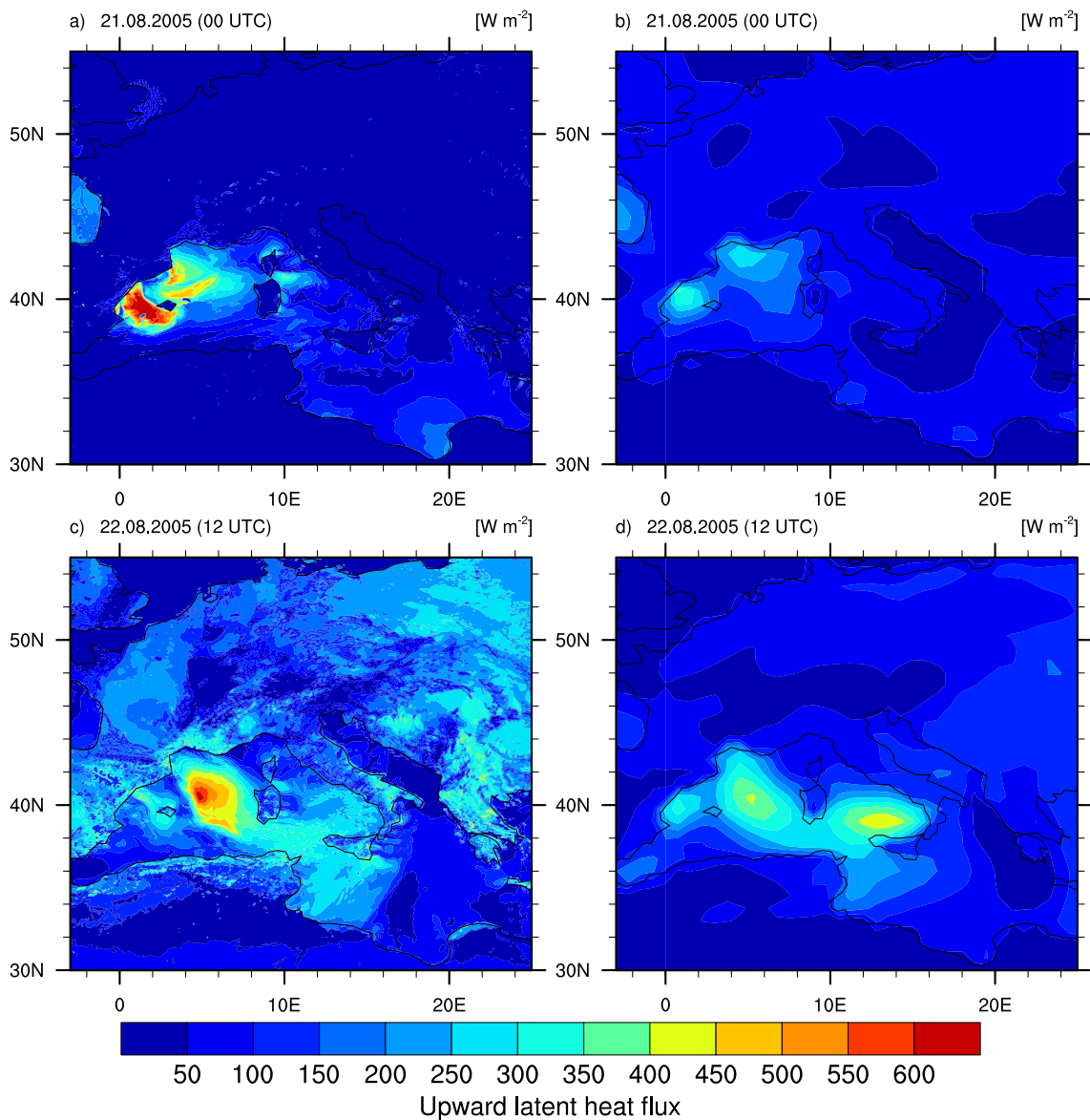


Figure 5.6: a) Upward latent heat fluxes over central Europe and the western Mediterranean of WRF ctrl 24 hours after the initialization. b) Same as a) in ERA-interim. c) Same as a) 60 hours after the initialization. d) Same as a) in ERA-interim 60 hours after the initialization.

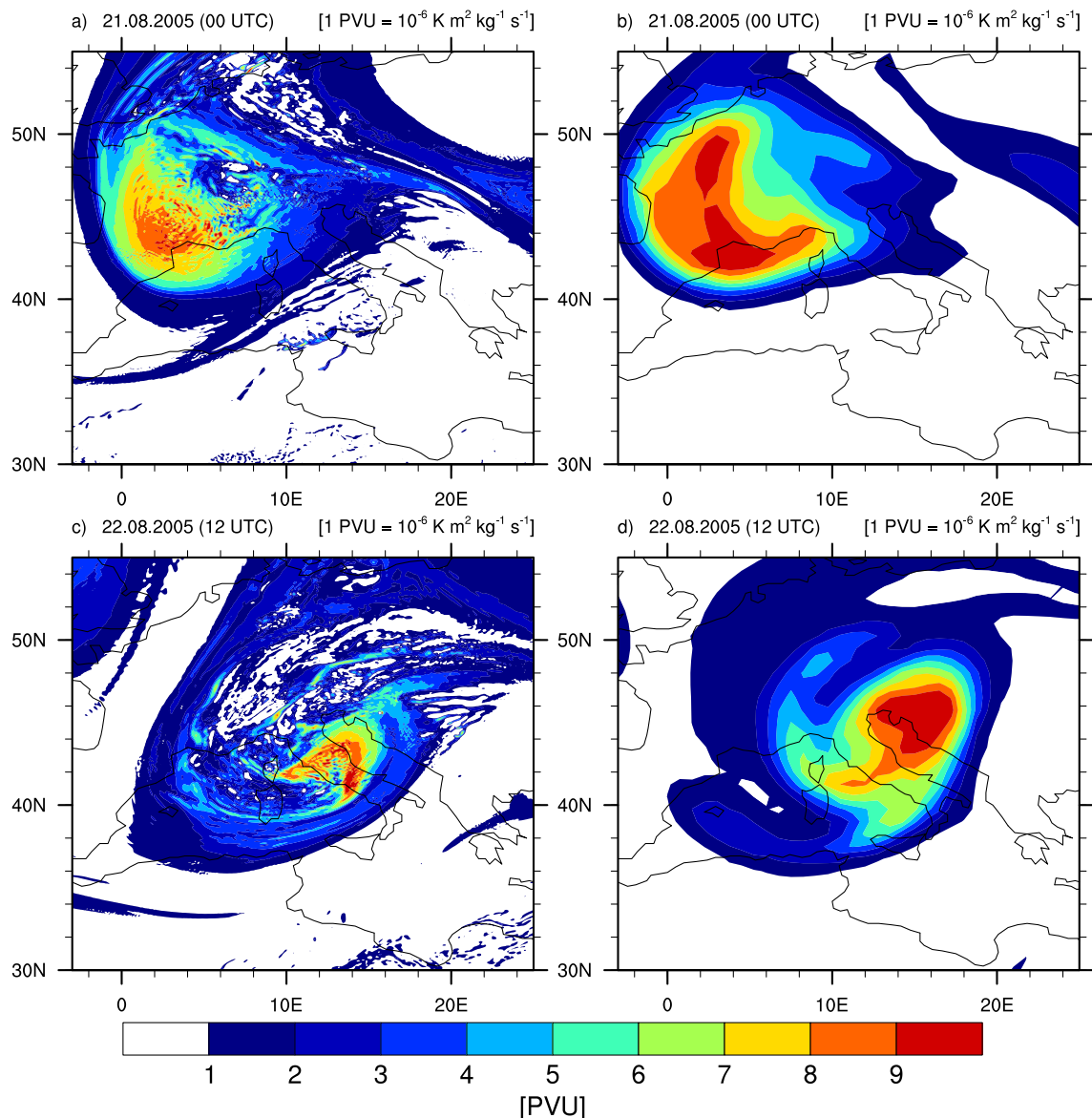


Figure 5.7: a) *PV* at the 330 K isentropic surface of WRF ctrl in the domain D4 24 hours after the initialization. b) Same as a) in ERA-interim. c) Same as a) 60 hours after the initialization. d) Same as a) in ERA-interim 60 hours after the initialization.

K isentropic surface of the WRF model and ERA-interim is given by Fig. 5.7. In summer at 45°N, the 330 K isentropic surface is located in the troposphere close by to the dynamical tropopause at about 300 hPa, and a height of about 9 km above sea level (Fig. 1.3). In the two shown time steps for the WRF domain D4 (Fig. 5.7a,c) there are two positive *PV* anomalies discernable that are similar to the data provided by ERA-interim (Fig. 5.7b,d). The two centers of the *PV* anomalies shown in Fig. 5.7b,d, with maximum values above 9 PVU, are similar to the *PV* maxima in WRF. In terms of their size they are more extended and smoother than the *PV* centers of WRF. This is understandable since the data by ERA-interim has a resolution of 1.5°. Overall, WRF is able to accurately reproduce the fields in ERA-interim regarding *PV* on the 330 K isentropic surface in the two chosen time steps.

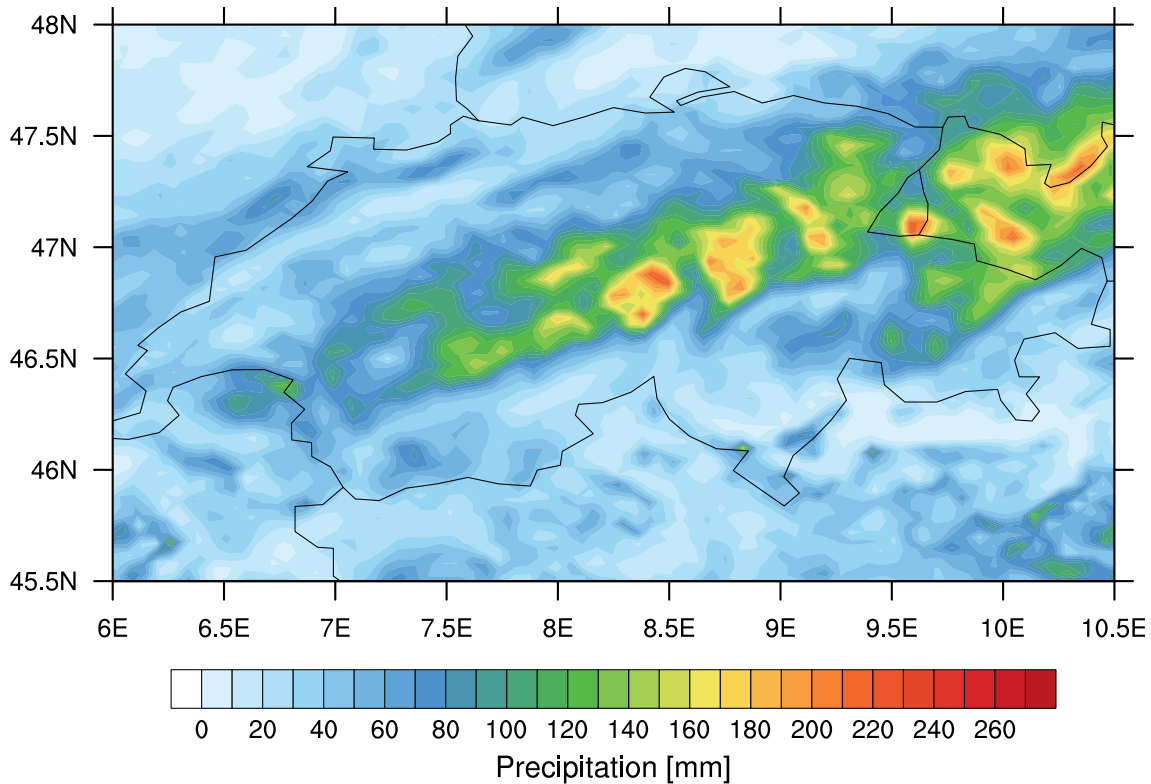


Figure 5.8: Distribution of accumulated precipitation in WRF ctrl in the domain D4 from August 20 (00 UTC) to August 24, 2005 (00 UTC) in Switzerland.

To assess the sensitivity of precipitation in Switzerland to SSTs in the Mediterranean the reference distribution of rain from the WRF ctrl simulation has to be assessed and compared with observations. Therefore, accumulated precipitation in the WRF domain D4 from August 20 (00 UTC) to August 24, 2005 (00 UTC) is presented (Fig. 5.8). The accumulated precipitation distribution as it is present in the WRF ctrl simulation is similar to observational data (Fig. 1.2). There is a clear maximum of precipitation observable in the alpine area. Furthermore, the WRF

ctrl precipitation mean value for the aforementioned time period in the Swiss rain area is 89.42 mm, whereas MeteoSwiss observes a mean of 110.1 mm in the same area and time. Although not equal, these two values are not significantly different, as confirmed by a t-test ($p < 0.05$).

5.2 Sensitivity experiments

A number of sensitivity experiments are performed to investigate the influence of Mediterranean SSTs on Vb related precipitation in Switzerland in case of the Vb-type cyclone in August 2005. In this section, the results of these sensitivity experiments are presented and compared with the WRF ctrl simulation.

In this regard, the tracks and the temporal evolutions of $z700$ minima from the sensitivity experiments are shown and compared with the tracks and temporal evolutions of the WRF ctrl simulation (Figs. 5.9, 5.10). Furthermore, the sensitivity experiment that exhibits the largest differences in precipitation relative to the ctrl simulation is used to illustrate the differences of vertical upward latent heat and moisture fluxes, and PV (Figs. 5.13, 5.11, 5.12). Also, vertical cross sections of potential vorticity tendency (PVT) and the diabatic heating part of PVT are shown to illustrate the physical processes that are present in the mid-troposphere (Figs. 5.15, 5.16, 5.17, 5.18). Finally, the accumulated precipitation field mean values simulated by the domain D4 of WRF from August 20 (00 UTC) to August 24, 2005 (00 UTC) for the Swiss rain area are shown for every sensitivity experiment (Fig. 5.19). Besides, time series of 6-hourly precipitation are shown in order to identify the time step where the strongest reaction of precipitation across the different sensitivity experiments occurs (Fig. 5.20).

The assessment of the WRF sensitivity experiments starts again by considering the trajectories. Figure 5.9 shows the identified trajectories of $z700$ minima in the smoothed WRF domain D4 for all the sensitivity experiments, and the ctrl simulation. In the first three time steps all the trajectories are very close to each other, which is a consequence of the spin-up phase. For the rest of the time steps, most of the trajectories are similar to the track of the ctrl simulation (black line in Fig. 5.9). However, the tracks of the -3 K, -4 K, and -5 K experiments deviate to the east after they passed over Croatia, whereas the tracks of the +3 K, +4 K, and the +5 K experiments show clear deviations to the west after they passed over the Adriatic Sea. Most of the tracks show no substantial meridional deviations. Only the tracks of the +2 K and the +3 K experiments show a slight deviation to the south over the northern part of the Italian Peninsula for the +3 K experiment, and a bit shifted to the west for the +2 K experiment.

The corresponding life cycles of the minima in $z700$ are, in terms of the overall structure, similar for all the sensitivity experiments (Fig. 5.10). All the cyclones start at 3075 gpm and increase to 3090 gpm at 18 hours after the initialization. This is again a consequence of the spin-up phase. Afterwards, $z700$ decreases in all the

sensitivity experiments and reaches its minimum at 54 hours after the initialization.

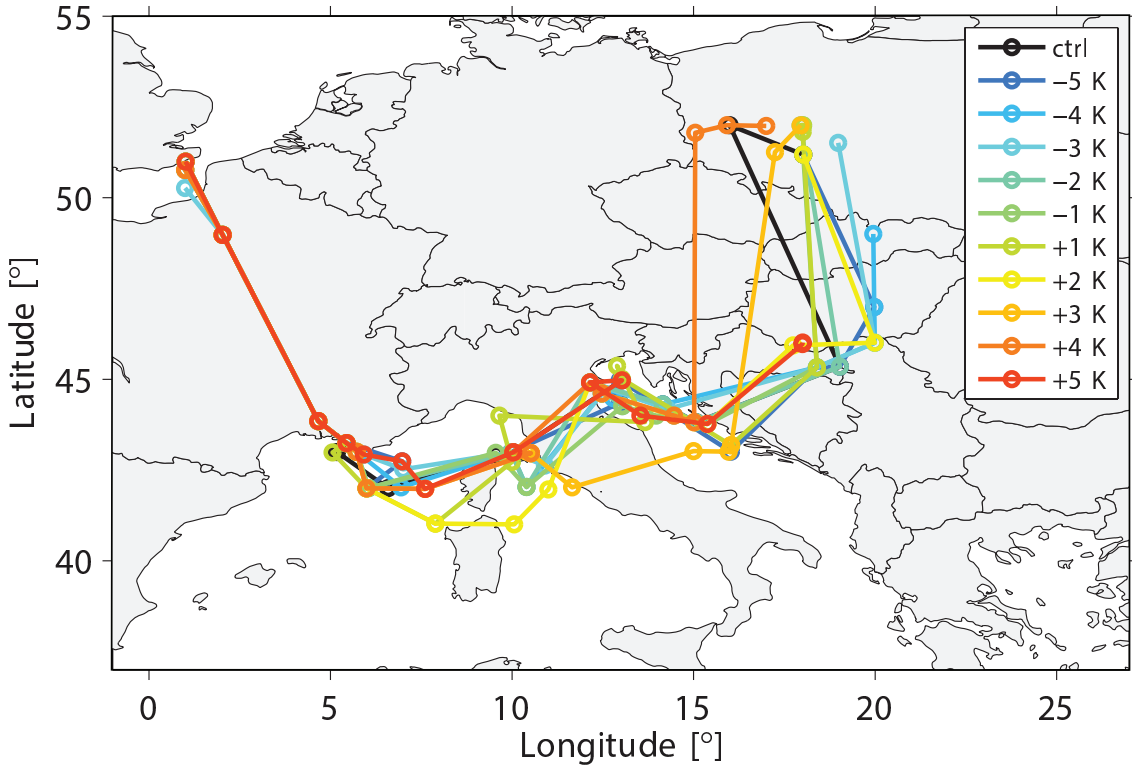


Figure 5.9: Trajectories of $z700$ minima of the WRF sensitivity experiments and the WRF ctrl simulation. The ctrl simulation is shown in black.

However, after the aforementioned 18 hours after the initialization, the minima of $z700$ of the +3 K, +4 K, and +5 K experiments start to become substantially lower than in the ctrl simulation. The +5 K experiment exhibits an absolute minimum value of 2992 gpm. This value is substantially lower than $z700$ of the ctrl simulation at the same point, which amounts to 3026 gpm.

After analyzing the impact of SST variations in the MB on the trajectories and intensification of the simulated Vb-type cyclone, it is of interest to investigate the implications of these SST variations to variables that are more related to precipitation. In this regard, the differences in vertical upward moisture and latent heat fluxes at the surface in the domain D4 between the ctrl simulation and the +5 K experiment are presented in Figs. 5.11 and 5.12.

The situation 24 hours after the initialization is presented in Fig. 5.11a and 5.12a, whereas Figures 5.11b and 5.12b present the situation 60 hours after the initialization. Both flux fields show increased values due to higher SSTs, which lead to more evaporation of water. This increases the moisture flux in terms of water vapor that rises from the surface. When this increased amount of water vapor condensates

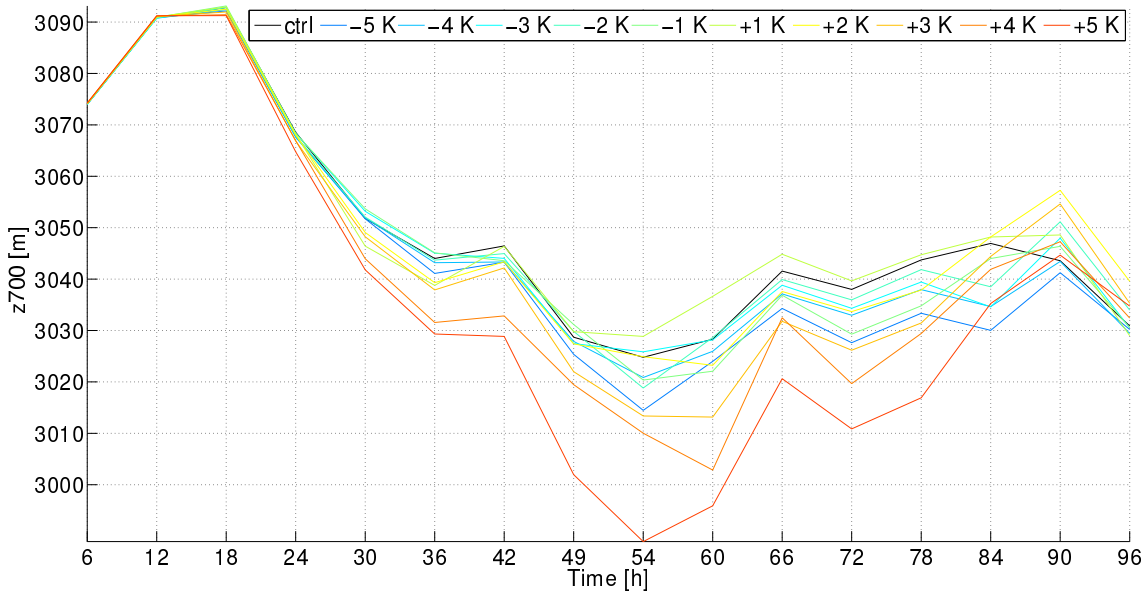


Figure 5.10: Life cycles of $z700$ minima of the WRF sensitivity experiments and the WRF ctrl simulation. The ctrl simulation is shown in black.

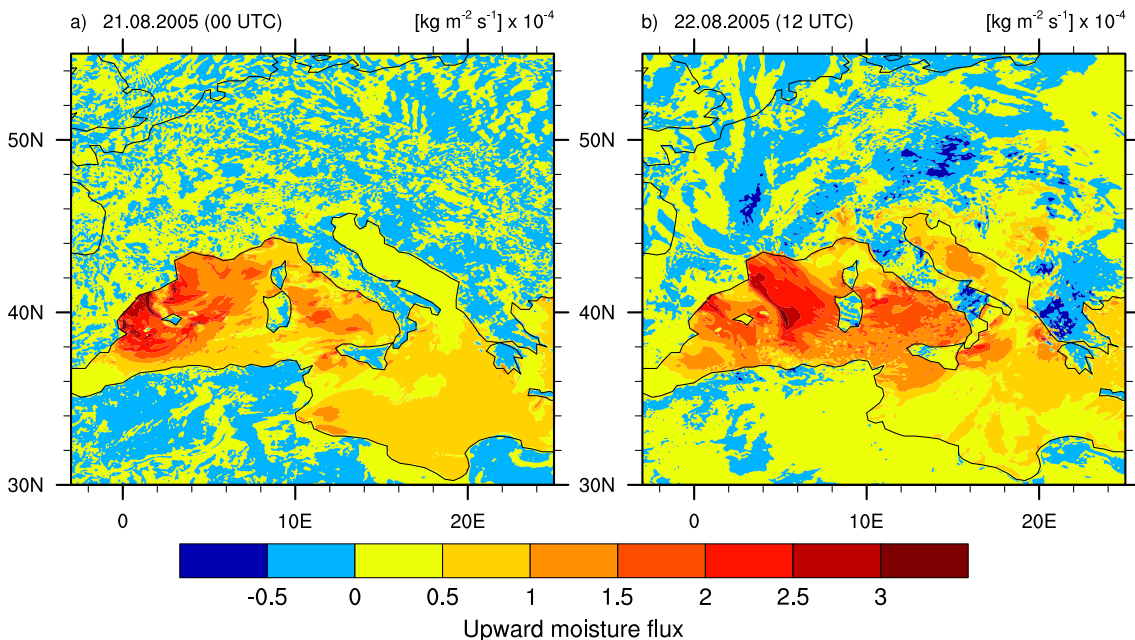


Figure 5.11: Difference in upward moisture fluxes between the +5 K experiment and the WRF ctrl simulation for a) 24 hours after the initialization and b) 60 hours after the initialization.

heat is released, which warms up the atmosphere at higher levels. This heat is called latent heat, since it is a background heat flux which only gets released when water condenses. Hence, the increasing moisture and latent heat fluxes with increasing SSTs in the MB are expectable and well simulated by WRF. The largest increases in both fluxes are found in an area that covers the coast from Monaco in France to Alacant in Spain with highest values between Barcelona and Valencia. In these locations, the differences in vertical moisture fluxes are between 3×10^{-4} and $3.5 \times 10^{-4} \text{ kgm}^{-2}\text{s}^{-1}$, and the differences in latent heat fluxes are $800 - 1000 \text{ Wm}^{-2}$.

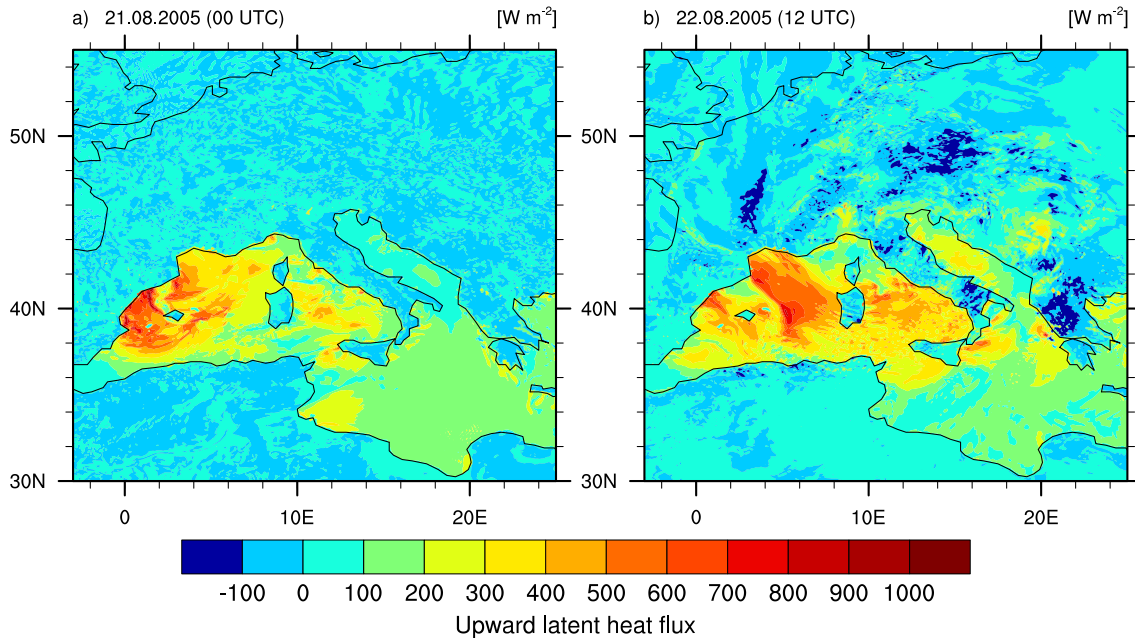


Figure 5.12: Difference in upward latent heat fluxes between the +5 K experiment and the WRF ctrl simulation for a) 24 hours after the initialization and b) 60 hours after the initialization.

Furthermore, the increases in moisture and latent heat fluxes are spatially more extended 60 hours after the initialization. Also this is somewhat expected since the center of the simulated cyclone in the first presented time step is not yet located over the Mediterranean. In this regard, the latent heat and moisture fluxes only start to get remarkably increased with cyclonic activity over the MB. From a theoretical point of view this is understandable since low pressure systems exhibit an upward motion on the affected air parcels (Martin, 2006).

To check whether changes in vertical moisture and latent heat fluxes have an impact on cyclogenesis in the upper troposphere, differences in *PV* on the 330 K isentropic surface between the WRF ctrl simulation of the domain D4 and the WRF +5 K sensitivity experiment are presented in Fig. 5.13. 24 hours after the initialization there are slight differences between the ctrl simulation and the +5 K experiment, whereas 60 hours after the initialization pronounced differences are simulated. The

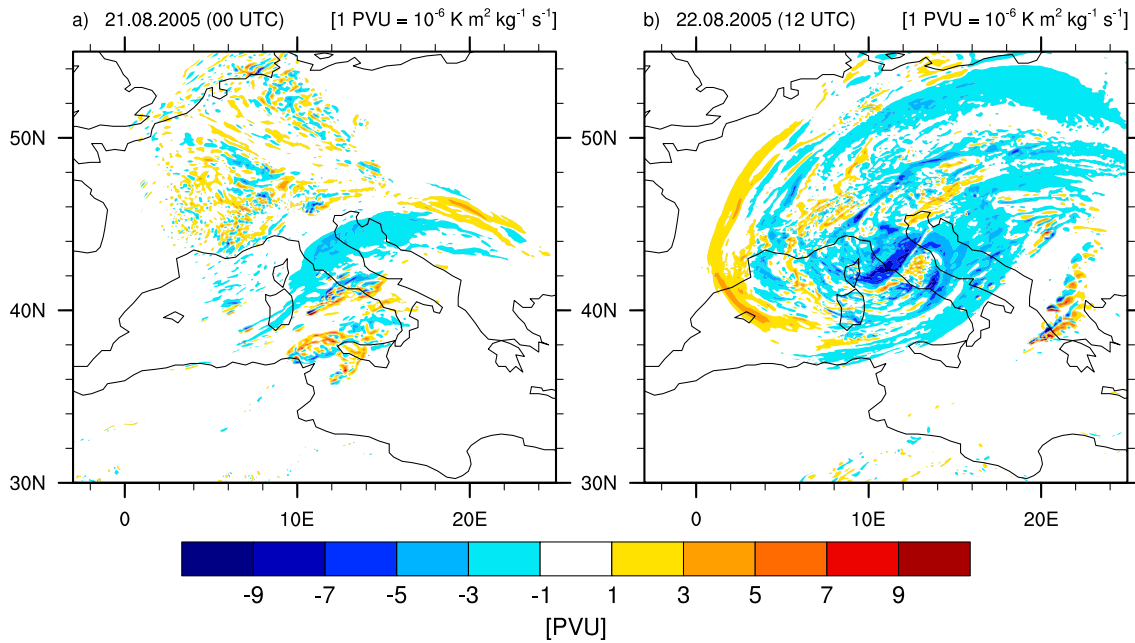


Figure 5.13: Difference in PV between the $+5$ K experiment and the WRF ctrl simulation for a) 24 hours after the initialization and b) 60 hours after the initialization.

positive PV anomalies over the Mediterranean that are present in the ctrl simulation are generally lower in the $+5$ K experiment (Fig. 5.13b). Thus, there is a relationship between lower upper level PV (along the 330 K isentropic surface) and SSTs, that are higher relative to the WRF ctrl simulation, and vice versa (Fig. 5.14). It follows from Eq. 1.2 that PV gets produced if the vertical gradient of the diabatic heating rate is positive, and destroyed if it is negative. Latent heating is a form of diabatic heating, and, as seen before, the differences of latent heat fluxes over the Mediterranean between the ctrl and the $+5$ K experiments are clearly positive.

Therefore, to check whether diabatical processes are responsible for the changes in upper level PV , and whether there is a vertical shift of cyclogenetic activity, vertical cross sections of PV tendency (PVT) and the vertical material change of PV due to diabatic heating ($\frac{D}{Dt}PV$) in the WRF domain D4 are analyzed. PVT indicates the temporal tendency of PV production or destruction due to PV advection and diabatic and frictional PV sources (Tory et al., 2011), whereas the material change represents the alteration of PV due to diabatic processes following an air parcel in the vertical. Thereby, the ctrl simulation and the differences between the $+5$ K experiment and the ctrl simulation in PVT are shown in Figs. 5.15 and 5.16, whereas the same for $\frac{D}{Dt}PV$ due to diabatic heating is presented in Fig. 5.17 and 5.18. Again the two time steps at 24 h and 60 h after the initialization are selected. The location of the vertical cross sections are chosen along the latitudes, where the maximum positive PV values in Fig. 5.7 are found. Thus, along the latitude of 48°N from 1°W to 5°E for the first time step and along the latitude of 44°N from 12°E to 18°E for the second time step. Along these latitudes, the patterns in the presented

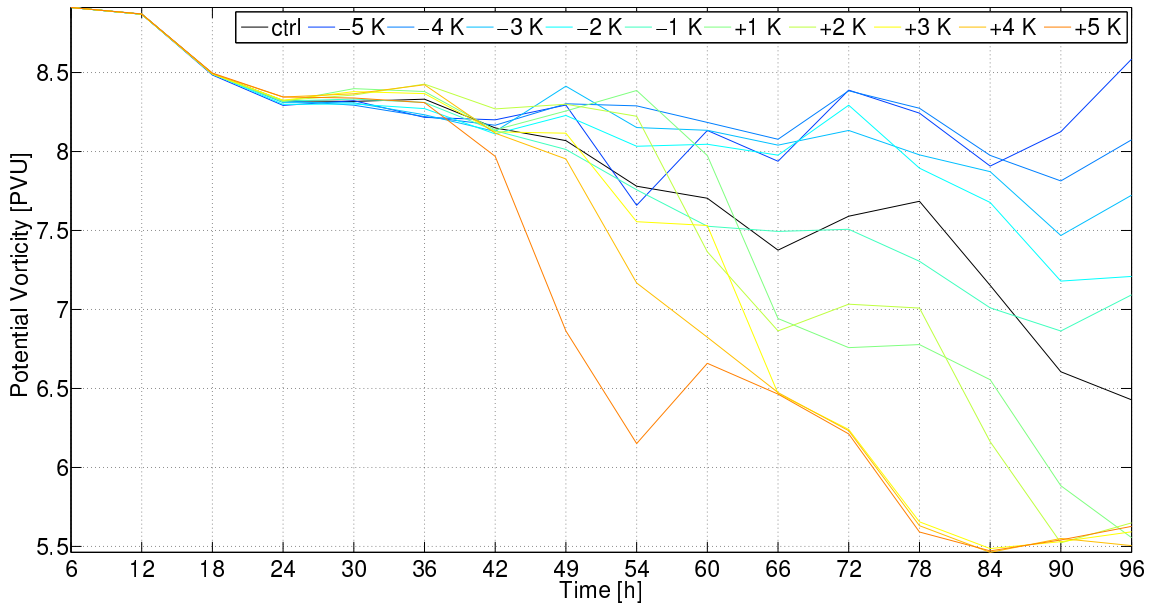


Figure 5.14: Life cycles of PV maxima along the 330 K isentropic surface in the WRF sensitivity experiments and the ctrl simulation. The ctrl simulation is shown in black.

vertical cross sections are most interesting at the longitudes where the maxima of the PV anomalies in Fig. 5.7 are located. This is for the first time step at 2°E, and for the second time step at 16°E.

The vertical coordinate are η -levels and on the y -axis potential temperature is presented. The η -levels are curved in this representation because they follow the orography and, hence deviate from the isentropic surfaces. The straight black line in the horizontal shows the 330 K isentropic surface, whereas the straight black line in the vertical is the longitude where the upper level PV anomaly in Fig. 5.7 is the highest. From a climatological point of view, the 330 K isentropic surface is in summer in the mid-latitudes very close to the dynamical tropopause and is located at roughly 300 hPa (Fig. 1.3). This corresponds to a mean height of 8.5 to 9 km above sea level. Hence, the values in the presented cross sections that are located below 330 K are located in the troposphere, whereas values that are above this line belong to the stratosphere.

The first presented time step does not show remarkable differences in PVT between the ctrl simulation and the +5 K experiment (Fig. 5.15a,b). The rest of the sensitivity experiments show for the first time step differences that are even less remarkable. As shown in Fig. 5.7a, in this time step the upper level PV anomaly is located over land masses and the differences between the ctrl simulation and the +5 K experiment are very small 5.13a. There, the Mediterranean is not yet able to diabatically influence the physical mechanisms, which are important for the cyclone. Hence, an increase of the Mediterranean SSTs does not yet have an influence on up-

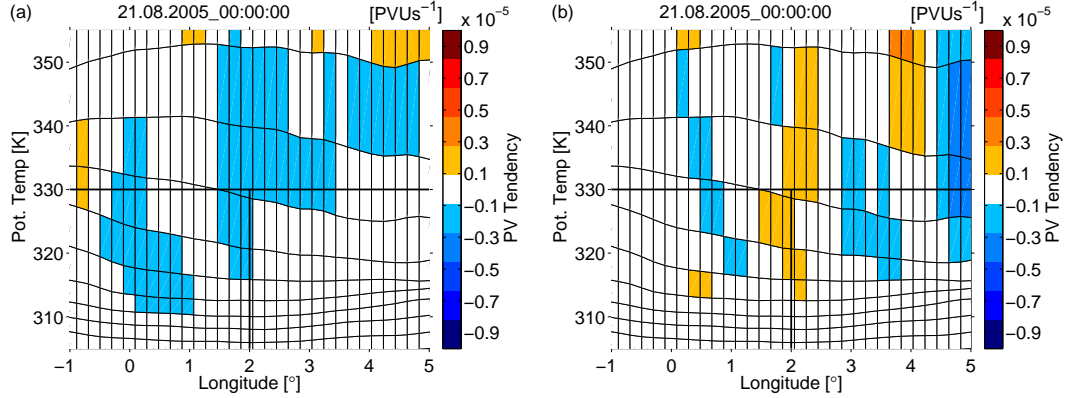


Figure 5.15: a) Cross section of PVT in the WRF ctrl simulation along the latitude of 48°N over the longitudes from -1°W to 5°E on August 21, 2005 (00 UTC). The y -axis shows vertical levels of potential temperature in Kelvin. b) Same as a) but for the difference in PVT between the $+5\text{ K}$ experiment and the ctrl simulation. The bold horizontal line indicates the 330 K isentropic surface, where the upper level PV on Fig. 5.7 are shown. The bold vertical line indicates the longitude where the upper level PV anomalies in 5.7 are most distinctive. The trend to calculate PVT is $+/ - 6$ hours relative to the displayed time steps.

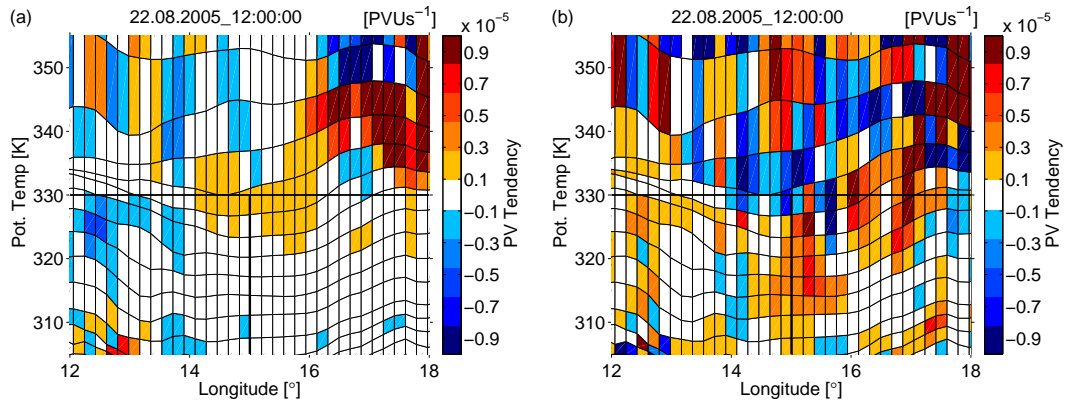


Figure 5.16: a) Cross section of PVT in the WRF ctrl simulation along the latitude of 44°N over the longitudes from 12°W to 18°E on August 22, 2005 (12 UTC). The y -axis shows vertical levels of potential temperature in Kelvin. b) Same as a) but for the difference in PVT between the $+5\text{ K}$ experiment and the ctrl simulation. The bold horizontal line indicates the 330 K isentropic surface, where the upper level PV on Fig. 5.7 are shown. The bold vertical line indicates the longitude where the upper level PV anomalies in 5.7 are most distinctive. The trend to calculate PVT is $+/ - 6$ hours relative to the displayed time steps.

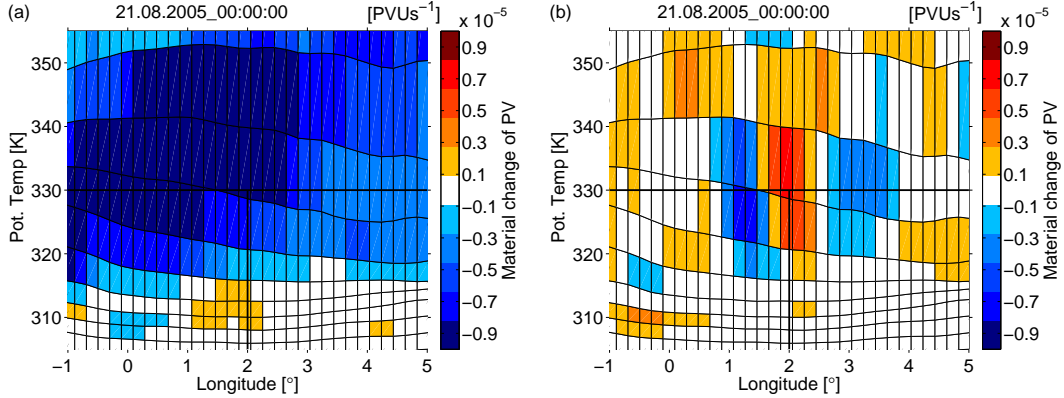


Figure 5.17: a) Cross section of $\frac{D}{Dt}PV$ due to diabatic heating in the WRF ctrl simulation along the latitude of 48°N over the longitudes from -1°W to 5°E on August 21, 2005 (00 UTC). The y -axis shows vertical levels of potential temperature in Kelvin. b) Same as a) but for the difference in $\frac{D}{Dt}PV$ due to diabatic heating between the +5 K experiment and the ctrl simulation. The bold horizontal line indicates the 330 K isentropic surface, where the upper level PV on Fig. 5.7 are shown. The bold vertical line indicates the longitude where the upper level PV anomalies in 5.7 are most distinctive. The trend to calculate $\frac{D}{Dt}PV$ due to diabatic heating is +/- 6 hours relative to the displayed time steps.

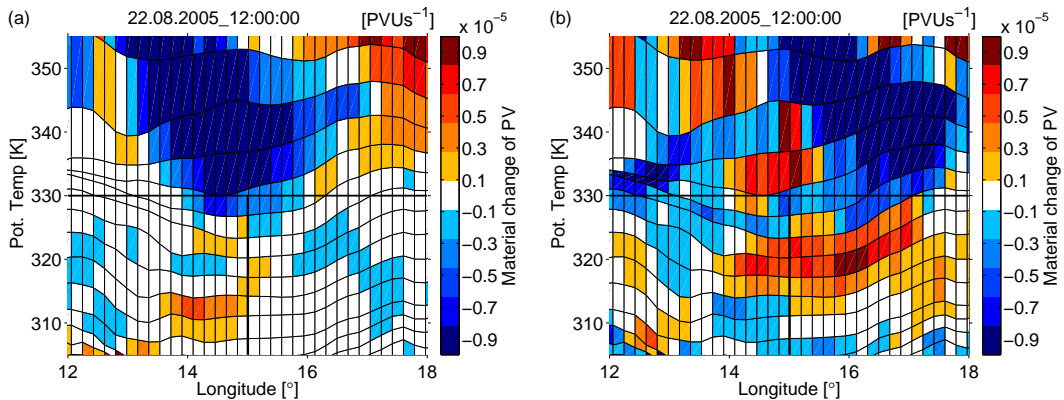


Figure 5.18: a) Cross section of $\frac{D}{Dt}PV$ due to diabatic heating in the WRF ctrl simulation along the latitude of 44°N over the longitudes from 12°W to 18°E on August 22, 2005 (12 UTC). The y -axis shows vertical levels of potential temperature in Kelvin. b) Same as a) but for the difference in $\frac{D}{Dt}PV$ due to diabatic heating between the +5 K experiment and the ctrl simulation. The bold horizontal line indicates the 330 K isentropic surface, where the upper level PV on Fig. 5.7 are shown. The bold vertical line indicates the longitude where the upper level PV anomalies in 5.7 are most distinctive. The trend to calculate $\frac{D}{Dt}PV$ due to diabatic heating is +/- 6 hours relative to the displayed time steps.

per level PV . At the same time, $\frac{D}{Dt}PV$ due to diabatic heating of the ctrl simulation shows extended negative values (Fig. 5.17a). The simulated cyclone at this time is still over land and close to the MB, and it seems that moisture fluxes due to higher SSTs are not high enough to diabatically influence the PVT . However, the differences in $\frac{D}{Dt}PV$ due to diabatic heating between the ctrl simulation and the +5 K experiment in the first time step show values between 0.5×10^{-5} PVU s $^{-1}$ and 0.8×10^{-5} PVU s $^{-1}$, and hence are a bit more pronounced (Fig. 5.17b). Thus, the 5 K increase of the Mediterranean SSTs already here exhibits a slight diabatical impact on PVT .

Considering PVT of the WRF ctrl simulation in the second time step (Fig. 5.16a), where the center of the positive PV anomaly is located over the Adriatic Sea at roughly 15°E, and already passed over the Mediterranean, slightly positive values are found along the 330 K isentropic surface, whereas below this level (mid-troposphere) no PVT is found. Comparing this with the differences in PVT between the WRF ctrl simulation and the +5 K experiment of the second time step, substantially positive values in PVT below the 330 K isenropic surface and negative values of PVT above the level of 330 K are visible (Fig. 5.16b). At the same time, there is a substantial increase between 0.7 and 1×10^{-5} PVU s $^{-1}$ in $\frac{D}{Dt}PV$ due to diabatic heating in the mid-troposphere, and a decrease between -0.1 and -0.7 around the 330 K isentropic surface at the same longitude (Fig. 5.18a,b), suggesting that there is an increase in PV due to diabatic heating in the mid-troposphere and a decrease of PV around the tropopause. Thus, cyclogenesis in the +5 K experiment slightly decreases on levels of potential temperature between 330 and 335 K, and substantially increases in the mid-troposphere due to diabatic heating from the Mediterranean, which renders the analysed Vb-type cyclone more intense (Fig. 5.10).

Since there is an intensification of the analysed Vb-type cyclone in the +5 K experiment relative to the ctrl simulation it is conceivable that precipitation values in the experiments with increased SSTs are increased as well. To check this, the accumulated precipitation as simulated by WRF in domain D4 from August 20 (00 UTC) to August 24, 2005 (00 UTC) for the WRF sensitivity experiments and the ctrl simulation are shown in Fig. 5.19. The values represent precipitation in the Swiss rain area (Fig. 3.2). There is a non-linear relationship between precipitation and Mediterranean SSTs discernable (Fig. 5.19): In the sensitivity experiments from -5 K to +2 K, no remarkable changes in precipitation are present, whereas from the +3 K to the +5 K experiment, accumulated precipitation increase constantly and substantially to the overall maximum in the +5 K experiment, where precipitation amounts to 118.2 mm. This corresponds to an increase in precipitation of approximately one third compared with the 89.42 mm that are found in the WRF ctrl simulation.

In the herein analyzed case, there is a clear relation between Vb related precipitation in Switzerland and warmer SSTs in the MB. Therefore, it is interesting to see when exactly precipitation increases in the different sensitivity experiments.

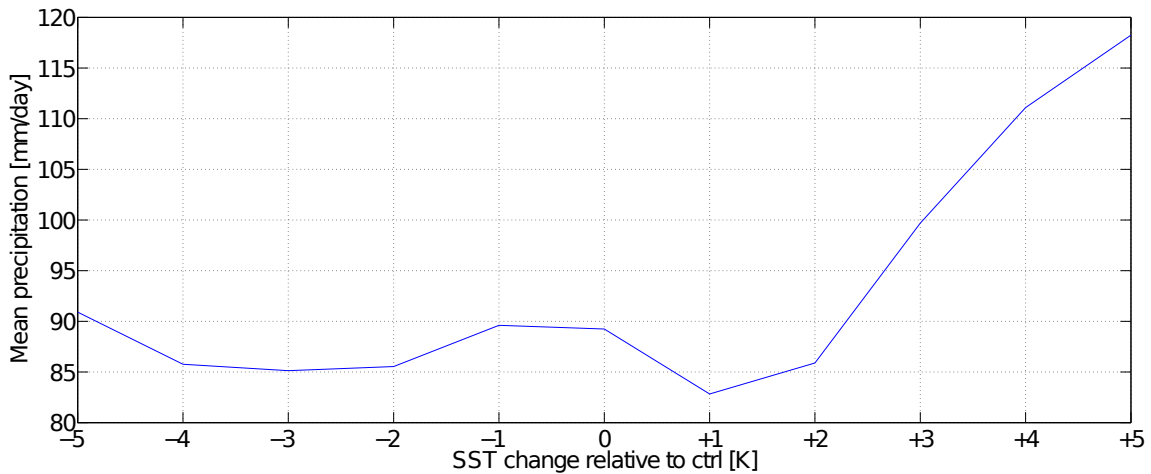


Figure 5.19: Accumulated precipitation from August 20 (00 UTC) to August 24, 2005 (00 UTC) on the domain D4 averaged over the Swiss rain area for every WRF sensitivity experiment.

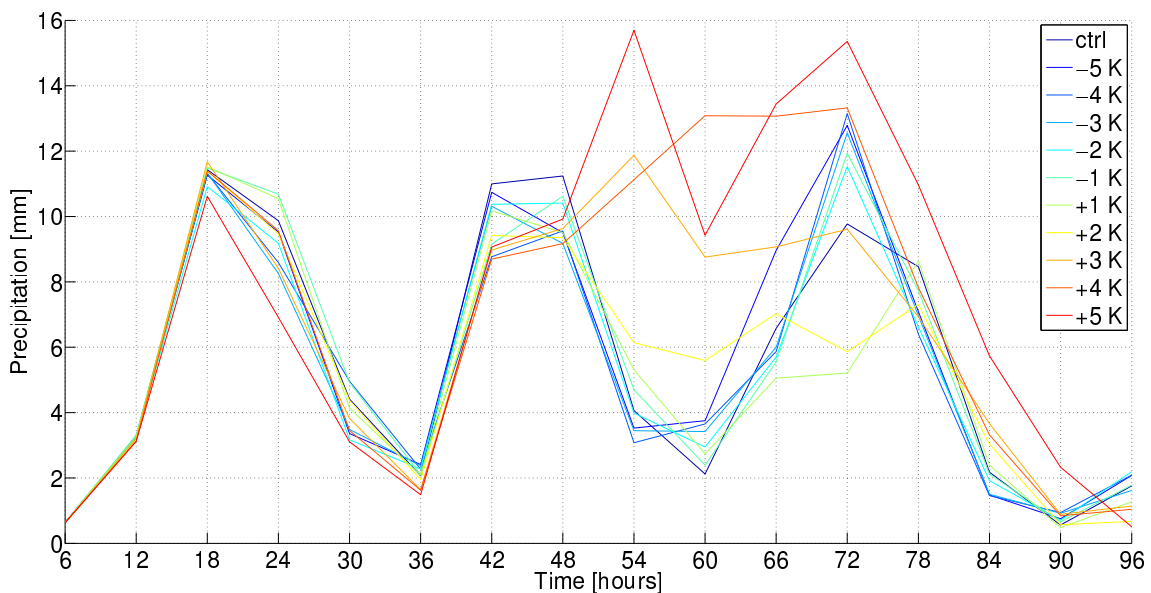


Figure 5.20: Accumulation of precipitation in the WRF sensitivity experiments including the WRF ctrl simulation in the domain D4 for every 6-hourly time step.

In this regard, the mean precipitation as simulated by WRF per time step for every sensitivity experiment is shown in Fig. 5.20. In the WRF ctrl simulation there is a pattern that exhibits three peaks with maxima after 18, 42 to 48, and 72 hours. All the sensitivity experiments with decreased SSTs relative to the ctrl simulation follow the same pattern, and hence are very similar to WRF ctrl. Regarding the sensitivity experiments with higher SSTs relative to WRF ctrl, the same pattern is present until 48 hours after the initialization. However, after the second peak between 54 and 66 hours after the initialization especially the +3 K, +4 K, and +5 K experiments deviate, and show substantial increases in precipitation. The reason for this behaviour is the trajectory of the simulated cyclone, which firstly is located over the land masses of France, where the influence of the Mediterranean in terms of moisture supply is low. Then, the low pressure system moves over the western MB, where it absorbs humidity from the underlying sea as illustrated by the moisture fluxes, which are substantially increased in the +3 K, +4 K, and +5 K experiments. Subsequently, 54-66 hours after the initialization, the simulated Vb-type cyclone moves over the Italian Peninsula. From this position the simulated Vb-type cyclone starts to transport its increased moisture content, due to counter-clock rotation, towards the northern side of the Swiss Alps, where the absorbed moisture is forced to precipitate.

5.3 Discussion

As discussed in Chapter 1, MeteoSchweiz (2006) showed that on August 20, 2005 an upper level low pressure system was observed over the Benelux Union and moved to the Mediterranean Sea, where it merged with a secondary surface low pressure system on August 21, 2005 (MeteoSchweiz, 2006). All in all, WRF is able to simulate this event. The *PV* distribution of the WRF ctrl simulation at the 330 K isentropic surface indicates that on August 20, 2005 a *PV* streamer with center over the Benelux Union stretches down until the Gulf of Genoa coming from polar regions, and covers western Europe. This exhibits cyclogenetic effects over the whole area with a maximum around the Benelux Union. Furthermore, there are already anomalously high *PV* values at the same level over the Gulf of Genoa on August 20, 2005. This contributes to cyclogenesis at surface level (Section 1.2), but might not be the only reason for the formation of the surface low pressure system. Another trigger for the formation of the surface low pressure system might be lee-cyclogenesis, where the Alps deviate surface and upper level winds such that on the lee-side of the Alps, in combination with baroclinic wave interaction, a surface low over the Gulf of Genoa forms (McGinley, 1982). At first glance, this mechanism is confirmed by the wind fields as simulated by WRF, where the jet stream is located over southern France and the Gulf of Genoa and a northerly flow is established in the mid-troposphere over the western Alps, while a southerly flow is established over the eastern Italian Peninsula. Furthermore, there is a northeasterly surface wind flowing around the western Alps.

According to Lionello et al. (2002) the SST in the Mediterranean increases until

2100 homogeneously by an average of 3.1 K. Over the Gulf of Genoa the increase in SSTs might be even a bit higher with 3.5 K (Somot et al., 2006). By comparing the WRF +3 K experiment with the WRF ctrl simulation, an increase in accumulated mean precipitation from August 20 to August 21, 2005 of about 15 mm is found. Note that the rain values of the ctrl simulation are lower than the observational data by MeteoSwiss. Nevertheless, an increase of 15 mm relative to the ctrl simulation is already remarkable and indicates that floodings such as the Vb case of August 2005 on average could potentially be more severe in 2100. However, the sensitivity experiments herein are run to analyze solely the impact of a warming Mediterranean on moisture fluxes and precipitation in Switzerland in the case of one particular Vb-type cyclone. This particular Vb-type cyclone is initialized using reanalysis data. Thus, the simulated cyclone is initially defined with specific atmospheric states in pressure, temperature, wind and other variables of atmospheric dynamics. Another possible Vb-type cyclones by the end of this century, which pass over the Mediterranean Sea, do not necessarily have to have the herein projected impact in precipitation. Every cyclone brings along different atmospheric conditions which determine in an individual dynamical interplay the Vb related sensitivity of precipitation to SSTs in the Mediterranean. Hence, the precipitation results in this study should be considered as a first indication that (1) a non-linear process governs the sensitivity of the precipitation impact of Vb-type cyclones to SSTs in the Mediterranean, and (2) the particular Vb case as it happened in August 2005 might in 2100, where according to Lionello et al. (2002) the MB is about 3 K warmer, be even more severe than it was in 2005.

As already stated above, there is a systematic bias between the values of $z700$ found in ERA-interim and the smoothed domain D4 of WRF (Fig. 5.4). It is conceivable that another set of parametrizations for the dynamical downscaling with WRF produces a cyclone that exhibits lower values in $z700$. Nevertheless, there are other arguments that might explain why a constant offset between the data in WRF and the data in ERA-interim is present. The WRF output in Fig. 5.1 is compared with ERA-interim data, which has a spatial resolution of 1.5° . On the other hand, the model run with WRF is driven with the NCEP/NCAR reanalysis data set, which has a spatial resolution of 2.5° . Thereby, comparing the cyclone trajectory identified in WRF, which has a spatial resolution of 4 km, with a reanalysis data set that has a resolution of 1.5° has two reasons: (1) It is expected to yield an assessment that is more accurate than a comparison with a reanalysis data set that has a spatial resolution of 2.5° . (2) The use of ERA-interim with a spatial resolution of 1.5° is in consistency with the herein presented Vb climatology (Chapter 4). Since ERA-interim has a resolution of 1.5° , it is conceivable that the considered cyclone at the first time step of the simulation is deeper in ERA-interim than in NCEP/NCAR. This is confirmed by a comparison of the snapshots in Figs. 5.11a and 5.11c. Thereby, the core of the low pressure system in Fig. 5.11a is slightly less deep than the core of the low pressure system in Fig. 5.11c. In this respect, the snapshot in Fig. 5.11a corresponds to the data as it is provided by the NCEP/NCAR reanalysis for the initialization of the dynamical downscaling with WRF. Hence, in

the evaluation of the trajectory and the intensity WRF starts from higher values of $z700$ than ERA-interim. However, a comparison of the two solid lines in Fig. 5.4 shows that the deepening rate and the temporal behavior of the life cycle of minima in $z700$ tracked in ERA-interim using the tracking algorithm by Blender et al. (1997), and the same life cycle in the domain D4 identified in WRF using a cyclone detection algorithm written in MATLAB (Appendix A), are close to each other and similar. This allows to use the cyclone as simulated by WRF to investigate the sensitivity of Vb related precipitation to SSTs in the MB.

The intensification of the analysed Vb-type cyclone with increased SSTs in the Mediterranean agree with the results by Lionello et al. (2002), where cyclones in the MB are projected to become more intense due to a reinforcement of diabatic processes such as latent heating. It has to be noted that diabatic heating is not only caused by latent heating due to condensation but also by radiative processes, and thermal conduction across the earth surface (Wernli and Croci-Maspoli, 2013). However, since in the sensitivity experiments with WRF everything is kept constant except for the SSTs in the Mediterranean, only the increased latent heat fluxes that arise from higher SSTs can be responsible for the increased diabatic heating in the mid-troposphere.

Chapter 6

Conclusion

The scope of this study was twofold: On the one hand, a climatology of Vb-type cyclones is presented to evaluate main characteristics in terms of their frequency, spatial distribution, intensity, duration, and impact on precipitation. On the other hand, the regional model WRF is used to investigate the impacts of uniform changes of the Mediterranean SSTs on precipitation in Switzerland. These experiments are based on the case of the Vb-type cyclone that caused substantial flooding in Switzerland in August, 2005.

In the herein presented Vb climatology the trajectories of Vb-type cyclones are identified on geopotential height at 700 hPa ($z700$). Thereby, the results suggest an occurrence of 89 Vb-type cyclones in the period from 1979-2009, which is equal to a mean occurrence of 2.97 events per year. Furthermore, this corresponds to roughly a sixth of all the low pressure systems that on average pass over central Europe in one year. Approximately a third of the identified Vb-type cyclones occurred in spring, which is the season where a Vb-type cyclone is most likely to occur. A secondary maximum is in fall, where about a fourth of the identified Vb-type cyclones are found. From 1979 to 2009 there is no trend in Vb-type cyclones per year discernable. Furthermore, the mean length of a Vb-type cyclone is 58 hours, with a standard deviation of 31.2 hours. Roughly one fifth of the 89 identified Vb-type cyclones from 1979 to 2009 contribute to extreme precipitation events (99th percentile) in an area that covers Switzerland, southern Germany, and Austria. Furthermore, the mean value of all the precipitation anomalies in Switzerland, southern Germany, and Austria from 1979 to 2009 is significantly lower than the mean value of precipitation in the same area and time period of all the precipitation anomalies that are related to Vb-type cyclones. Overall, Vb-type cyclones are rare events, which, when they occur, play a significant role for precipitation in Switzerland, southern Germany, and Austria.

For the case of the Vb-type cyclone that occurred in August, 2005 the regional model WRF is able to reproduce the temporal evolution and the trajectory of $z700$, as it is present in ERA-interim. The same can be said for PV along the 330 K isentropic surface, and for upward moisture and latent heat fluxes at the surface.

Furthermore, the accumulated mean value of precipitation from August 20 (00 UTC) to August 24, 2005 (00 UTC) in northern Switzerland as simulated by the WRF ctrl simulation is not significantly different from the observations in the same area and time provided by the Federal Office of Meteorology and Climatology, MeteoSwiss.

Increased SSTs in the Mediterranean, together with cyclonic activity cause upward latent heat and moisture fluxes at the Mediterranean Sea surface to rise. In the case of the Vb-type cyclone that occurred in August, 2005 the increased latent heat fluxes exhibit cyclogenetic effects through diabatic heating in the middle of the troposphere, and cause the cyclone to become more intense. This is in agreement with other studies that project an increased intensity of Mediterranean cyclones due to diabatic heating for the end of the 21th century (Lionello et al. (2002), Somot et al. (2006), IPCC (2012), IPCC (2013)).

The WRF sensitivity experiments show a non-linear relation between SST changes in the Mediterranean and Vb related precipitation in Switzerland. In this respect, SSTs in the Mediterranean that are increased by 2 K and beyond relative to the SST of August 20, 2005 cause the accumulated mean precipitation from August 20 (00 UTC) to August 24, 2005 (00 UTC) in Switzerland to increase substantially from 86 mm to more than 115 mm in the +5 K experiment (Fig. 5.19). Projections of Mediterranean SSTs estimate a uniform mean increase of about 3 K until 2100 (Lionello et al., 2002). Hence, the Vb-type cyclone that occurred in August 2005 and caused substantial flooding in Switzerland might be even more intense and could potentially cause more damage in the context of higher Mediterranean SSTs as projected for the end of the 21th century.

Chapter 7

Outlook

The precipitation analysis in this study was performed using rain anomalies to see the impact of daily Vb related precipitation in Switzerland, southern Germany, and Austria throughout the year from a climatological point of view. However, it would be interesting as well to see the role of Vb-type cyclones in terms of flooding events in these countries during the 20th century. Therefore, a task would be to identify all the flooding events that occurred during the 20th century in the aforementioned countries to see the ratio of the Vb-type cyclones that are involved.

The simulations with WRF are designed with a specific set of parametrizations and temporal as well as spatial resolutions. Herein, it was not feasible to perform several sets of simulations with different parametrizations and domain setups, which might have an impact on WRF output fields such as $z700$, PV , and precipitation. Although the set of parametrizations employed here led to satisfactory results, it is conceivable that another set of parametrizations could perform even better for this case study. In particular, the mean value of accumulated precipitation for the simulated time period could potentially be improved by using different schemes that are concerned with the simulation of rain. Furthermore, also the implications of spatial resolutions that are higher than the 4 km of the herein used domain D4 to the aforementioned output fields has to be investigated.

Herein, an increase of Mediterranean SSTs caused the Vb-type cyclone to become more intense, which led to an increase in precipitation in Switzerland. To substantiate whether changes in Mediterranean SSTs are in general a reason for intensification of Vb-type cyclones, it would be necessary to perform the herein presented sensitivity experiments with different Vb-type cyclones.

Appendix A

Programs and Scripts

A.1 Detection of z700 minima in WRF output

```
1 close all
2 clear all
3
4 %% This section is for the WRF sens. experiments and ctrl
   simulation
5
6 figure(1);
7 hold on
8 geoshow('cntry02.shp','FaceColor',[0.95 0.95 0.95]);
9 axis([-5 25 37 55]);
10
11 [z lon lat height] = ...
12 getnetCDFvar0('/alphadata03/kummlie/no_backup/WRF_0/
    GHT_700_6_hourly_0_d4_COARSE-d4.nc','zg','lon','lat','orog');
13
14 z1000 = squeeze(z);
15 clear z
16 [dim_x,dim_y,dim_t] = size(z1000);
17
18 for tt = 1:dim_t
19   for xx = 1:dim_x
20     for yy = 1:dim_y
21       if height(xx,yy,tt) < 200
22         x(xx,yy,tt) = z1000(xx,yy,tt);
23       else
24         x(xx,yy,tt) = NaN;
25       end
26     end
27   end
28 end
29
30 clear z1000
31
32 % Here we calculate the gradients around a point in the field.
33 for tt = 1:dim_t
34   for xx = 11:dim_x-11
```

```

35     for yy = 11:dim_y-11
36         if (lon(xx,yy) > 0) && (lon(xx,yy) < 20) && ...
37             (lat(xx,yy) > 40) && (lat(xx,yy) < 52)
38             grad_ax(xx,yy,tt) = mean(x(xx+10,yy,tt)) - x(xx,yy,tt) /
39                 (40000);
40             grad_bx(xx,yy,tt) = mean(x(xx-10,yy,tt)) - x(xx,yy,tt) /
41                 (40000);
42             grad_ay(xx,yy,tt) = mean(x(xx,yy+10,tt)) - x(xx,yy,tt) /
43                 (40000);
44             grad_by(xx,yy,tt) = mean(x(xx,yy-10,tt)) - x(xx,yy,tt) /
45                 (40000);
46             x_d(xx,yy,tt) = x(xx,yy,tt);
47         else
48             grad_ax(xx,yy,tt) = NaN;
49             grad_bx(xx,yy,tt) = NaN;
50             grad_ay(xx,yy,tt) = NaN;
51             grad_by(xx,yy,tt) = NaN;
52             x_d(xx,yy,tt) = NaN;
53         end
54     end
55 end
56 clear x
57
58 for tt = 1:dim_t
59     for xx = 1:dim_x-12
60         for yy = 1:dim_y-12
61             if (grad_ax(xx,yy,tt) > 0) && (grad_bx(xx,yy,tt) > 0) && ...
62                 (grad_ay(xx,yy,tt) > 0) && (grad_by(xx,yy,tt) > 0)
63                 x_d4(xx,yy,tt) = x_d(xx,yy,tt);
64             else
65                 x_d4(xx,yy,tt) = NaN;
66             end
67         end
68     end
69 clear x_d
70 roh = 0;
71
72 while roh == 0
73
74 val_min_1 = squeeze(min(min(x_d4,[],1),[],2));
75
76 for t = 1:dim_t
77     [pos_min_x_1(t) pos_min_y_1(t)] = find(x_d4(:,:,t)==val_min_1(t));
78 end
79
80 for t = 1:dim_t-1
81     if lon(pos_min_x_1(t),pos_min_y_1(t)) > ...
82         lon(pos_min_x_1(t+1),pos_min_y_1(t+1))
83         val_min_1(t) = NaN;
84     end

```

```
85 end
86
87 for t = 1:dim_t
88     if val_min_1(t) == NaN
89         roh = 0;
90         break
91     else
92         roh = 1;
93     end
94 end
95 end
96 end
```


Appendix B

Namelists

B.1 namelist.wps

```
1 &share
2   wrf_core = 'ARW',
3   max_dom = 4,
4   start_date = '2005-08-20_00:00:00', '2005-08-20_00
:00:00', '2005-08-20_00:00:00',
5           '2005-08-20_00:00:00', '2005-08-20_00:00:00',
6   end_date   = '2005-08-24_00:00:00', '2005-08-24_00
:00:00', '2005-08-24_00:00:00',
7           '2005-08-24_00:00:00', '2005-08-24_00:00:00',
8   interval_seconds = 21600
9   io_form_geogrid = 2,
10 /
11
12 &geogrid
13   parent_id      = 1,    1,    2,    3,    4,
14   parent_grid_ratio = 1,    3,    3,    3,    3,
15   i_parent_start  = 1,   12,   25,   50,   40,
16   j_parent_start  = 1,   12,   25,   50,   40,
17   e_we            = 81,  166,  355,  721,  1000,
18   e_sn            = 81,  166,  355,  721,  1000,
19   geog_data_res   = '20m', '10m', '5m', '2m', '30s',
20   dx = 108000,
21   dy = 108000,
22   map_proj = 'lambert',
23   ref_lat  = 46.6,
24   ref_lon   = 14,
25   truelat1 = 80.0,
26   truelat2 = 10.0,
27   stand_lon = 14,
28   geog_data_path = '/home/ubelix/sm/ck08p414/DATA/topography/geog'
29 /
30
31 &ungrib
32   out_format = 'WPS',
33   prefix = 'PGB',
34 /
```

```

35
36 &metgrid
37   fg_name = 'PGB', 'GRB2D'
38   io_form_metgrid = 2,
39 /

```

B.2 namelist.input

```

1  &time_control
2    run_days                  = 4,
3    run_hours                 = 0,
4    run_minutes                = 0,
5    run_seconds                = 0,
6    start_year                = 2005, 2005, 2005, 2005,
7      2005,
8    start_month               = 08, 08, 08, 08, 08,
9    start_day                 = 20, 20, 20, 20, 20,
10   start_hour                = 00, 00, 00, 00, 00,
11   start_minute              = 00, 00, 00, 00, 00,
12   start_second              = 00, 00, 00, 00, 00,
13   end_year                  = 2005, 2005, 2005, 2005,
14     2005,
15   end_month                 = 08, 08, 08, 08, 08,
16   end_day                   = 24, 24, 24, 24, 24,
17   end_hour                  = 00, 00, 00, 00, 00,
18   end_minute                = 00, 00, 00, 00, 00,
19   end_second                = 00, 00, 00, 00, 00,
20   interval_seconds          = 21600
21   input_from_file           = .true., .true., .true., .true.,
22     ., .true.,
23   history_interval           = 60, 60, 60, 60, 60,
24   frames_per_outfile         = 1000, 1000, 1000, 1000,
25     1000,
26   restart                    = .false.,
27   restart_interval            = 360,
28   io_form_history             = 2
29   io_form_restart              = 2
30   io_form_input                = 2
31   io_form_boundary              = 2
32   debug_level                 = 0
33 /
34
35 &domains
36   time_step                  = 180,
37   time_step_fract_num          = 0,
38   time_step_fract_den          = 1,
39   max_dom                     = 4,
40   e_we                        = 81, 166, 355, 721, 1000,
41   e_sn                        = 81, 166, 355, 721, 1000,
42   e_vert                       = 36, 36, 36, 36, 36,
43   p_top_requested              = 2000,
44   num_metgrid_levels            = 18,
45   num_metgrid_soil_levels        = 2,
46   dx                           = 108000, 36000, 12000,

```

```

        4000, 1333.33,
43 dy                               = 108000, 36000, 12000,
        4000, 1333.33,
44 grid_id                          = 1,      2,      3,      4,
        5,
45 parent_id                         = 0,      1,      2,      3,
        4,
46 i_parent_start                   = 1,      12,     25,     50,
        40,
47 j_parent_start                   = 1,      12,     25,     50,
        40,
48 parent_grid_ratio                = 1,      3,      3,      3,
        3,
49 parent_time_step_ratio           = 1,      3,      3,      3,
        3,
50 feedback                          = 1,
51 smooth_option                     = 0,
52 /
53
54 &physics
55 mp_physics                        = 8,      8,      8,      8,
        8,
56 ra_lw_physics                    = 4,      4,      4,      4,
        4,
57 ra_sw_physics                    = 1,      1,      1,      1,
        1,
58 radt                             = 3,      3,      3,      3,
        3,
59 sf_sfclay_physics                = 1,      1,      1,      1,
        1,
60 sf_surface_physics               = 1,      1,      1,      1,
        1,
61 bl_pbl_physics                   = 1,      1,      1,      1,
        1,
62 bldt                            = 0,      0,      0,      0,
        0,
63 cu_physics                        = 1,      1,      1,      1,
        1,
64 cudt                            = 5,      5,      5,      5,
        5,
65 isfflx                           = 1,
66 /
67
68 &fdda
69 /
70
71 &dynamics
72 w_damping                         = 1,
73 diff_opt                          = 1,
74 km_opt                           = 4,
75 diff_6th_opt                     = 0,      0,      0,      0,
        0,
76 diff_6th_factor                  = 0.12,   0.12,   0.12,
        0.12,
77 base_temp                         = 297.

```

```
78  damp_opt                  = 0,
79  zdamp                     = 5000.,   5000.,   5000.,
80    5000.,   5000.,
80  dampcoef                  = 0.2,     0.2,     0.2,     0.2,
81    0,2,
81  khdif                     = 0,       0,       0,       0,
82    0,
82  kvdif                     = 0,       0,       0,       0,
82    0,
83  non_hydrostatic           = .true.,  .true.,  .true., .
83    true.,  true.,
84  moist_adv_opt             = 1,       1,       1,       1,
84    1,
85  scalar_adv_opt            = 1,       1,       1,       1,
85    1,
86 /
87
88 &bdy_control
89  spec_bdy_width            = 5,
90  spec_zone                 = 1,
91  relax_zone                = 4,
92  specified                 = .true.,  .false., .false., .
92    false.,  false.,
93  nested                    = .false.,  .true.,  .true., .
93    true.,  true.,
94 /
95
96 &grib2
97 /
98
99 &namelist_quilt
100 nio_tasks_per_group = 0,
101 nio_groups = 1,
102 /
```

List of Figures

1.1	The green lines show all cyclone tracks named by W. J. van Bebber. The darker green line represents the Vb trajectory. Source: M. Messmer, personal communication, based on van Bebber (1891).	4
1.2	Observational distribution of precipitation in mm accumulated between August 20 and August 22, 2005 in Switzerland. Source: Frei (2005).	6
1.3	Zonal-mean climatological distribution of potential temperature (dashed contours) and PV (solid contours for 1,2, 4, and 7 PVU) in the northern hemisphere winter (left) and summer (right). The 2 PVU contour, indicating the dynamical tropopause, and the 310, 330, and 350 K isentrope are indicated by bold lines. Figure from Wernli and Croci-Maspoli (2013).	8
2.1	Schematic representation of vertical η -levels between 0 and 1. Figure from Kilic (2012).	14
2.2	Arakawa-C grid: Horizontal grid comprised of a parent domain and an embedded nest domain with a 3:1 grid size ratio. Figure from Skamarock et al. (2008).	15
2.3	Flowchart of WPS components, their input sources, and interactions.	21
2.4	Four nested domains (D1, D2, D3, D4) for the model simulations with WRF. To illustrate the horizontal resolution the orography is shown.	23
2.5	Height of vertical η -levels over the Adriatic Sea at 15°E and 43.5°N.	24
2.6	Pressure of vertical η -levels over the Adriatic Sea at 15°E and 43.5°N.	25
2.7	SST distribution in Kelvin for the domain D3 of the ctrl simulation on August 20, 2005 (00 UTC).	26
3.1	Target area used for the analysis of precipitation caused by Vb-type cyclones in Switzerland, southern Germany, and Austria.	28
3.2	Target area for precipitation in Switzerland. Figure from MeteoSwiss.	30
3.3	Tracking boxes used for the identification of Vb-type cyclones.	32

4.1	Vb tracks detected in ERA-interim from 1979 to 2009. Blue rectangles show the Vb-boxes 1 and 2, which are used to identify Vb-type cyclones. The mean Vb trajectory is shown in green and the Vb-type cyclone that is used for the sensitivity experiments with WRF is emphasized in red. The black crosses indicate grid points where $z700$ exceeds the 5th percentile of a particular cyclone. The purple crosses indicate grid points where the gradient of $z700$ is above the 95th percentile of a particular cyclone and the green dots indicate grid points where both of the aforementioned percentiles are exceeded and exceeded, respectively.	36
4.2	a) Life cycles of the differences between minimum $z700$ in a time step of a particular cyclone and the mean $z700$ of this particular cyclone for all the Vb-type cyclones in Fig. 4.1 (blue lines). The red line represents the mean of the blue lines. The black lines show the standard deviation around the mean. The time axis shows the relative life time of the Vb-type cyclones. b) Same as a) but for $z700$ gradient.	38
4.3	a) Number of Vb-type cyclones per year in the period 1979-2009; b) corresponding relative distribution of Vb-type cyclones of the entire period.	39
4.4	a) Number of Vb related 6-hourly intervals per year in the period 1979-2009. b) corresponding relative distribution of these 6-hourly intervals of the entire period.	40
4.5	Histogram showing the length of all the Vb-type cyclones between 1979 and 2009 in hours starting at the first time step, where a cyclone enters the first Vb-box 1.	41
4.6	Annual cycle of precipitation for the European rain area (Fig. 3.1). The mean values of daily precipitation for each month are shown in mm/day.	41
4.7	Time series of rain anomalies from 1979-2009 in the ERA-interim data set in the European rain area averaged over Switzerland, southern Germany, and Austria (Fig. 3.1). The blue dots indicate precipitation anomalies. Black crosses highlight all the rain anomalies that occur during Vb situations. The maximum rain days per Vb-type cyclone are colored in red. The horizontal black lines indicates the 95th and 99th percentiles. Furthermore, the Vb related rain days that belong to the Vb-type cyclone which occurred in August, 2005 are shown with bold crosses.	42
4.8	a) Histogram of rain anomalies after removing the annual cycle in the European rain area. b) As a) but only for Vb related days (black and red crosses in Fig. 4.7.)	43

5.1	<i>z</i> 700 fields for 4 time steps and different data sets. The columns from left to right show: a) The WRF ctrl simulation in the domain D4, b) the smoothed domain D4 as simulated by the WRF ctrl simulation, c) ERA-interim, d) the differences between ERA-interim and WRF D4 smoothed. The time steps are shown in 1) to 4), starting with the first time step simulated by WRF, and the following two separated by 24 hours, whereas the last shown time step is on August 23, 2005 (12 UTC). Furthermore, the particular locations of the minima of <i>z</i> 700 in WRF are indicated with “+”-symbols, whereas the particular locations of the minima of <i>z</i> 700 in ERA-interim are indicated with “×”-symbols.	48
5.2	Mean differences of <i>z</i> 700 between ERA-interim and the smoothed domain D4 of WRF. The ERA-interim data was interpolated to the grid of the WRF domain D4 to calculate the mean values for every grid point over all the time steps.	49
5.3	Tracks identified in the WRF ctrl simulation in the smoothed domain D4 and in ERA-interim. The WRF track is shown in black and the ERA-interim track is shown in red. The points indicate the cyclone centers, i.e., the minima in <i>z</i> 700. All the time steps that coincide with each other are marked. Furthermore, the time steps 1, 4, 8, and 10 correspond to the time steps shown in Fig. 5.1.	50
5.4	Life cycles of <i>z</i> 700 minima on the different trajectories of Fig. 5.3. The smoothed WRF ctrl output of the domain D4 is represented by the solid black line, whereas the ERA-interim output is represented by the solid red line. The dashed lines show the life cycles of <i>z</i> 700 minima in WRF on the track where the identified ERA-interim minima are located (black dashed), and of ERA-interim where the identified WRF minima are located (red dashed).	51
5.5	a) Upward moisture fluxes over central Europe and the western Mediterranean of WRF ctrl 24 hours after the initialization. b) same as a) in ERA-interim. c) Same as a) 60 hours after the initialization. d) Same as a) in ERA-interim 60 hours after the initialization.	54
5.6	a) Upward latent heat fluxes over central Europe and the western Mediterranean of WRF ctrl 24 hours after the initialization. b) Same as a) in ERA-interim. c) Same as a) 60 hours after the initialization. d) Same as a) in ERA-interim 60 hours after the initialization.	55
5.7	a) PV at the 330 K isentropic surface of WRF ctrl in the domain D4 24 hours after the initialization. b) Same as a) in ERA-interim. c) Same as a) 60 hours after the initialization. d) Same as a) in ERA-interim 60 hours after the initialization.	56
5.8	Distribution of accumulated precipitation in WRF ctrl in the domain D4 from August 20 (00 UTC) to August 24, 2005 (00 UTC) in Switzerland.	57
5.9	Trajectories of <i>z</i> 700 minima of the WRF sensitivity experiments and the WRF ctrl simulation. The ctrl simulation is shown in black.	59

5.10	Life cycles of $z700$ minima of the WRF sensitivity experiments and the WRF ctrl simulation. The ctrl simulation is shown in black.	60
5.11	Difference in upward moisture fluxes between the +5 K experiment and the WRF ctrl simulation for a) 24 hours after the initialization and b) 60 hours after the initialization.	60
5.12	Difference in upward latent heat fluxes between the +5 K experiment and the WRF ctrl simulation for a) 24 hours after the initialization and b) 60 hours after the initialization.	61
5.13	Difference in PV between the +5 K experiment and the WRF ctrl simulation for a) 24 hours after the initialization and b) 60 hours after the initialization.	62
5.14	Life cycles of PV maxima along the 330 K isentropic surface in the WRF sensitivity experiments and the ctrl simulation. The ctrl simulation is shown in black.	63
5.15	a) Cross section of PVT in the WRF ctrl simulation along the latitude of 48°N over the longitudes from -1°W to 5°E on August 21, 2005 (00 UTC). The y -axis shows vertical levels of potential temperature in Kelvin. b) Same as a) but for the difference in PVT between the +5 K experiment and the ctrl simulation. The bold horizontal line indicates the 330 K isentropic surface, where the upper level PV on Fig, 5.7 are shown. The bold vertical line indicates the longitude where the upper level PV anomalies in 5.7 are most distinctive. The trend to calculate PVT is +/- 6 hours relative to the displayed time steps.	64
5.16	a) Cross section of PVT in the WRF ctrl simulation along the latitude of 44°N over the longitudes from 12°W to 18°E on August 22, 2005 (12 UTC). The y -axis shows vertical levels of potential temperature in Kelvin. b) Same as a) but for the difference in PVT between the +5 K experiment and the ctrl simulation. The bold horizontal line indicates the 330 K isentropic surface, where the upper level PV on Fig, 5.7 are shown. The bold vertical line indicates the longitude where the upper level PV anomalies in 5.7 are most distinctive. The trend to calculate PVT is +/- 6 hours relative to the displayed time steps.	64
5.17	a) Cross section of $\frac{D}{Dt}PV$ due to diabatic heating in the WRF ctrl simulation along the latitude of 48°N over the longitudes from -1°W to 5°E on August 21, 2005 (00 UTC). The y -axis shows vertical levels of potential temperature in Kelvin. b) Same as a) but for the difference in $\frac{D}{Dt}PV$ due to diabatic heating between the +5 K experiment and the ctrl simulation. The bold horizontal line indicates the 330 K isentropic surface, where the upper level PV on Fig, 5.7 are shown. The bold vertical line indicates the longitude where the upper level PV anomalies in 5.7 are most distinctive. The trend to calculate $\frac{D}{Dt}PV$ due to diabatic heating is +/- 6 hours relative to the displayed time steps.	65

- 5.18 a) Cross section of $\frac{D}{Dt}PV$ due to diabatic heating in the WRF ctrl simulation along the latitude of 44°N over the longitudes from 12°W to 18°E on August 22, 2005 (12 UTC). The y -axis shows vertical levels of potential temperature in Kelvin. b) Same as a) but for the difference in $\frac{D}{Dt}PV$ due to diabatic heating between the +5 K experiment and the ctrl simulation. The bold horizontal line indicates the 330 K isentropic surface, where the upper level PV on Fig. 5.7 are shown. The bold vertical line indicates the longitude where the upper level PV anomalies in 5.7 are most distinctive. The trend to calculate $\frac{D}{Dt}PV$ due to diabatic heating is +/- 6 hours relative to the displayed time steps. 65
- 5.19 Accumulated precipitation from August 20 (00 UTC) to August 24, 2005 (00 UTC) on the domain D4 averaged over the Swiss rain area for every WRF sensitivity experiment. 67
- 5.20 Accumulation of precipitation in the WRF sensitivity experiments including the WRF ctrl simulation in the domain D4 for every 6-hourly time step. 67

List of Tables

2.1 Spatial resolutions and time steps of the four domains that are used for the simulations with WRF.	25
---	----

Bibliography

- Bechtold, P., E. Bazile, F. Guichard, P. Mascart, and E. Richard, 2001: A mass-flux convection scheme for regional and global models. *Q. J. R. Meteorol. Soc.*, **127**, 869–886.
- Berrisford, P., D. Dee, K. Fielding, M. Fuentes, P. Kallberg, S. Kobayashi, and S. Uppala, 2009: The ERA-Interim archive. Tech. rep., ECMWF, Shinfield Park, Reading, Uk. 16 pp.
- Bezzola, G. R., C. Hegg, and A. Koschni, 2008: Hochwasser 2005 in der Schweiz. *Synthesebericht zur Ereignisanalyse*, 24 pp.
- Blender, R., K. Frädrich, and F. Lunkeit, 1997: Identification of cyclone-track regimes in the North Atlantic. *Quart. Roy. Meteor. Soc.*, **123**, 727–741.
- Blender, R. and M. Schubert, 2000: Cyclone tracking in different spatial and temporal resolutions. *Amer. Meteor. Soc.*, **128**, 377–384.
- Campa, J. and H. Wernli, 2012: A PV perspective on the vertical structure of the mature midlatitude cyclones in the Northern Hemisphere. *Amer. Meteor. Soc.*, **69**, 725–740.
- Dee, D. P., et al., 2011: The ERA-Interim reanalysis: Configuration and performance of the data assimilation system. *Quart. Roy. Meteor. Soc.*, **137**, 553–597.
- Donner, L., 1993: A cumulus parametrization including mass fluxes, vertical momentum dynamics, and mesoscale effects. *J. Atmos. Sci.*, **50**, 889–906.
- Dudhia, J., 1989: Numerical study of convection observed during the winter monsoon experiment using a mesoscale two-dimensional model. *J. Atmos. Sci.*, **46**, 3077–3107.
- Frei, C., 2005: August-Hochwasser 2005: Analyse der Niederschlagsverteilung. Tech. rep., MeteoSchweiz. 5 pp.
- Graefe, H. and Hegg, 2004: Ereignisanalyse Hochwasser August 2002 in den Osterzgebirgsflüssen. Tech. rep., Sächsisches Landesamt für Umwelt und Geologie. 176 pp.

- Grell, G. A., J. Dudhia, and D. R. Stauffer, 1994: A description of the fifth generation Penn State/NCAR mesoscale model (MM5). Tech. rep., National Centre for Atmospheric Research, Boulder, Colorado, USA. doi:10.5065/D60Z716B.
- Grünewald, U., et al., 2004: Hochwasservorsorge in Deutschland - Lernen aus der Katastrophe 2002 im Elbegebiet. Tech. rep., Deutsches Komitee für Katastrophenvorsorge e. V. (DKKV). 152 pp.
- Hall, W., R. Rasmussen, and G. Thompson, 2005: The New Thomson microphysical scheme in WRF. *WRF/MM5 users workshop - June 2005*, 7 pp.
- Hofstaetter, M. and B. Chimani, 2012: Van Bebber's cyclone tracks at 700 hPa in the Eastern Alps for 1961-2002 and their comparison to circulation type classification. *Meteor. Zeitschr.*, **21**, 459–473.
- Holton, J. R., 1992: *An introduction to dynamic meteorology*. Academic Press Inc., 536 pp.
- Hong, S.-Y. and K. S-W, 2007: Stable boundary layer mixing in a vertical diffusion scheme. Tech. rep., Department of atmospheric sciences, Yonsei University, Seoul, Korea and NOAA/ESRL, Boulder, Colorado, USA. 120-749.
- Hoskins, B., M. McIntyre, and A. Robertson, 1985: On the use and significance of isentropic potential vorticity maps. *Quart. Roy. Meteor. Soc.*, **111**, 877–946.
- IPCC, 2007: Climate change 2007: The physical science basis - IPCC working group 1 contribution to AR4. Tech. rep., Intergovernmental Panel on Climate Change, Cambridge, United Kingdom and New York, NY, USA. 996 pp.
- IPCC, 2012: Managing the Risks of Extreme Events and Disasters to Advance Climate Change Adaptation. A Special Report of Working Groups I and II of the Intergovernmental Panel on Climate Change [Field, C.B., V. Barros, T.F. Stocker, D. Qin, D.J. Dokken, K.L. Ebi, M.D. Mastrandrea, K.J. Mach, G.-K. Plattner, S.K. Allen, M. Tignor, and P.M. Midgley (eds.)]. Tech. rep., Cambridge University Press, Cambridge, UK, and New York, NY, USA. 582 pp.
- IPCC, 2013: Climate change 2013: The physical science basis - IPCC working group 1 contribution to AR5. Tech. rep., Intergovernmental Panel on Climate Change, Cambridge, United Kingdom and New York, NY, USA. 1536 pp.
- Kain, S., 2004: The Kain-Fritsch convective parametrization: An update. *Appl. Meteor.*, **43**, 170–181.
- Kalnay, E., et al., 1996: The NCEP/NCAR 40-Year reanalysis project. *Bull. Amer. Meteor. Soc.*, **77**, 437–471.
- Kilic, C., 2012: Sensitivity of hurricane intensity and trajectories using the regional model WRF. *Master thesis at the institute for climate and environmental physics, University of Bern*, 85 pp.

- Kistler, R., et al., 2001: The NCEP-NCAR 50-year reanalysis: Monthly means cd-rom and documentation. *Bull. of the Amer. Meteor. Soc.*, **82**, 247–268.
- Koeppen, W., 1881: Die Zugstrassen der barometrischen Minima in Europa und auf den nordatlantischen Ocean und ihr Einfluss auf Wind und Wetter bei uns. *Mittlgn. d. geogr. Gesellschaft in Hamburg*, **Bd. 4**, 76–97.
- Lionello, P., F. Dalan, and E. Elvini, 2002: Cyclones in the Mediterranean region: The present and the doubled CO₂ climate scenarios. *Clim. Res.*, **22**, 147–159.
- Lionello, P. and F. Giorgi, 2007: Winter precipitation and cyclones in the Mediterranean region: Future climate scenarios in a regional simulation. *Adv. Geosci.*, **12**, 153–158.
- Lionello, P., et al., 2006: *Mediterranean Climate Variability*. Elsevier, 413 pp.
- Martin, J. E., 2006: *Mid-Latitude Atmospheric Dynamics*. John Wiley and Sons, Ltd, 324 pp.
- McGinley, J., 1982: A diagnosis of alpine lee cyclogenesis. *Mon. Wea. Rev.*, **110**, 1271–1287.
- MeteoSchweiz, 2006: Starkniederschlagsereignis August 2005. *Arbeitsberichte der Schweiz*, **211**, 63 pp.
- Mitzschke, H., 2013: Gewässerkundlicher Monatsbericht mit vorläufiger Auswertung des Hochwassers. Tech. rep., Sächsisches Landesamt für Umwelt, Landwirtschaft und Geologie. 69 pp.
- Mlawer, E., S. Taubmann, P. Brown, M. Iacono, and S. Clough, 1997: Radiative transfer for inhomogeneous atmosphere: RRTM, a validated correlated-k model for the long-wave. *J. Geophys. Res.*, **102**, 16 663–16 682.
- Mudelsee, M., M. Börngen, G. Tetzlaff, and U. Grünwald, 2004: Extreme floods in Central Europe over the past 500 years: Role of cyclone pathway Zugstrasse Vb. *Geophys. Res.*, **109**, D23 101, doi:10.1029/2004JD005034.
- Murray, R. and I. Simmonds, 1991: A numerical scheme for tracking cyclone centres from digital data, Part 1: Development and operation of the scheme. *Aust. Meteor. Mag.*, **39**, 155–166.
- Neu, U., et al., 2013: IMILAST: A community effort to intercompare extratropical cyclone detection and tracking algorithms. *Bull. Amer. Meteor. Soc.*, **94**, 529–547.
- Raible, C., 2007: On the relation between extremes of mid-latitude cyclones and the atmospheric circulation using ERA40. *Geophys. Res. Lett.*, **34**, L07 703.
- Raible, C., H. Saroni, B. Ziv, and M. Wild, 2010: Winter cyclonic activity over the Mediterranean Basin under future climate based on the ECHAM5 GCM. *Clim. Dyn.*, **35**, 473–488.

- Raible, C. C., P. M. Della-Marta, C. Schwierz, H. Wernli, and R. Blender, 2008: Northern hemisphere extratropical cyclones: A comparison of detection and tracking methods and different reanalyses. *Mon. Wea. Rev.*, **136**, 880–897.
- Simmons, A. J., K. Willet, P. Jones, P. Thorne, and D. Dee, 2010: Low-frequency variations on surface atmospheric humidity, temperature, and precipitation: Inferences from reanalyses and monthly gridded observational data sets. *Journ. of Geophys. Res.*, **115**, D01110.
- Simpson, J., 1983: Cumulus clouds: Interactions between laboratory experiments and observations as foundations for models. *Mesosc. Meteor.*, **114**, 399–412.
- Skamarock, W., et al., 2008: *A description of the advanced research WRF version 3*. Boulder, Colorado, USA, Nat. Cent. for Atmos. Res.
- Somot, S., F. Sevault, and M. Déqué, 2006: Transient climate change scenario simulation of the Mediterranean Sea for the twenty-first century using a high resolution ocean circulation model. *Clim. Dyn.*, **27**, 851–879.
- Tory, K. J., J. D. Kepert, J. A. Sippel, and C. M. Nguyen, 2011: On the use of potential vorticity tendency equations for diagnosing atmospheric dynamics in numerical models. *J. Atmos. Sci.*, **69**, 942–960.
- van Bebber, W. J., 1891: Die Zugstrassen der barometrischen Minima nach Bahnkarten der deutschen Seewarte fuer den Zeitraum von 1870-1890. *Meteor. Zeitschr.*, **8**, 361–366.
- Wang, W., et al., 2010: *ARW Version 3 modelling system user's guide*. Boulder, Colorado, USA, Nat. Cent. for Atmos. Res.
- Wernli, H. and M. Croci-Maspoli, 2013: Large-scale atmospheric dynamics. Tech. rep., ETH Zuerich, Institute for Atmospheric and Climate Science. 103 pp.
- Wernli, H. and H. C. Davies, 1997: A Lagrangian-based analysis of extratropical cyclones. I: The method and some applications. *Quart. J. Roy. Meteor. Soc.*, **123**, 467–489.
- Wernli, H. and C. Schwierz, 2006: Surface cyclones in the ERA-40 data set (1958–2001). Part 1: Novel identification method and global climatology. *J. Atmos. Sci.*, **63**, 2486–2507.
- Wiggert, V., 1969: Models of precipitating cumulus towers. *Mon. Wea. Rev.*, **97**, 471–489.

Acknowledgements

I would like to thank...

PD Dr. Christoph C. Raible for the possibility to write a thesis in his group and for the very valuable scientific support. Thank you! Furthermore, I'd like to thank Dr. Juan José Gómez-Navarro for all the explanations concerning regional modelling, and for the technical help. Thank you!

Cevahir Kılıç, Martina Messmer, and Dr. Stefan Muthers for their great technical support. Thank you guys!

My parents, who continuously supported me throughout my studies. Thank you very much!

All the people around me, who supportet me and gave me the neccesary strength to pull it through. In this regard, especially Nathalie and Elias are to mention. Thank you guys!

Last but not least, I'd like to thank the whole division of Climate and Environmental Physics, where I always found a good and supportive working atmosphere. Thanks!

Declaration

under Art. 28 Para. 2 RSL 05

Last, first name: Kumml, Claudio

Matriculation number: 08-117-327

Programme: Graduate school of climate sciences

Bachelor Master Dissertation

Thesis title: Sensitivity of precipitation to Mediterranean SSTs in the case of the Vb-type cyclone in August 2005 using the regional model WRF

Thesis supervisor: PD Dr. Christoph C. Raible

I hereby declare that this submission is my own work and that, to the best of my knowledge and belief, it contains no material previously published or written by another person, except where due acknowledgement has been made in the text. In accordance with academic rules and ethical conduct, I have fully cited and referenced all material and results that are not original to this work. I am well aware of the fact that, on the basis of Article 36 Paragraph 1 Letter o of the University Law of 5 September 1996, the Senate is entitled to deny the title awarded on the basis of this work if proven otherwise. I grant inspection of my thesis.

Place, date:

Signature: